Deriving Snow Accumulation Rates of Greenland and the Antarctic Ice Sheet from Microwave Remote Sensing Data

Stefanie Linow

AWI Alfred-Wegener-Institut
für Polar- und Meeresforschung
in der Helmholtz-Gemeinschaft

Universität Bremen

Universität Bremen 2011

Deriving Snow Accumulation Rates of Greenland and the Antarctic Ice Sheet from Microwave Remote Sensing Data

Vom Fachbereich für Physik und Elekrotechnik der
Universität Bremen

zur Erlangung des akademischen Grades eines
Doktor der Naturwissenschaften (Dr. rer. nat.)
genehmigte Dissertation

von

Stefanie Linow

1. Gutachter: Prof. Dr. Peter Lemke
2. Gutachter: Prof. Dr. Justus Notholt

Eingereicht am: 31. März 2011
Datum des Promotionskolloquiums: 16. September 2011

Erklärung

Hiermit versichere ich, dass ich

1. die Arbeit ohne unerlaubte fremde Hilfe angefertigt habe,
2. keine anderen als die von mir angegebenen Quellen und Hilfsmittel benutzt habe und
3. die den benutzten Werken wörtlich oder inhaltlich entnommenen Stellen als solche kenntlich gemacht habe.

Bremerhaven, den 31. März 2011

(Stefanie Linow)

Zusammenfassung

Um die Auswirkungen globaler Klimaveränderungen verstehen zu können, ist eine Beobachtung der Massenbilanz polarer Eisschilde erforderlich. Im Laufe der vergangenen Jahre wurden Methoden entwickelt, um die Genauigkeit der Massenbilanzabschätzung zu verbessern. Die Massenbilanz is die Summe aus Massenverlust und Massengewinn, und der Massenzutrag durch Schneeakkumulation ist noch immer unzureichend genau bekannt. Dies ist dadurch bedingt, dass die Polargebiete schwer zugänglich und daher in-situ-Daten rar und zudem ungleichmäßig verteilt sind. Aus diesem Grund ist es interessant, Fernerkundungsdaten zur Bestimmung von Schneeakkumulationsraten zu nutzen. Die Verfahren, die hierfür entwickelt wurden, sind jedoch noch immer relativ ungenau.

Im Rahmen dieser Arbeit wird analysiert, inwiefern man bereits vorhandene Verfahren zur Ableitung von Akkumulationsraten aus Mikrowellenfernerkundungsdaten verbessern kann. Zu diesem Zweck werden unterschiedliche Datentypen auf ihre Eignung für eine Akkumulationsratenbestimmung untersucht. Der hier gewählte Ansatz nutzt aus, dass Mikrowellen unter Trockenschneebedingungen mit den Schneeschichten wechselwirken und die Eigenschaften der Schneeschichten (wie Korngröße und Dichte) durch die Akkumulationsrate beeinflußt sind. Gegenüber diesen Änderungen in der Schneeschicht sind Mikrowellen sensitiv. Aus diesem Grund wird in der vorliegenden Arbeit die Schneemikrostruktur detaillierter betrachtet. Basierend auf dieser Untersuchung ergibt sich die Entwicklung einer verbesserten Parametrisierung der Schneemikrostruktureigenschaften Dichte und Korngröße als Funktion der Tiefe, und abhängig von den Temperaturbedingungen. Ergebnisse der Mikrostrukturmodellierung werden nun genutzt, um mit Hilfe eines einfachen Strahlungstransfermodells die Wechselwirkung zwischen Mikrowellen und Schneevolumen zu beschreiben. Das hierbei simulierte Signal wird dann mit Satellitendaten abgeglichen, um Akkumulationsraten ableiten zu können. Da sich einige Vereinfachungen im Strahlungstransfermodell als ungültig erwiesen haben, werden diese durch geeignetere Annahmen ersetzt, z.B. durch Nutzung der Theorie zur Mie-Streuung.

Die Ergebnisse des hier entwickelten Algorithmus zur Ableitung von Akkumulationsraten werden mittels in-situ-Daten validiert, und sein Gültigkeitsbereich kann ebenfalls festgestellt werden. Die mit dem vorgestellten Verfahren abgeschätzten Akkumulationsraten stimmen im Gültigkeitsbereich dieser Methode sowohl mit den in-situ-Daten, als auch mit Akkumulationskarten aus externen Quellen, gut überein.

Summary

In order to estimate the impact of climate change it is necessary to monitor the surface mass balance of the ice sheets. Much effort has gone into developing accurate methods for surface mass balance estimation over the past years. Mass balance is defined as the sum of mass gain and mass loss. Still, it remains difficult to quantify surface accumulation, which is the net gain term of the balance equation. This is due to the fact that the polar ice sheets are difficult to access, so in-situ measurements are sparse. Therefore, it is important to employ remote sensing techniques to obtain accumulation data with a better spatial and temporal resolution. However, the resulting datasets still exhibit large amounts of uncertainty.

This thesis seeks to improve the currently available methods to derive snow accumulation rates from microwave remote sensing data. For this purpose, different types of microwave data are systematically evaluated with respect to their suitability for accumulation rate retrieval. The approach taken here makes use of the fact that microwaves interact with a volume of dry polar firn and are sensitive to accumulation rate-dependent firn characteristics. For this reason, firn microstructure is examined in more detail. On the basis of this analysis, an improved parameterization of firn properties (grain size and density) is developed, which is valid for the layers of the firn column that interact with the microwave radiation. The improved microstructure model is used in conjunction with a simple radiative transfer model to simulate firn-microwave interaction, resulting in a synthetic microwave signal. Accumulation rates can subsequently be inverted by matching the signal from the model to microwave data measured by satellite sensors. A number of assumptions made in the radiative transfer model have proven to be invalid. In this work, the radiative transfer model is improved by including Mie scattering instead of the widely-used Rayleigh approximation for the combination of scatterer sizes and microwave frequencies investigated.

The results from the accumulation retrieval algorithm developed in this work are validated with in-situ data, and limits in its applicability are evaluated. Accumulation rates inverted from the method introduced in this work are found to agree with field data as well as with accumulation maps from external sources within the range of the model's validity.

Contents

List of Figures

List of Tables

Hic sunt dracones
(the Lenox Globe, ca. 1510)

1

Introduction

In a changing climate, the polar ice sheets play an important role. The Antarctic ice sheet alone stores approximately 70% of the world's freshwater resources. Meltwater from the polar ice sheets influences the thermohaline circulation in the oceans as well as the global water cycle. Mass loss of the ice sheets caused by melt or glacier calving events also contributes to sea level rise. A change in the extent of ice sheets and mountain glaciers also directly impacts the global radiation budget due to albedo changes. For those reasons it is important to assess the current state and the changes of the polar ice sheets, as they are key factors to evaluate the implications of climate change.

1.1 Ice sheet mass balance

To assess the impact of a changing climate on extent, thickness and dynamics of the polar ice sheets, it is necessary to quantify their mass variations on both spatial and temporal scales. This can be done by looking at the total mass balance of an ice sheet, which can be expressed as the sum of accumulation (mass gain) and ablation (mass loss). The term "accumulation" denotes the net mass gain on a glacier or an ice sheet. It includes precipitation, but snow redistribution by wind drift also has to be considered. Ablation is defined as the net mass loss. It can be caused by a combination of very different factors, such as wind redistribution of snow, calving of icebergs, surface runoff, evaporation and the basal melting of ice shelves. Both terms are defined in units of water equivalent height per unit area, per time interval (usually a year). The boundary between accumulation and ablation areas is called equilibrium line, its location varies according to the seasonal cycle and due to changing climate conditions. The main environmental processes influencing the ice sheet's mass balance are sketched in Figure 1.1.

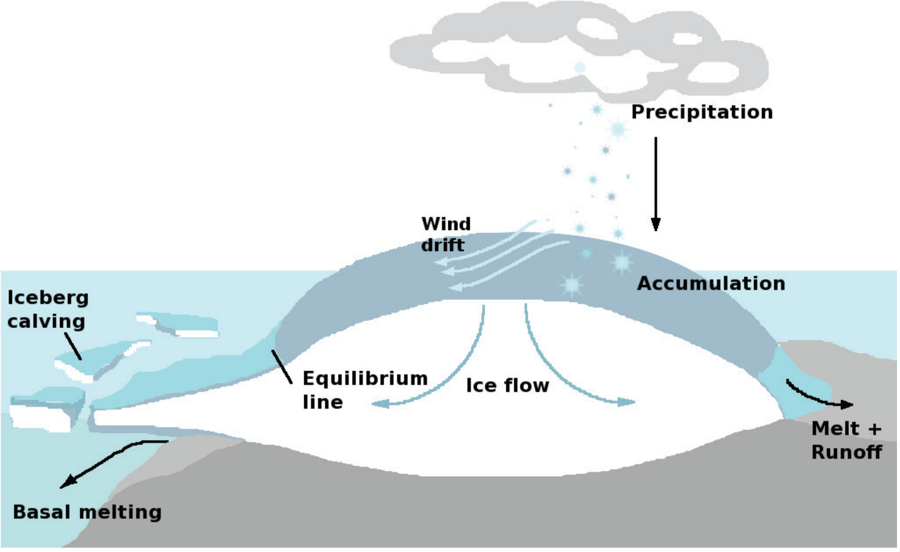

Figure 1.1: *Surface mass balance of polar ice sheets*

Different methods have been developed to measure the total mass balance or its components. By analysing firn core and snow pit records, accumulation rates can be determined from the layering of the firn*. Inclusions of dust, volcanic ash and a number of other chemical tracers can be used to date the layers (Bales et al., 2001a; Oerter et al., 1999, 2000). From stake measurements, mass loss in the ablation zone as well as mass gain can be quantified (Schlosser et al., 2002).

Another approach for mass balance determination is the hydrological method of calculating the mass gain and loss from data for precipitation, evaporation and surface run-off (Schlosser et al., 2008). This includes using climate models (Dethloff et al., 2002; Genthon et al., 2009). Many methods have been developed to determine the ice sheet mass balance from remote sensing data. It is, for instance, possible to detect the equilibrium line in satellite images or to map surface melt (Abdalati and Steffen, 1997; Liu et al., 2006). While this method allows no direct quantitative statement about mass change, it is very useful to map long-term spatial trends in the mass balance development (Abdalati and Steffen, 2001).

A different approach to quantify mass change is to map surface elevation changes by spaceborne (Lacroix et al., 2008) and airborne altimetry (Helm

---

*The term "firn" denotes snow on an ice sheet that has survived at least one summer season without melting or being transformed into glacier ice. In the regions of polar ice sheets not affected by melt, a clear distinction between snow and firn is not possible, hence the two terms will be used interchangeably.

et al., 2007). Direct mass changes were derived from satellite gravimetry missions (Sasgen et al., 2007; Velicogna, 2009; Chen et al., 2009). Different methods of mass balance determination were combined to improve the accuracy of the results, but the uncertainty associated with the balance terms is still large (Vaughan et al., 1999; Shepherd and Wingham, 2007; Rignot et al., 2008b,a). Table 1.1 illustrates this with a compilation of net accumulation rates determined using different methods.

Table 1.1: *Snow accumulation on the Antarctic ice sheet (grounded ice)*

Source	Method	Accumulation [Gt/a]
Vaughan et al. (1999)	interpolated field data	2288
Giovinetto and Zwally (2000)	interpolated field data	2326
Huybrechts et al. (2000)	interpolated field data	2344
Rignot et al. (2008a)	climate model	2055
Arthern et al. (2006)	passive microwave, field data	1730
Monaghan et al. (2006)	climate model	1475–2331

The purpose of this thesis is to look at the gain term of the mass balance equation and improve the accuracy of snow accumulation estimates.

1.2 Measuring snow accumulation

There are many different approaches to measure accumulation. A very extensive description of different techniques used to measure snow accumulation in the field is given by Eisen et al. (2008). For a variety of methods used to determine accumulation, Figures 1.2 and 1.3 show the resolution capabilities on a spatial and temporal scale: data from microwave remote sensing can cover large areas at a comparably high spatial and temporal resolution. Hence it has the potential to improve the knowledge about snow accumulation variations, especially in areas that are otherwise difficult to access.

A number of accumulation datasets were derived from spatially interpolated field measurements. One of the first spatially interpolated accumulation maps of Greenland was compiled by Ohmura and Reeh (1991). Due to the inhomogeneous distribution of sampling points and the different methods of data acquisition, great care has to be taken in handling of statistical properties of the interpolated datasets. An error estimate for accumulation mapping from interpolated field data on the Greenland ice sheet is given, for example, by Cogley (2004).

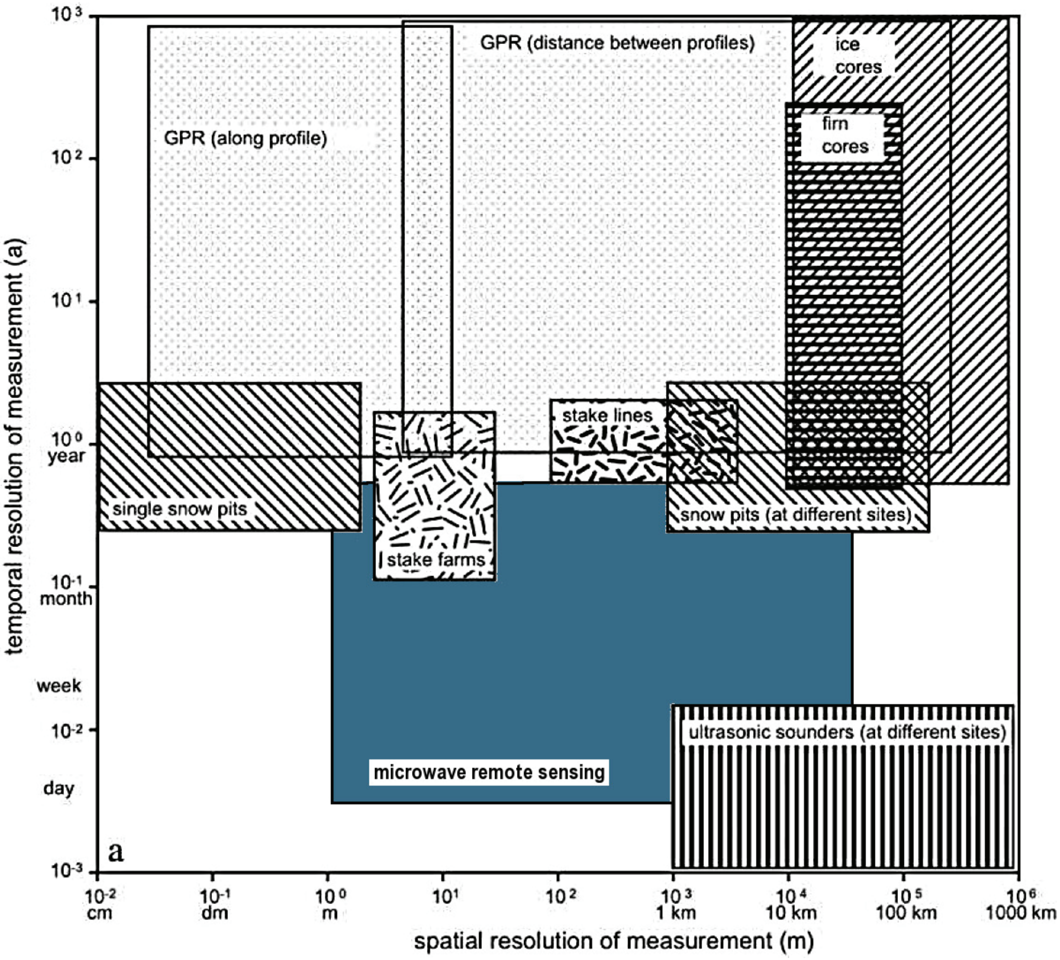

Figure 1.2: *Spatial resolution of different methods of accumulation measurement. Image from Eisen et al. (2008) (modified by including microwave remote sensing)*

Magand et al. (2007) interpolated field measurements of accumulation to obtain a “quality-controlled” dataset for the 90° - 180° E sector of Antarctica, focusing on the heterogenity of the different methods used to aquire field data and their respective levels of uncertainty. Rotschky (2007) used spatially interpolated field data to compile an accumulation dataset for Dronning Maud Land, considering the spatial autocorrelation and statistical properties of the point measurements. Arthern et al. (2006) combined passive microwave data with field measurements using a universal kriging approach to map accumulation rates for Antarctica, and Bindschadler et al. (2005) used passive microwave data at 85.5 GHz to map snowfall events, and derive accumulation rates based on IceSat altimetry at three sites in Antarctica.

Various approaches exist to directly infer accumulation rates from microwave remote sensing data, without considering prior information from ground truth. Bingham and Drinkwater (2000) examined the seasonal and interannual signa-

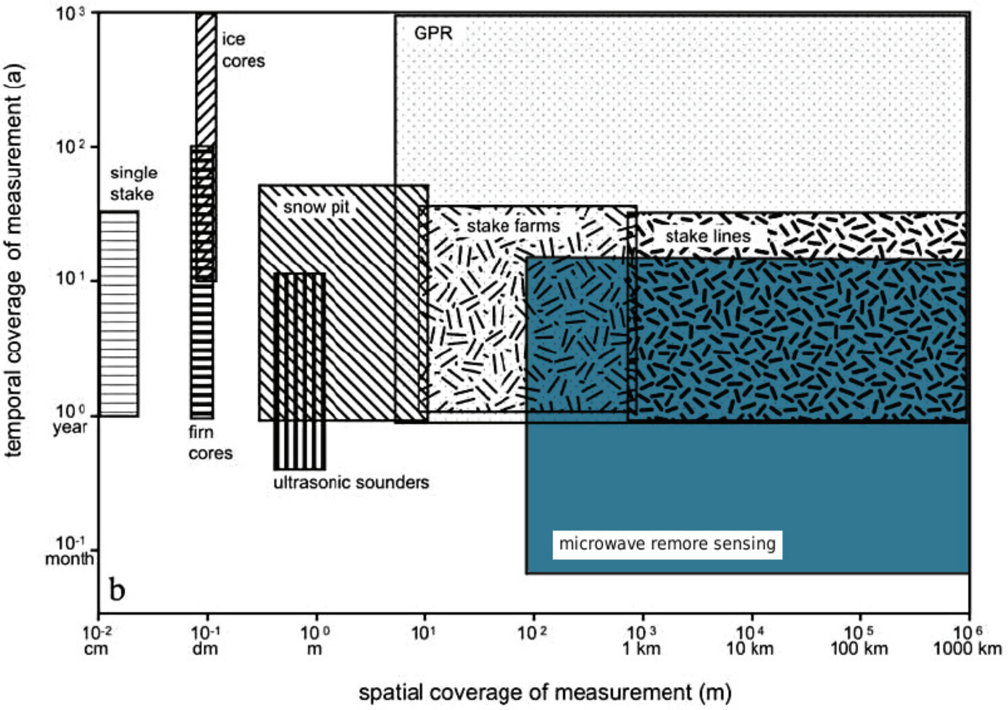

Figure 1.3: *Spatial coverage of different methods of accumulation measurement. Image from Eisen et al. (2008) (modified by including microwave remote sensing)*

ture of time series of passive microwave data from several regions in Antarctica and linked changes in brightness temperature to changes in the firn structure. They observed that changes in grain size due to metamorphism processes in the firn column influence brightness temperatures, and deduced that there is a link between accumulation rate and brightness temperature.

Munk et al. (2003) modeled firn microwave interaction to infer accumulation rates from the C-band radar mosaic of the dry snow zone† of Greenland, and Flach et al. (2005) employed a coupled firn layer/radiative transfer model to simulate time series of brightness temperatures and microwave backscatter properties depending on a set of snowpack parameters, and found large deviations between model results and absolute values of satellite data on the Greenland ice sheet.

1.3 Evaluation of remote sensing applications for snow accumulation retrieval

Forster et al. (1999) used shallow firn core data and accumulation rates mea-

---

† A region of a glacier or an ice sheet that never experiences melt.

sured at transects at the Greenland Summit region in a combination with the ERS-1 SAR backscatter mosaic to enhance the spatial resolution of an accumulation map interpolated from field data. Automatic weather station (AWS) snow heights for Greenland were compared to QuikSCAT data by Nghiem et al. (2005) to improve snow accumulation estimates for the Greenland ice sheet.

The spatially interpolated accumulation map of Greenland by Ohmura and Reeh (1991) was combined with SSM/I data (Pack and Jensen, 2001). Drinkwater et al. (2001) used scatterometer data to infer accumulation rates and validated results with ice core records from Greenland. The C-band ERS-1 SAR mosaic and a set of accumulation point measurements for Greenland were used by Munk et al. (2003) to map accumulation. Flach et al. (2005) used passive and active microwave time series, and compared results with spatially interpolated accumulation records (Bales et al., 2001b). An approach to snow accumulation quantification using SAR interferometry and the spatially interpolated Ohmura/Reeh accumulation map was taken by Oveisgharan and Zebker (2007). Passive microwave-derived accumulation rates were compared with 14 shallow ice cores from ITASE and GPR profiles in Antarctica by König et al. (2007).

Microwave interaction with a polar snow volume is a complex process, with many parameters influencing the signal. The structure of polar firn is determined by local climate conditions, such as temperature, wind and accumulation rate. Retrieving accumulation rates from microwave data without using an external set of field data for calibration is only possible in an indirect approach that considers firn-microwave interaction. The accuracy of the model result always depends on the accuracy of the firn column representation and the model of firn-microwave interaction. Previous approaches used to invert accumulation rates relied on empirically determined correction factors to compensate for insufficiencies in both the microstructure representation and the model of firn-microwave interaction.

This work aims to improve existing approaches to accumulation rate retrieval and to develop a method that is independent of external field data. It is structured in the following way:

Chapter 2 introduces the datasets needed to invert accumulation rates — passive and active microwave images and some supplementary information which is needed for preprocessing. Ground truth is required to validate the accumulation retrieval results, and temperatures are needed as they are a variable parameter in the inversion. For this reason, great care has been taken to validate the temperatures and account for possible sources of error. Radar data need additional preprocessing steps to account for some specific image properties. Hence, routines for incidence angle correction and normalization were implemented to complement the standard radiometric calibration. The comparison of different datasets, e.g. temperatures, elevations and microwave data, required the development of some basic geocoding and geolocation tools, which were also necessary for the comparison of satellite and field data in Chapter 6.

Chapter 3 examines the medium. Polar firn has a complex microstructure, and therefore great care was taken in evaluating the microstructure models used in existing snow accumulation retrieval approaches. This process eventually led to the development of a new firn microstructure parameterization which is better suited to describe the upper meters of the firn column interacting with microwave radiation.

The theoretical background of firn-microwave interaction is briefly introduced in Chapter 4, and different approaches to describe this process in a physical model are discussed.

Chapter 5 describes the model of firn-microwave interaction implemented within the context of this thesis. It discusses the problems that arise as a consequence of simplifications in the model, specifically due to the Rayleigh approximation used to describe extinction properties of the medium. It is noted at this point that Mie scattering needs to be considered here, which is then implemented in the radiative transfer model used in this work.

In Chapter 6, the accumulation rate inversion algorithm is introduced, and the model results are validated using ground truth. Since it proves difficult to reconstruct absolute values of the microwave signal due to limitations in the radiative transfer model, the amplitudes of the seasonal signals are examined with respect to their suitability for accumulation rate retrieval. It is shown that, while the amplitudes are better suited to invert accumulation rates, there are limitations to the validity of this approach dependent on sensor frequency, polarization and magnitude of accumulation rate. From the model validation, suitable ranges of input parameters are found. Resulting accumulation maps generated from the retrieval algorithm are validated using ground truth as well as supplementary accumulation maps from different external sources. It is concluded that, by improving the firn microstructure model and considering Mie scattering in the radiative transfer model, it is possible to map accumulation rates up to 0.2 m w.e./a from microwave remote sensing data without an external calibration of the results using field data or empirically derived bias correction terms.

Chapter 7 finally summarizes the results of this work, and shows its limitations as well as perspectives for further improvements of accumulation retrieval methods.

2

Data

This work combines a number of different datasets for determining snow accumulation on the polar ice sheets. Data from various active and passive spaceborne microwave sensors, operating at different wavelengths and spatial resolutions, serve as basic input for the snow accumulation retrieval algorithm. The latter requires some supplementary datasets.

Digital elevation models are needed for SAR data processing and are used as a proxy for estimating air temperature distribution over the Greenland ice sheet in initial versions of the retrieval algorithm. Air temperatures over the ice sheets have a great influence on densification and grain growth processes in the underlying snow layers, and for this reason temperature datasets from various sources were included in this work.

Data from field measurements of snow accumulation in Greenland and Dronning Maud Land (Antarctica) are used for calibration and validation of the retrieval results, and measurements of snow microstructure permit the improvement of the snow pack model introduced in section 3.2.

This chapter gives an overview of the different types of data used here, their main characteristics, and a basic description of processing steps required for further application.

2.1 Ground Truth

The following section introduces the sets of field data: accumulation rates, firn density profiles and grain size measurements.

2.1.1 Accumulation

Snow accumulation datasets for Antarctica are available for Dronning Maud Land (DML), compiled from 136 snow pit or firn core datasets by Rotschky et al. (2006). An additional set of stake measurements from the Kottas Traverse, comprising more than 900 single points of measurements, was also used (Figure 2.1b) (Rotschky et al., 2007). A more detailed description of the data can be found in the publications referenced above. Figure 2.1 shows where the points of measurements are located and the amount of accumulation measured.

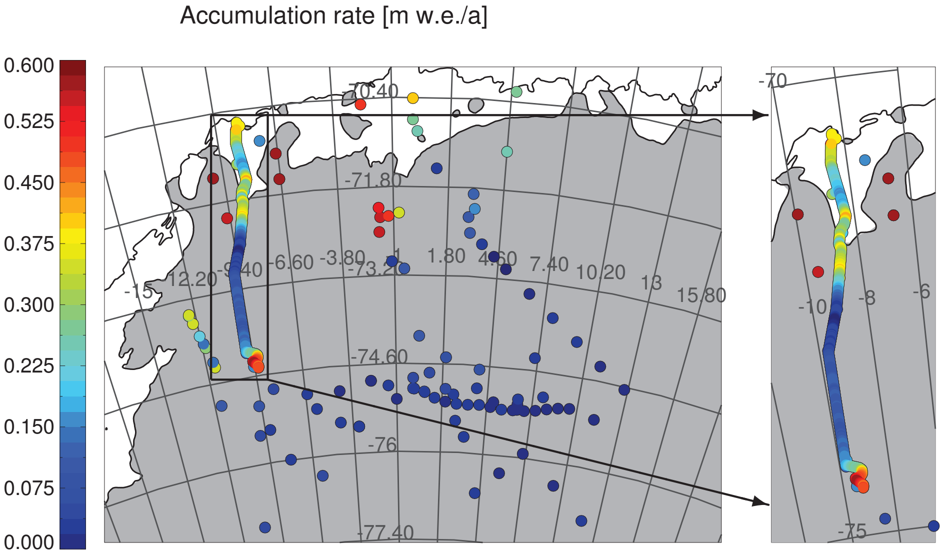

(a) *Overview* (b) *Traverse*

Figure 2.1: *Accumulation measurements*

2.1.2 Density

Firn density records are needed to validate the snow pack model. Density data from 19 firn cores measured during the “European Programme for Ice Coring in Antarctica” pre-site survey on the inland ice plateau of Dronning Maud Land (Oerter et al., 2000) were used in this work. Additionally, density records for 5 firn cores from the 1996/97 field season (Oerter et al., 1999), one firn core from Wilhelms (2000) and 16 density records from shallow firn cores (Oerter et al., 2008) were available from Dronning Maud Land. For the Greenland ice sheet, density records of six ice cores from the North Greenland Traverse (Wilhelms, 2000; Schwager, 2000) are available.

Firn densities were obtained from core samples by weight and volume measurements or by gamma-density measurements (Wilhelms, 2000). The locations of the density records used to derive the densification model in Section 3.2.1 is shown in Figure 2.2. A complete list of all density records used here can be found in Appendix 7.

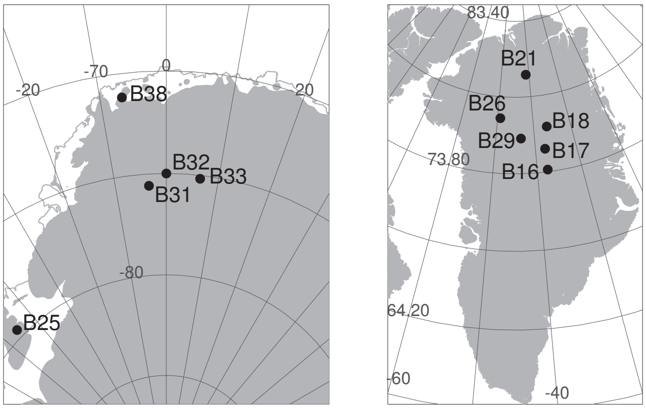

Figure 2.2: *Locations of the density profiles*

2.1.3 Grain Size

To examine firn microstructure characteristics, five firn cores from different sites in Antarctica and one firn core from the dry snow zone of Greenland (Figure 2.3) were analyzed at AWI using X-ray micro-computer tomography (CT) by Hörhold (2010).

The firn core locations represent a wide range of polar climate conditions, ranging from the relatively warm, high-accumulation environment of the B38 core location to the very cold, low-accumulation Dome C site (Table 2.1).

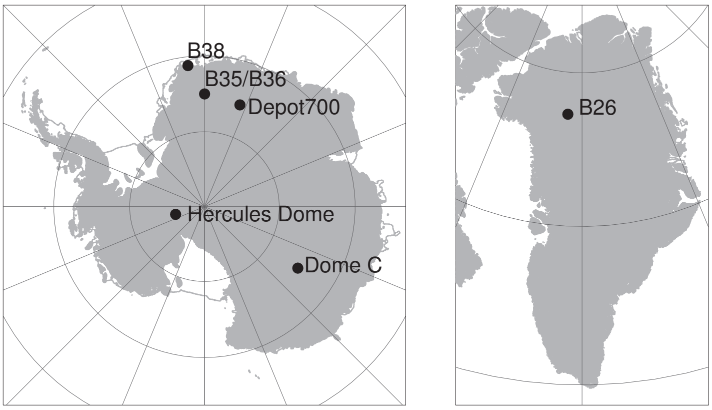

Figure 2.3: *Locations of the grain size profiles*

Table 2.1: *Firn core locations and environmental conditions*

Name	Lat. [°]	Lon. [°]	Mean temp. [°C]	Accumulation [m w.e. · a^{-1}]	Elevation [m a.s.l.]
B26	77.25	-49.22	-31.6	0.180	2598
B35/B36	-75.00	0.07	-44.6	0.067	2415
B38	-71.16	-6.70	-18.1	1.250	690
Depot700	-75.65	19.24	-51.0	0.045	3530
Dome C	-75.10	123.35	-53.0	0.025	3233
Hercules Dome	-86.00	-105.00	-37.0	0.180	2610

To capture grain size variability, the B36, B38 and DP7 cores were sampled continuously at the uppermost 1–2 m. Below that, samples of 40 cm length with 16–20 measurements were taken at each following meter of the core, as indicated in Figure 2.4. The B26 core is sampled each meter from the surface using the 40 cm interval size, and the record from Hercules Dome contains discontinuous samples at irregular steps throughout the entire core. The lowermost 1-meter intervals of B38 and B26 were sampled continuously again. Firn microstructure images are constructed by backprojection of a series of X-ray shadow images of a firn core rotated in 0.9 ° steps. The resulting image stack is reconstructed into a 3-D image. After filtering, segmentation and threshold determination, the 3-D image is binarized to discern pore space and ice phase. From the datasets, porosity (pore fraction) and density (ice fraction × density of pure ice) are calculated. The longest extent of a grain in one or more arbitrarily defined directions is called chord length, it is determined from the sample together with the total surface and the total volume of the ice phase. From those quantities the specific surface area (SSA) is calculated, and this value is used to derive the effective grain size r_{eff} as a measure of particle size in the firn sample. A more extensive discussion of grain size parametrization can be found in section 3.1.3.

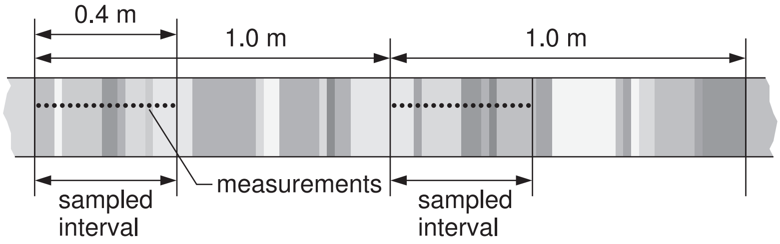

Figure 2.4: *Grain size sampling*

2.2 Digital Elevation Models

Elevation models are required for determining the local incidence angle during radiometric calibration of high-resolution SAR images. They can also be used for estimating the mean annual surface temperature, which is one of the input parameters for the snow microstructure model.

2.2.1 Greenland

For the Greenland ice sheet, the digital elevation model, published by Bamber et al. (2001a), was used (Figure 2.5). This dataset was generated from a combination of different sources: radar altimetry from ERS-1 and Geosat, Airborne Topographic Mapper (ATM) data, height data from photogrammetric analysis of aerial photos and DEMs provided by the U.S. National Imaging and Mapping Agency (NIMA) (Bamber et al., 2001b). The dataset has a horizontal resolution of 5 km and is mapped to a polar stereographic projection with reference to the WGS84 ellipsoid. The standard deviation of elevations for the entire ice sheet is given by the autors to be ± 6.97 m. This elevation model can be obtained via the NSIDC website.

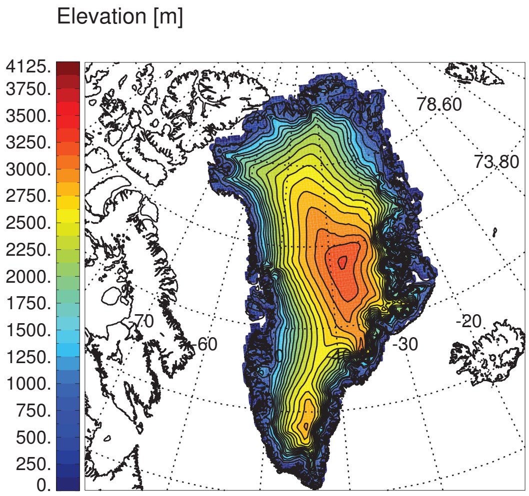

Figure 2.5: *Digital Elevation Model of Greenland*

2.2.2 Antarctica

The RAMP DEM, version 2, is also provided by the NSIDC (Liu et al., 2001). It was compiled from various sources, among them radar altimeter data, GPS surveys, and large-scale topographic maps from the U.S. Geological Survey

(USGS) and the Australian Antarctic Division. Vertical accuracy of the DEM varies considerably, ranging from ± 1 m on the ice shelves, ± 7.5 m for the relatively flat interior of the ice sheet, ± 15 m for steeply sloped coastal regions, and up to ± 100 m over rugged mountainous areas. The elevation model (Figure 2.6a) is available at grid sizes of 1 km, 400 m, and 200 m. For combination with QuikSCAT and SSM/I data (with pixel sizes on the order of 20 km) which require continent-wide coverage, a spatial resolution of 1 km is sufficient.

For incidence angle correction of SAR data, a more accurate elevation model than RAMP is required. Ground-based kinematic GPS, airborne and satellite altimetry data were combined into an elevation model of central Dronning Maud Land by Wesche (2009) (Figure 2.6b). This DEM covers a spatial extent from 20°W to 20°E and from 69°S to 86°S. It has a spatial resolution of 2.5 km, and elevation errors range from ± 4.45 m in the coastal regions to ± 0.26 m on the plateau. Elevation values of both datasets are with reference to the WGS84 ellipsoid. As mentioned before, the elevation models are needed for local incidence angle correction in the SAR images, so it is interesting to look at the influence of the DEM's accuracy on the local slope correction. In order to illustrate the problem, it is reduced to a 1-D case without loss of generality. If p is the DEM's pixel size, and Δh the elevation difference between two adjacent pixels, the local incidence angle deviation $\Delta\theta$ from the ellipsoid normal due to the local slope is

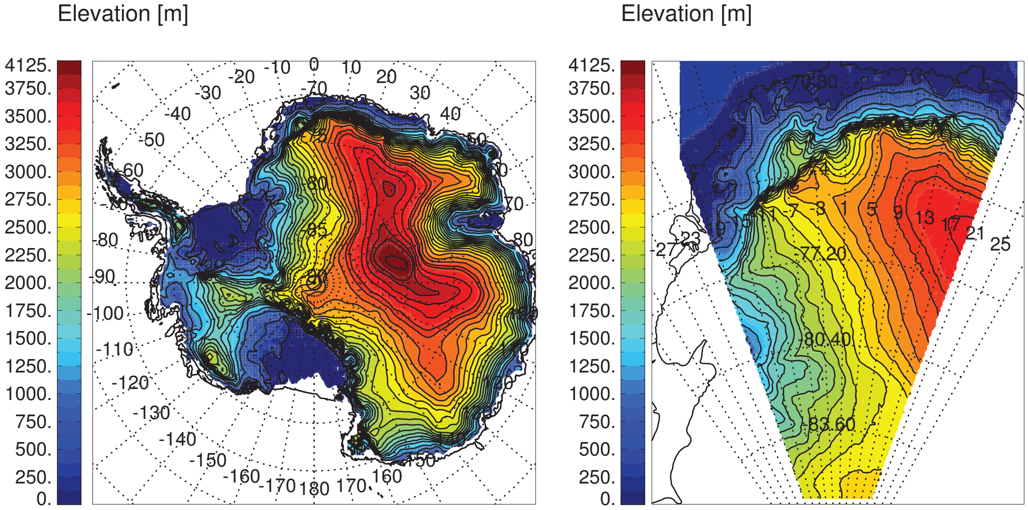

(a) *Antarctica* **(b)** *DML region, (Wesche, 2009)*

Figure 2.6: *Digital Elevation Models — Antarctica*

$$\Delta\theta = \arctan\frac{\Delta h}{p} \tag{2.1}$$

A simple error propagation for an elevation standard deviation σ_h gives an error estimate $\sigma_{\Delta\theta}$ for the local incidence angle deviation:

$$\sigma_{\Delta\theta} = \pm \frac{\sigma_h}{p + \Delta h^2/p} \tag{2.2}$$

Results from the error estimate in Figure 2.7 show that the local DML elevation model yields more accurate results for the local incidence angle correction needed for SAR image calibration. The standard deviation σ_h is the elevation uncertainty of a single measurement: the error of an elevation value averaged over the DEM's pixel size. In the case of high-resolution microwave data recorded over very rugged terrain, the deviation of the surface elevation at the position of a microwave pixel from the according DEM value can significantly exceed σ_h. This increases the error of the local incidence angle $\sigma_{\Delta\theta}$, and the effect becomes more pronounced with larger differences between the spatial resolutions of the two types of data. Still, for the relatively flat terrain found on the Antarctic plateau the error estimate from Equation 2.2 remains valid, and the DML DEM seems to be the most appropriate choice for SAR image calibration despite its low spatial resolution.

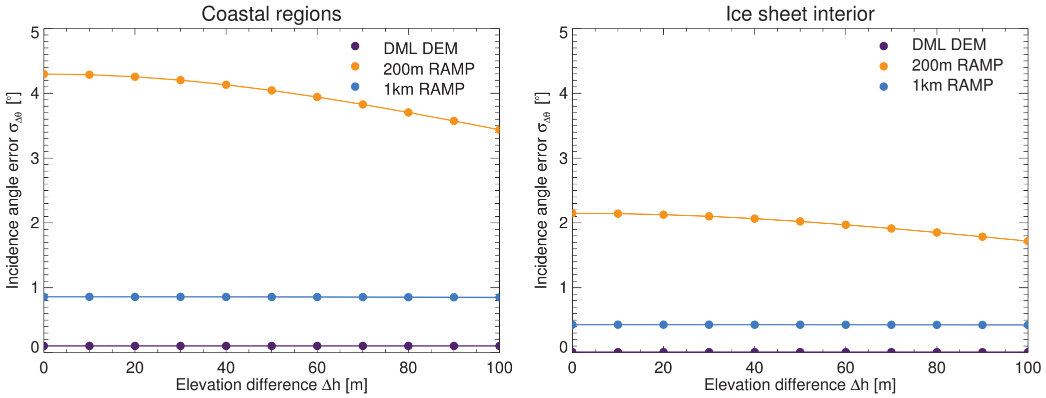

(a) *Incidence angle error in coastal regions* **(b)** *Incidence angle error at ice sheet interior*

Figure 2.7: *Error estimate for local slope correction*

2.3 Temperature

It is important to consider temperatures at the surface of the ice sheets, since there is a strong influence of temperature on the evolution of firn profile properties, such as density and grain size (Colbeck, 1983). There are different types of temperature measurements available for polar regions.

For example, firn core temperatures measured at 10 m depth can be used to estimate mean annual temperatures, because the seasonal temperature signal is no longer present at this depth (Paterson, 1999). There are a number of weather stations located on the polar ice sheets, but temperatures are recorded not directly at the surface of the ice, but at some height above ground, which can lead to a temperature bias (Takahashi et al., 1998). Also, the inhomogeneous spatial distribution of point measurements can lead to large uncertainties in the data, and this has to be taken into consideration when working with this type of data.

Surface temperatures can also be measured by satellite sensors working in the infrared part of the electromagnetic spectrum. Those measurements are sensitive to cloud cover (Comiso, 2000), and algorithms for cloud detection and filtering have been developed to address this problem. The following sections describe the different approaches used in this work to estimate the surface temperature of polar ice sheets.

2.3.1 Field data-derived temperatures

Local-scale temperature datasets that were compiled from field data exist for Greenland and Antarctica. Temperatures are either directly available or given in the form of empirical equations linking geographical latitude and elevation to temperature.

Greenland

Different empirical models exist to estimate mean annual surface temperatures $\bar{T}$ in the dry snow zone of Greenland. These equations describe the temperature as a function of elevation h and geographic latitude Φ. One relation was derived by a linear regression from a temperature map of Greenland by Ohmura (1987):

$$\bar{T} = 48.38 - 0.007924\ h - 0.7512\ \Phi. \tag{2.3}$$

The dataset on which equation 2.3 is based, comprises 48 stations. Of those, 26 were located in ice-free areas along the coast and were not used in the regression. This leaves 22 stations of which only 5 recorded air temperatures throughout the entire year (Reeh, 1989). In another approach, Greenland GC-Net Automatic Weather Station (AWS) data (Steffen et al., 1996) were used to describe mean annual temperature $\bar{T}$ and temperature amplitude ΔT as a function of elevation and geographic latitude (Flach et al., 2005).

$$\bar{T} = 49.4198 - 0.00602023\ h - 0.809669\ \Phi \tag{2.4}$$

$$\Delta T = -5.31628 - 0.00024020\ h + 0.270005\ \Phi \tag{2.5}$$

From a comparison of equations 2.3 and 2.4, differences of more than 3 °C can be recognized. A temperature change of 3 °C is roughly equivalent to a difference in grain radius of 0.3 mm at a profile depth of 25 m[*]. The sensitivity of the microwave signature to grain size and its implications for accumulation retrieval are addressed in more detail in Section 6.2.

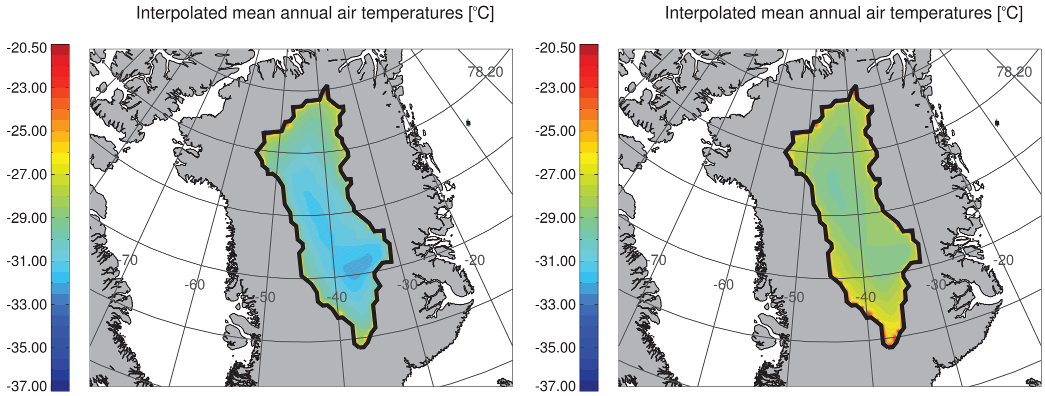

(a) *Ohmura/Reeh* **(b)** *GC-Net AWS data*

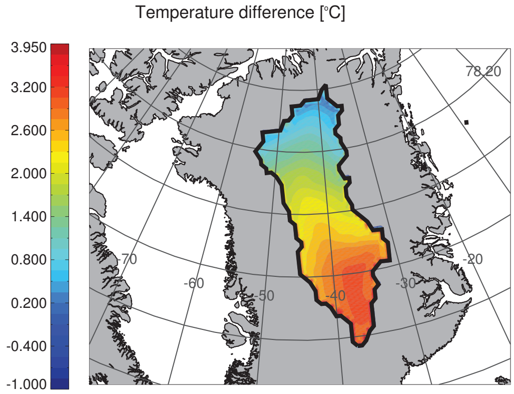

(c) *Difference between (a) and (b)*

Figure 2.8: *Interpolated mean annual temperatures [°C] in the Greenland dry snow zone from two different empirical relations, comparison between the empirically derived values and temperatures from MODIS data. The dry snow zone is marked by a thick black line*

Considering the large differences between the temperature maps of the Greenland dry snow zone, it seems to be reasonable to use actual high-resolution MODIS measurements to estimate surface temperature instead of relying on

---

[*] The value is calculated from the microstructure model introduced in Section 3.2

empirical relationships derived from relatively few points of data. A discussion of MODIS data accuracy will follow in Section 2.3.2.

Antarctica

The THERMAP data set (Bohlander and Scambos, 2001) consists of more than 800 shallow firn core temperature (10-meter temperature) and deeper ice core temperature (drill hole temperature) measurements. It covers the entire continental ice sheet and several ice shelves. The position of the measurements is given in polar stereographic projection. This dataset was used as a proxy for mean annual air temperatures in Antarctica. The dataset is spatially very inhomogeneous, with many measurements on the large ice shelves and the peninsula and almost no data in the central Antarctic, causing large interpolation errors in the ice sheet's interior when the data is interpolated over the entire continent.

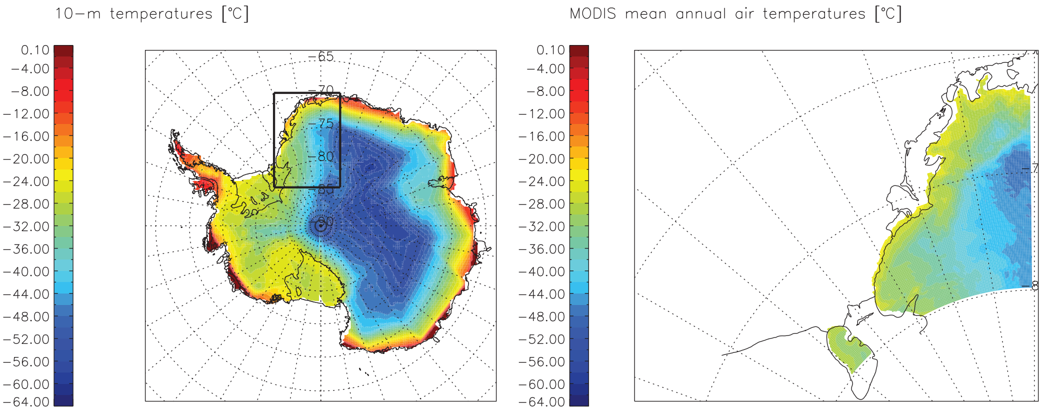

(a) *Interpolated THERMAP data* **(b)** *Annual average of MODIS data set for DML*

Figure 2.9: *Interpolated mean annual temperatures (Antarctica)*

2.3.2 Satellite-based temperature measurements

Land surface temperatures at a high spatial and temporal resolution are recorded by the MODIS (Moderate-resolution Imaging Spectroradiometer) instrument aboard the Terra and Aqua satellites. Both instruments combined image the entire Earth every 1 to 2 days (LPDAAC, 2009a). MODIS measures radiation in 36 spectral bands, at different resolutions ranging from 250 m (bands 1 and 2) to 500 m (bands 3 to 7) and 1000 m for the remaining bands. Land surface temperatures (LST) are recorded in the spectral

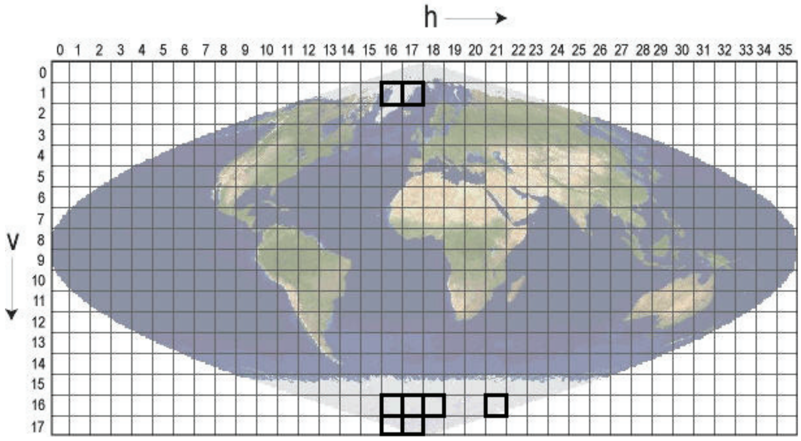

Figure 2.10: *MODIS sinusoidal grid and derived tile names. Image from (LP-DAAC, 2009a). Tiles used in this work are marked by a black frame*

bands 31 (10.780 µm – 11.280 µm wavelength) and 32 (11.770 µm – 12.270 µm wavelength). Sensors working at those wavelengths are sensitive to cloud cover. The data product used here are level-3 MODIS global Land Surface Temperature and Emissivity data (version 5). Average values of clear-sky land surface temperatures during an 8-day period are stored on a 1-km Sinusoidal grid.

One MODIS file contains 12 data layers, e.g. daytime LST, nighttime LST, cloud cover, emissivities, quality control records. Only the daytime LST layers were extracted from the datasets, and they were reprojected to geographic latitude and longitude. For layer extraction and reprojection, the MODIS Reprojection Tool (LPDAAC, 2009b) was used. In this work, the following MODIS tiles were processed: h16v01, h17v01, (Greenland), h16v16, h16v17, h17v16h, h17v17, h18v16 and h21v16 (Antarctica). Their location is shown in Figure 2.10. For each tile, 8-day averaged MODIS daytime land surface temperature datasets covering the entire year 2008 were used, resulting in up to 47 data points per pixel per year. The MODIS instrument is sensitive to atmospheric water vapor, and measurements influenced by cloud cover are removed from the data product during preprocessing. This has two implications. First, only in-situ temperature measurements under clear-sky conditions can be used for an accuracy assessment of the MODIS data.

MODIS land surface temperatures were validated by Wan (2008) with in-situ temperature measurements under clear-sky conditions and a temperature range between -10 °C and +58 °C. The accuracy of MODIS measurements was found to be better than 0.7 K, and better than 0.5 K for cases with low atmospheric aerosol levels. A comparison between MODIS LST and in-situ temperatures from the Greenland AWS network was carried out by Hall et al.

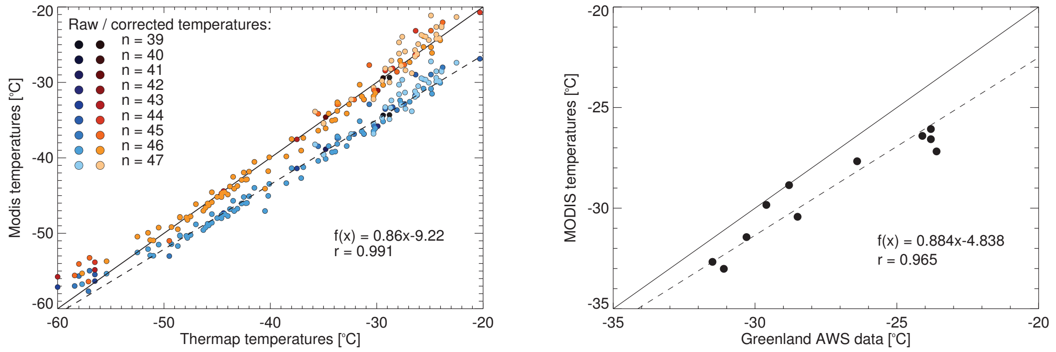

(a) *MODIS/THERMAP correlation for Antarctica. The number of datasets used to calculate the annual average, n, is color-coded for quality control. Image pixels with n< 39 were not considered for averaging.*

(b) *MODIS/AWS correlation for Greenland. Please note that the axis scaling is different from Figure 2.11*

Figure 2.11: *MODIS/field data correlation*

(2008), who reported a standard deviation of 2.1 °C.

The second implication of the instruments' sensitivity to atmospheric water vapor is that atmospheric insulation effects caused by cloud cover cannot be represented in the MODIS data. This means that the LST are biased towards lower values. This effect can be confirmed by comparison with the THERMAP datset. In order to quantify the temperature bias, MODIS pixel values at the positions of the THERMAP firn/ice cores were retrieved from the datasets. From Figure 2.11, a linear correlation between the two datasets can be inferred. The MODIS temperature bias for Antarctica is corrected using the relationship from Equation 2.6.

$$T_{MODIS} = 0.86 \cdot T_{MODIS,corrected} - 9.22 \tag{2.6}$$

From studies on Greenland temperatures by Reeh (1989); Steffen and Box (2001) it was possible to find some in-situ temperature measurements for Greenland and compare them to the MODIS temperature measurements (Figure 2.11b). This confirms the results from Antarctica regarding the nature of the bias, but not quite its magnitude. There are very few data points available to obtain a reliable result for the bias correction, but when the regression result from this data are applied, the corrected temperatures agree with the values calculated from the relationship from Ohmura (1987) (Figures 2.8a and 2.12b). Since the regression relation was derived from data that was included in *both* empirical temperature models introduced earlier (Equations 2.3 – 2.5), and no means to independently validate the datasets are available for this work, Equation 2.7 is used to correct MODIS temperatures for Greenland.

$$T_{MODIS} = 0.88 \cdot T_{MODIS,corrected} - 4.84 \tag{2.7}$$

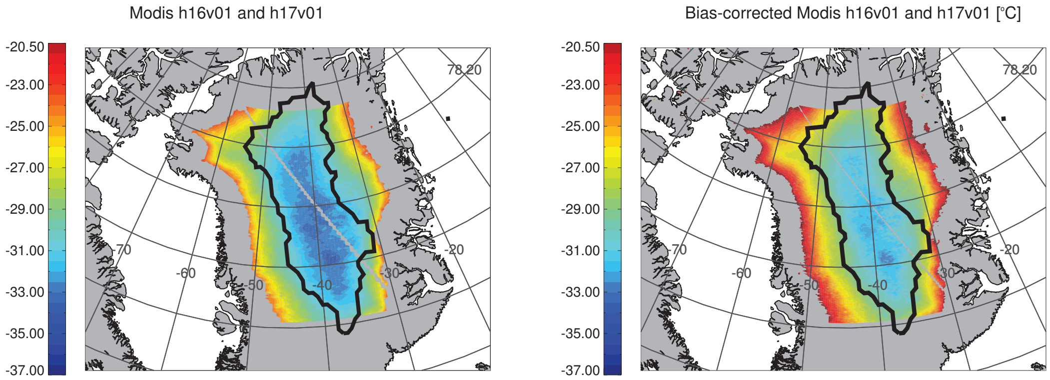

(a) *MODIS temperatures*

(b) *Bias-corrected MODIS data for the dry snow zone of Greenland*

Figure 2.12: *MODIS data for Greenland*

2.4 Low-Resolution Microwave Data

Both active and passive microwave measurements of the ice sheets are examined regarding their potential for accumulation rate retrieval. This section introduces the passive microwave and scatterometer datasets, and even though the principles of measurement differ, the preprocessing steps are very similar and for this reason described together.

2.4.1 Passive Microwave

Passive microwave sensors measure the energy emitted from the earth-atmosphere system in the microwave frequency region. The energy received at the radiometer can be related to the physical temperature of the source using the Rayleigh-Jeans approximation. The physical temperature T multiplied with a material-dependent emissivity $\hat{\epsilon}$ yields the radiometric brightness temperature, T_B (Ulaby et al., 1981).

Brightness temperature images at a daily resolution are generated by the Special Sensor Microwave/Imager (SSM/I)(Maslanik and Stroeve, 1990) and are provided by the NSIDC. SSM/I operates at frequencies of 19.3 GHz, 22.2 GHz, 37.0 GHz, and 85.5 GHz. Datasets are available in horizontal and vertical polarization for every frequency, except at 22.2 GHz, which is only available in horizontal polarization. Data recorded at 85.5 GHz are gridded at a resolution of 12.5 km, data of all other frequencies are gridded at a resolution of 25 km. SSM/I works with a constant incidence angle of 53.1°. Due to the instrument's orbital inclination of 98.8°, regions north of 87.2° N and south of 87° S cannot be covered. The datasets are available in polar stereographic projection. For this work, daily gridded brightness temperature images covering the north and south polar region for the entire year 2006 were used.

2.4.2 Scatterometer

Scatterometers are active microwave systems that transmit pulses to the surface and measure the backscattered power received at the instrument (Ulaby et al., 1981). The SeaWinds scatterometer on QuikSCAT (Long, 2006) measures microwave backscatter σ^0 at a fixed incidence angle of 46°(horizontal polarization) and 54°(vertical polarization). The instrument operates at a frequency of 13.4 GHz. Its orbit is sun-synchronous, at an altitude of 803 km, with an inclination of 98.6°. The resulting data product is an average of the σ^0 measurements over a one-day period[†]. Datasets covering three regions (the entire globe, the northern hemisphere and the southern hemisphere) are available from the Physical Oceanography Distributed Active Archive Center (PO.DAAC). Data products for the polar regions are provided in polar stereographic projection, with a grid size of 22.5 km/pixel. For this work, daily browse images of both the northern and the southern hemisphere, covering the entire year 2006, were selected.

2.4.3 Low-resolution data preprocessing

For the low-resolution passive microwave and scatterometer measurements it is convenient to convert all datasets so that they cover the same spatial extent at the same resolution. For this reason, QuikScat, SSM/I, THERMAP and RAMP datasets are regridded to a 25 km resolution. Although all mentioned datasets are delivered in a polar stereographic projection, different projection parameters are used for each dataset.

The polar stereographic projection is described by three parameters: latitude

---

[†] The data format includes a count of satellite passes for each pixel, with values ranging from 0–50, depending on pixel location.

φ_0 and longitude λ_0 of the projection origin, and the standard parallel (latitude of true scale) φ_1. Transformation to a common reference system is done by an inverse projection of the coordinates to geographic latitude Φ and longitude Λ. Formulas for the polar stereographic projection on the ellipsoid were taken from Snyder (1987).

Since the spatial coverage of the datasets varies, it was necessary to define a common region for the following processing steps. The elevation models provide a useful basis, as they are already limited in their extent to the regions of interest. An algorithm was developed to find the location of the DEM corners in the satellite images and to extract a region of interest equivalent to the area covered by the DEM. For this step, cartesian coordinates were calculated and the minimum distance of satellite image pixels from the DEM corners and the associated microwave image pixel index was determined.

To simplify calculations, the heigth of the surface above the ellipsoid h was neglected. Calculating the error propagation shows that the resulting error in pixel location accuracy never exceeds 4 km[‡] which is far below the resolution of SSM/I and QuikSCAT data.

For the part of this work that uses low-resolution SSM/I and QuikSCAT data, all data outside the region defined by the DEM corners were discarded, and the remaining image was scaled to the resolution of the SSM/I data. Results of this stage of processing are SSM/I, QuikSCAT, temperature and elevation datasets in the same reference system and with the same resolution.

2.4.4 Averaging and filtering of time series

Each SSM/I or QuikSCAT dataset covers an entire year at a temporal resolution of one day. This means that for one pixel location of the low-resolution datasets, there are 365 single measurements and an average value stored for each frequency band. Figure 2.13a shows one SSM/I pixel as an example: the dots represent the daily brightness temperature measurements, while the line shows the annual mean value. To filter outliers from the data, it is necessary to look at the seasonal signal contained in each pixel. A residual brightness temperature ΔT_B is calculated as the difference between adjacent daily $T_B(t)$ values:

$$\Delta T_B = T_B(t) - T_B(t-2) \tag{2.8}$$

[‡] An elevation error of 4 km was assumed in the calculation, which is far too high for the locations of the DEM corner points, which are more likely to be at an elevation close to sea level.

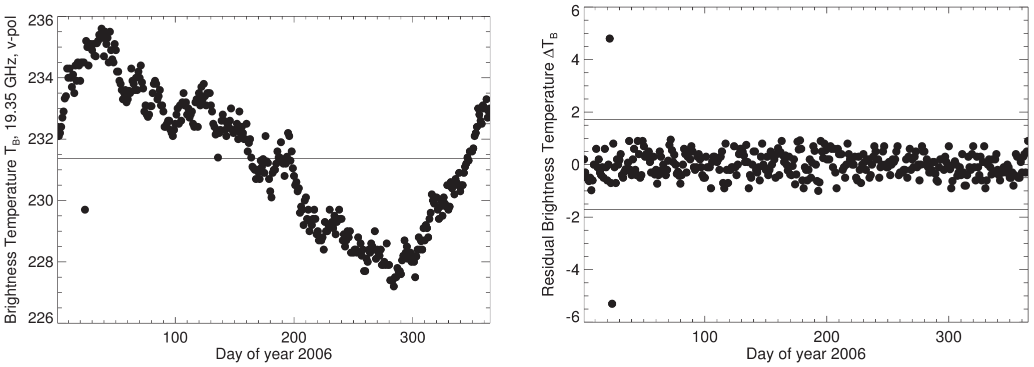

(a) *Sample SSM/I pixel record: dots represent daily T_B values, the line marks the annual mean T_B*

(b) *Residual brightness temperature: dots represent de-trended daily ΔT_B values, lines show the $\pm 3\sigma$ range*

Figure 2.13: *Outlier filter for low-resolution datasets*

This removes most of the seasonal oscillation from the dataset. Now, the standard deviation of the residual brightness temperature, σ_{T_B}, can be determined. All data points outside of the $3\,\sigma_{T_B}$ range are considered to be outliers and are substituted with 4-day averages of their neighboring values.

Figure 2.13b shows the residual brightness temperature ΔT_B and the corresponding $3\,\sigma_{T_B}$ range for the SSM/I pixel record plotted in Figure 2.13a. This example contains a single outlier at day number 23. The simple difference calculation from Equation 2.8 causes the outlier to appear twice in the de-trended dataset, but only the value from the original time series needs to be corrected. The same filtering algorithm was applied to filter outliers from the QuikSCAT data.

2.5 Synthetic Aperture Radar

This section gives a brief introduction to the principles of measurement of synthetic aperture radar systems (SAR) (ESA, 2007; Ulaby et al., 1981, 1982).

Radar systems measure the runtime of a short pulse transmitted by the antenna. The pulse is reflected at the ground and received at the antenna after a small delay caused by its propagation through the atmosphere. This two-way traveltime $\Delta\tau$ can be converted to the slant range distance $\hat{r}_{sr}$:

$$\hat{r}_{sr} = \frac{c\Delta\tau}{2} \tag{2.9}$$

From the incidence angle the ground range distance $\hat{r}_{gr}$ of the received pulse can be calculated:

$$\hat{r}_{gr} = \frac{\hat{r}_{sr}}{\sin\theta} \tag{2.10}$$

If such an instrument were designed to be nadir-looking, it would be impossible to discern between return signals coming from the left or from the right side of the flight track. In order to avoid this ambiguity, side-looking radars are used (Figure 2.14). The resolution δ_{sr} in slant range direction depends on the pulse length τ.

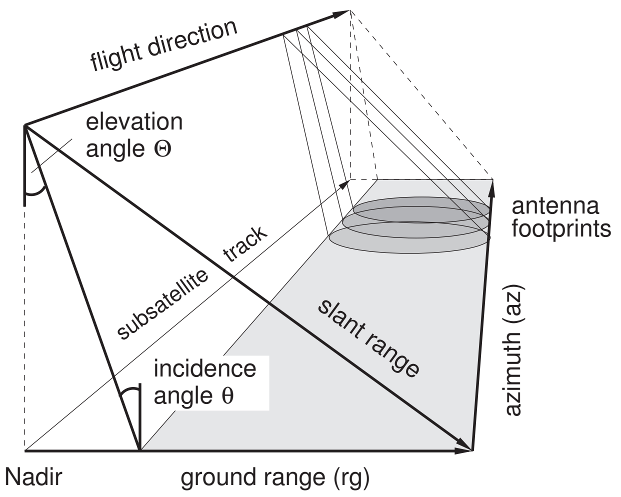

Figure 2.14: *SAR image geometry*

$$\delta_{sr} = \frac{c\tau}{2} \tag{2.11}$$

A higher resolution is achieved by using a shorter pulse to increase the bandwidth B_r. A short pulse length implies that less energy is transmitted and thus means a poorer radiometric resolution due to a decreasing the signal-to-noise ratio. The radiometric resolution can be preserved by generating a long pulse with a linear frequency modulation (chirp) instead of using a small pulse length. The bandwidth-dependent slant range resolution is:

$$\delta_{sr} = \frac{c}{2\,B_r} \tag{2.12}$$

The resolution in ground range δ_{gr} can be calculated using the elevation angle Θ

$$\delta_{gr} = \frac{\delta_{sr}}{\sin\Theta} \tag{2.13}$$

In azimuth direction, the resolution of a system with a real aperture δ_{ra} is determined by the size of the antenna footprint l_{ra}, the wavelength λ and the distance to the target $\hat{r}_0$.

$$\delta_a = \frac{\lambda \, \hat{r}_0}{l_{ra}} \tag{2.14}$$

A synthetic aperture radar measures coherent signals: both amplitude and phase of the return pulses are recorded. Due to the size of the antenna footprint on the ground, a single target is illuminated by several pulses during the sensor's overflight, and has a typical phase history. This effect can be used to generate a "synthetic" antenna with an azimuth resolution δ_{sa} which is independent of the sensors' elevation and depends on the antenna footprint size only:

$$\delta_{sa} = \frac{l_{ra}}{2} \tag{2.15}$$

One very distinct property of SAR images is the grainy appearance of homogeneous areas. Within each SAR pixel, there are multiple scatterers contributing to the signal. Those scattering elements are statistically distributed. All elements' contributions sum up coherently, adding a random part to the received intensity value, which is termed "speckle" (see also Figure 4.1a).

Due to its random nature, speckle cannot be completely removed from a SAR scene, it can only be reduced by averaging over multiple pixels and thus decreasing the image's spatial resolution.

2.5.1 Envisat ASAR

The Advanced Synthetic Aperture Radar (ASAR) instrument on board the Envisat satellite measures radar backscatter at a frequency of 5.3 GHz. Envisat orbits repeat every 35 days, and the satellite's altitude is 786 km. Of the instruments' different image acquisition modes, Wide Swath (WS) and Image Mode Precision Image (IM) products are used here.

Wide Swath images are generated by switching between different swaths during image acquisition, resulting in a 400 km by 400 km image with a spatial resolution of 150 m and a pixel size of 75 m. The ASAR Image Mode scenes cover about 100 km in along-track direction, with different image widths depending on the selected swath (i.e., IS1 to IS7). Incidence angles vary between 15° to 45° (see Table 2.2), and Image Mode datasets have a nominal spatial resolution of 30 m, and a pixel size of 12.5 m. Availabe datasets comprise 17 Wide Swath and 14 Image Mode scenes, all located in Dronning Maud Land, Antarctica (Figure 2.15).

All SAR scenes were averaged by 2×2 pixels to reduce speckle. Further pro-

Table 2.2: *ASAR image acquisition modes. The numbers are from the Envisat ASAR handbook (ESA, 2007)*

Swath	Swath Width [km]	Ground, position from nadir [km]	Incidence Angle Range [°]
IS1	105	187 – 292	15.0 – 22.9
IS2	105	242 – 347	19.2 – 26.7
IS3	82	337 – 419	26.0 – 31.4
IS4	88	412 – 500	31.0 – 36.3
IS5	64	490 – 555	35.8 – 39.4
IS6	70	550 – 620	39.1 – 42.8
IS7	56	615 – 671	42.5 – 45.2

cessing steps for the ASAR data are described in section 2.5.3.

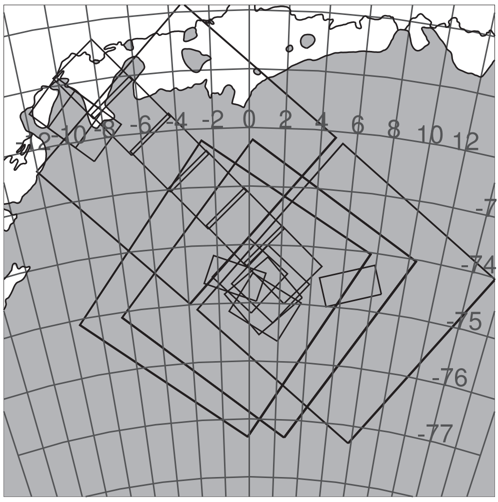

Figure 2.15: *Availabe Envisat ASAR datasets*

2.5.2 Geocoding

Envisat ASAR scenes are geocoded using the Geolocation Grid information from the file header documented by ESA (2007). The process of combining different types of datasets with the ASAR scenes is not as straightforward as for the low-resolution data — storing all needed datasets in memory and referencing data from different sets via shared pixel indices is difficult, because of the large amount of data that would need to be handled.

In order to obtain data from a different dataset for a specific point in a SAR image, a simple pixel location algorithm was developed that determines the minimum distance between the pixel centers of the SAR image pixel and the pixel centers of the supplementary dataset, similar to the procedure used to locate the DEM corners in section 2.4.3. This greatly reduces the amount of computer memory needed and also avoids the need to resample large amounts of data to a different resolution. Pixel location errors caused by this procedure are on the order of 0.5 × SAR pixel size.

2.5.3 Radiometric calibration of SAR images

Envisat Level-1 ASAR images contain intensities (“radar brightness”). In order to determine the radar backscattering coefficients σ^0, the images need to be calibrated. The pixel values DN at position i, j can be converted to σ^0 using a calibration constant $\hat{K}$ and the local incidence angle θ (Rosich and Meadows, 2004):

$$\sigma^0_{i,j} = \frac{DN^2_{ij}}{\hat{K}} \cdot \sin\theta_{i,j} \tag{2.16}$$

The calibration constant can be found in the ASAR file header. The local incidence angle is not known at the time of ASAR product generation, and a ”flat terrain” based on the WGS84 ellipsoid is assumed. Incidence angles with reference to the WGS84 ellipsoid are stored in the Envisat ASAR file headers. Figure 2.16 shows the basic SAR image geometry, and the deviation between ellipsoid and topography surface normals. Those differences can be significant, and therefore local incidence angles are derived from an elevation

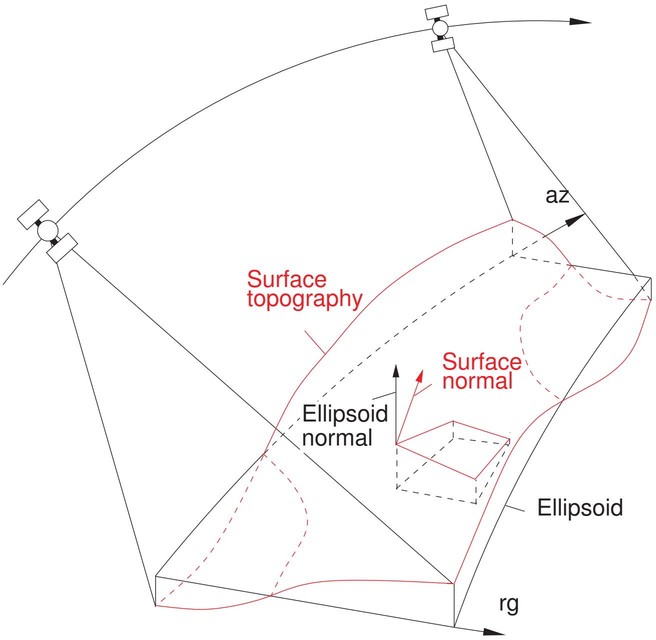

Figure 2.16: *Imaging geometry, local incidence*

model (Wesche, 2009) and used in the ASAR image calibration process. The processing steps neccessary for the integration of local topography data in the radiometric calibration are described in the following sections 2.5.4 and 2.5.5.

2.5.4 Local incidence angle correction

To find the local incidence angle, the elevation model needs to be in the same reference system as the radar dataset. Therefore, the DEM is transformed to the azimuth/range coordinate system of the ASAR image. Since the elevation model is available in polar stereographic projection, it needs to be un-projected to geographic latitude Φ and longitude Λ first (Snyder, 1987). The next step is a coordinate transform from the global reference system $\vec{e}_{wgs}$ to a local reference system $\vec{e}_{sar}$. This is a simple similarity transform, which can be described by three rotations and a translation (Torge, 2001). The local system's origin in the global reference system is denoted by $\vec{x}_{0,wgs}$ and coincides with the origin of the SAR scene. The orientation of the local system's axes is defined by the azimuth and range directions of the SAR image.

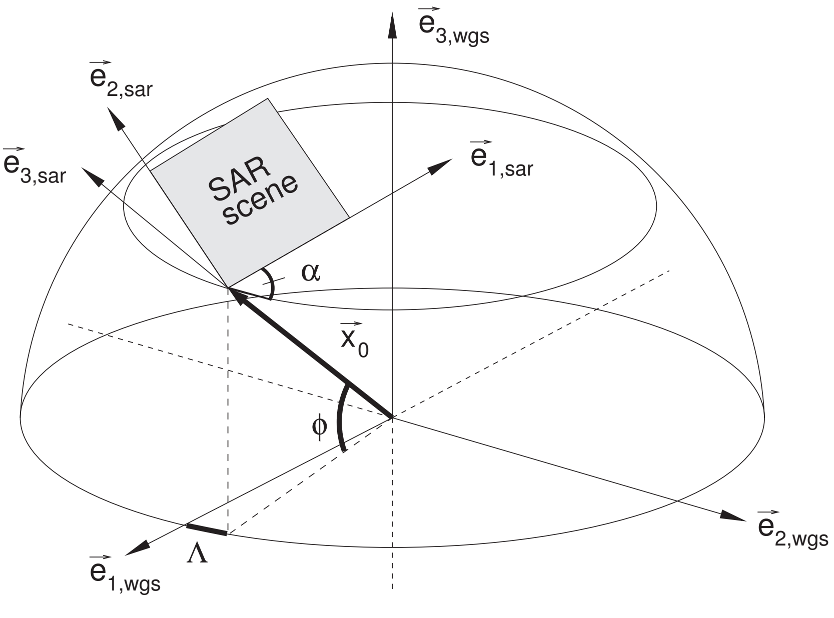

Figure 2.17: *DEM/SAR scene image geometry*

$$\vec{x}_{sar} = \vec{x}_{0,wgs} + \mathbf{R}_3(\alpha) \cdot \mathbf{R}_2(\Phi_0) \cdot \mathbf{R}_3(\Lambda_0) \cdot \vec{x}_{wgs} \tag{2.17}$$

The matrices $\mathbf{R}_i(\gamma_j)$ rotate the system by an angle γ_j around the i-th axis of the respective basis.

$$\mathbf{R}_2(\gamma_2) = \begin{pmatrix} \cos\gamma_2 & 0 & \sin\gamma_2 \\ 0 & 1 & 0 \\ -\sin\gamma_2 & 0 & \cos\gamma_2 \end{pmatrix} \tag{2.18}$$

$$\mathbf{R}_3(\gamma_3) = \begin{pmatrix} \cos\gamma_3 & -\sin\gamma_3 & 0 \\ \sin\gamma_3 & \cos\gamma_3 & 0 \\ 0 & 0 & 1 \end{pmatrix} \tag{2.19}$$

The angles Φ_0 and Λ_0 are the latitude and longitude of the ASAR image origin. The local azimuth angle α can be found in the ASAR file headers. From Equation 2.17, the coordinates of the elevation model grid points are calculated in the ASAR images' coordinate system (Figure 2.18). As a last step of the transformation, the DEM pixels are resampled to the resolution of the ASAR image using the standard IDL Delaunay triangulation and regridding routines.

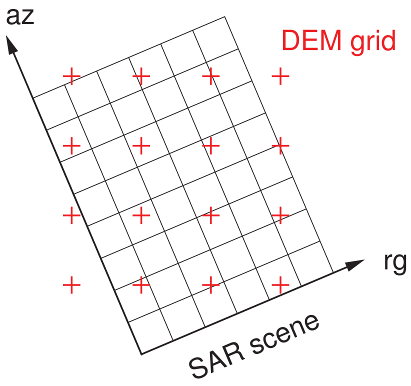

Figure 2.18: *Pixel locations in ASAR image and elevation model*

2.5.5 Terrain slope correction

A radiometric calibration that does not consider local topography (Figure 2.19b) would cause calibration errors of up to 0.5 dB for regions where $|\theta| < 10\,^\circ$ (Ulander, 1995). A terrain slope correction for the incidence angle can be determined from a digital elevation model following Equation 2.1, resulting in terrain slope components in azimuth and range directions θ_a and θ_r. Figure 2.19 illustrates the effect of terrain slope on the local incidence angle for an exemplary ASAR Wide Swath scene. In Figure 2.19a, the elevation model for the image is shown: while most of the terrain is relatively flat, there are some steeper slopes on the northern image boundary. The deviation between the reference ellipsoid normal and the normal vector of the local topography is sketched in Figure 2.20. A local orthonormal basis can be defined by $\vec{e_1}$ and $\vec{e_2}$, which coincide with the azimuth and ground range directions, respectively. The $\vec{e_3}$ direction is equivalent to the reference ellipsoid normal. The incidence angle relative to the reference ellipsoid θ^* between the negative slant range $\vec{k}$ and $\vec{e_3}$ is known from the ASAR image header (Figure 2.20). The surface tilt in azimuth θ_a and range direction θ_r can be easily calculated from the elevation model for every pixel of the SAR image and is shown in Figure 2.21. The

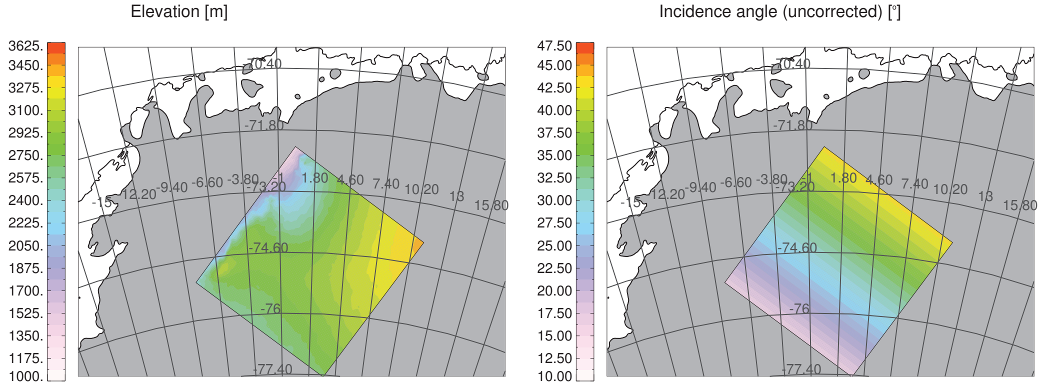

(a) *Elevation (DML DEM)* **(b)** *Incidence (uncorrected)*

Figure 2.19: *Terrain slope effect in Envisat ASAR wide swath image*

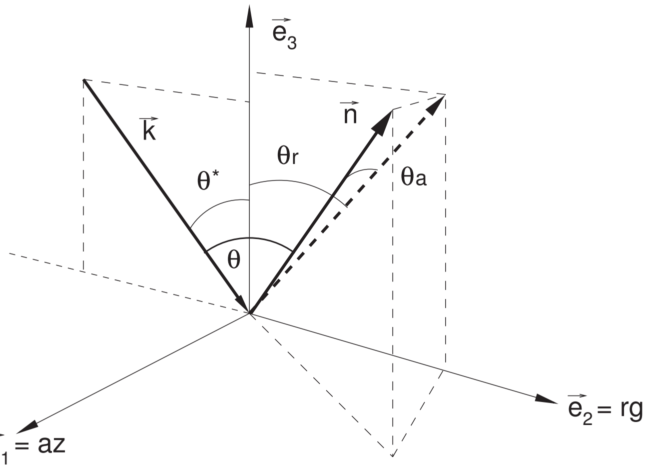

Figure 2.20: *Incidence angle geometry*

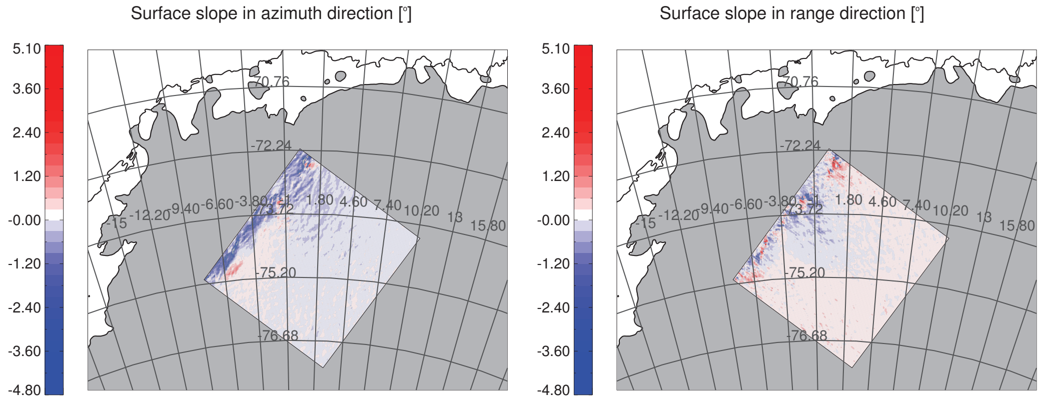

(a) *Azimuth component of local slope* **(b)** *Range component of local slope*

Figure 2.21: *Azimuth and range components of the local terrain slope calculated from the DEM*

negative slant range $\vec{k}$ and the surface normal $\vec{n}$ are:

$$\vec{k} = \begin{pmatrix} 0 \\ k_2 \\ k_3 \end{pmatrix} = \begin{pmatrix} 0 \\ -\sin\theta^* \\ \cos\theta^* \end{pmatrix} \tag{2.20}$$

and

$$\vec{n} = \begin{pmatrix} n_1 \\ n_2 \\ n_3 \end{pmatrix} = \begin{pmatrix} \sin\theta_a \\ -\sin\theta_r \cdot \cos\theta_a \\ \cos\theta_r \cdot \cos\theta_a \end{pmatrix}. \tag{2.21}$$

The local incidence angle θ can be written as

$$\sin\theta = |\vec{n} \times \vec{k}|. \tag{2.22}$$

and is used for a more precise radiometric image calibration in Equation 2.16.

2.5.6 Incidence angle normalization

Radar backscatter properties depend on the incidence angle (Ulaby et al., 1981), and therefore a model of firn-microwave interaction always needs θ as an input parameter. From a practical standpoint it would be convenient to eliminate the angular dependency in the SAR data in order to reduce the computation time of such a model.

For this reason, the angular dependency of backscatter in Envisat ASAR images was examined. From the vicinity of Kohnen station (0 ° E, -75,° S), Antarctica, 23 locations were arbitrarily selected. Backscatter values and incidence angles were determined for each location from all 12 available ASAR scenes covering that area. The plotted σ^0 and θ in Figure 2.22a show a linear relationship, with regression parameters very similar to those found by Rotschky (2007). The slope (IG) of the regression found from the selected points was

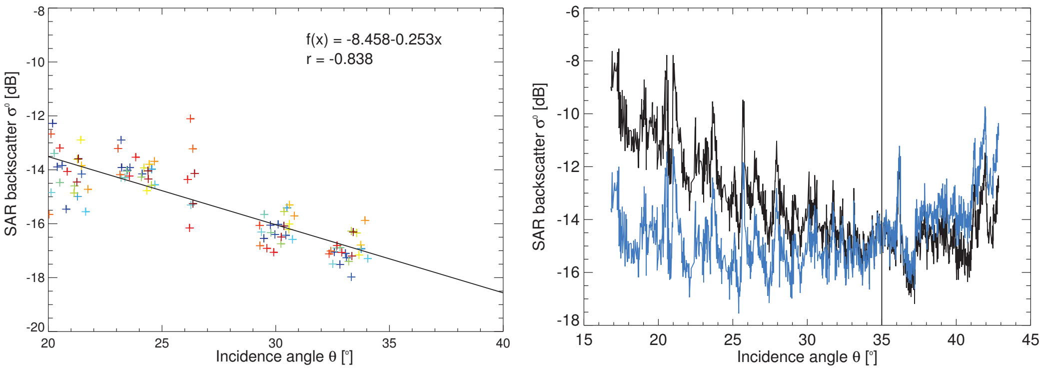

(a) *Angular dependency of SAR backscatter* **(b)** *Row of a SAR image. The black curve shows uncorrected σ^0, and the blue curve shows σ^0 values that are normalized to 35° incidence*

Figure 2.22: *Incidence angle normalization*

then used to normalize the backscatter values to a common incidence angle of 35 °.

$$\sigma^0(35^\circ) = \sigma^0(\theta) + IG(35^\circ - \theta) \tag{2.23}$$

A line in range direction of a SAR image is plotted in Figure 2.22b to illustrate the effect of the normalization process: it can be seen that the correction from Equation 2.23 decreases the angle-dependent backscatter gradient.

2.6 Defining the dry snow zone

The applicability of the accumulation models developed in this work is restricted to the dry snow zone of the polar ice sheets, i.e. to regions that never experience melt conditions. Hence, a criterion has to be found to define its spatial extent.

A possible method for the delineation of the dry snow zone is the ratio P of the horizontally and vertically polarized radar backscatter $\sigma^0_{h,v}$ measurements (Flach et al., 2005):

$$P = \left(\frac{\sigma^0_v - \sigma^0_h}{\sigma^0_v + \sigma^0_h} \right) \tag{2.24}$$

This approach is applied to backscatter images from Greenland and Antarctica to define the dry snow zone.

2.6.1 Greenland

An empirically determined value of $P \leq 0.05$ was given by Flach et al. (2005) as a treshold for determining the extent of the dry snow zone of Greenland. From QuikSCAT annual averages of horizontal and vertical polarization we obtain the polarization ratio image shown in Figure 2.23a. An application of above treshold value then leads to the dry snow zone definition shown in Figure 2.23b, which has been found to be consistent with other sources (Nghiem et al., 2005; Winebrenner et al., 2001; Munk et al., 2003).

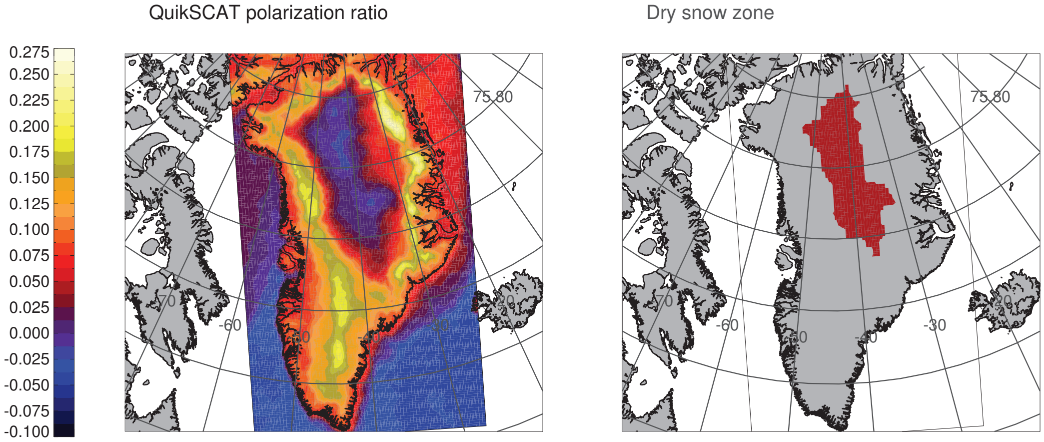

(a) *Polarization ratio* **(b)** *Dry snow zone*

Figure 2.23: *Polarization ratio from annual average QuikSCAT σ^0 values and derived dry snow zone*

2.6.2 Antarctica

The determination of the Antarctic dry snow zone from P is not as straightforward as for Greenland. In central Antarctica, at elevations above 2000 m, large areas with a polarization ratio similar to that of percolation zones ($P > 0.05$) can be found (Figure 2.24a). Since melting can be ruled out in those regions, there must be another cause for these signatures. A comparison with a map of antarctic megadunes (Shuman et al., 2008) shows large agreement between areas with a high P and the location of the megadunes. Megadunes are large-scale undulatuing features on the low-accumulation Antarctic plateau formed by wind redeposition of snow. With wavelengths of 2–5 km and amplitudes of 2–4 m, they are visible from space. One noticeable property of the snow microstructure in the megadune areas is the large variability of snow grain sizes: on the downwind side of the dunes, very large snow crystals with radii up to 1 cm can be found. The upwind side shows very small grain sizes (Courville

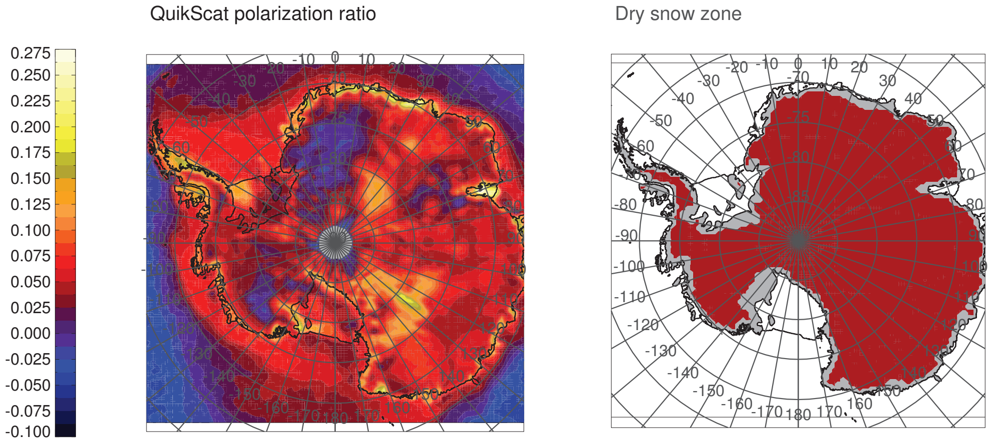

(a) *Polarization ratio* (b) *Dry snow zone*

Figure 2.24: *Polarization ratio from annual average QuikSCAT* σ^0 *values and derived dry snow zone*

et al., 2007).

In radar images, the rough and very hard wind-glazed upwind side scatters much energy back to the sensor, making it appear bright in the image. The downwind regions with their large snow grains absorb more energy and look darker. In the presence of surface scattering, polarization depends on the distribution and orientation of scattering structures on the surface. This could explain the high polarization ratios characteristic for these areas.

If, due to such features, the polarization ratio cannot be used to delineate the dry snow zone, a different criterion needs to be found. It can still be assumed that the polarization ratio treshold is valid along coastal regions of the Antarctic continent.

Since it is only necessary to differentiate between areas with and without occurence of melt in the coastal regions (melt events can be excluded in central Antarctica) the original criterion for melt detection can be used, but has to be complemented by another criterion which avoids mis-classification of areas in central Antarctica. For this purpose, an elevation model helps to classify all points with elevations above 1,500 m as belonging to the dry snow zone (Figure 2.24b). The resulting dry snow zone definition is in accordance with results published on this subject (Rott et al., 1993; Rau and Braun, 2002; Liu et al., 2006; Picard et al., 2007)

3

The microstructure of snow

The following chapter will examine snow microstructure, with a focus on snow properties influencing microwave-snow interaction on the polar ice sheets. Figure 3.1 shows the cross-section of a glacier and its zones of different firn characteristics.

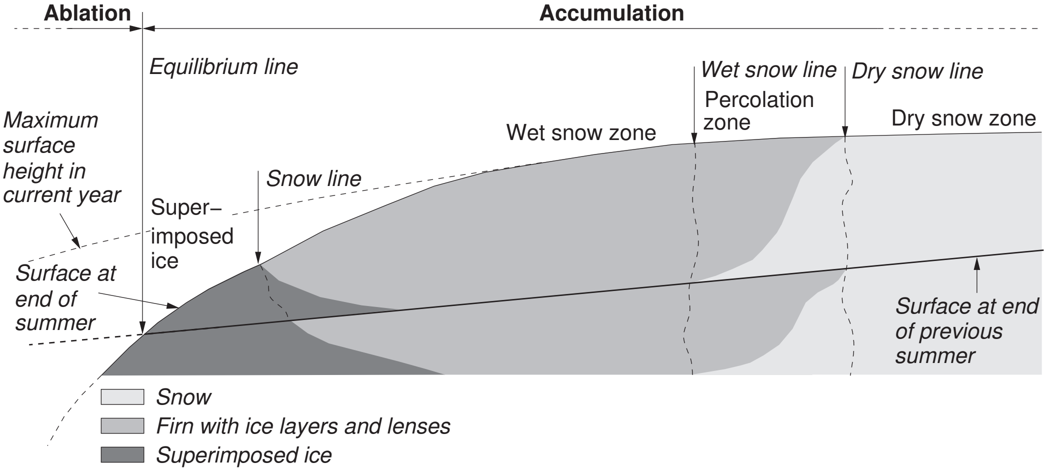

Figure 3.1: *Glacier zones, from Paterson (1999)*

- The **ablation zone** is the region below the superimposed ice zone where more ice is lost due to melting than is formed or transported there. The **superimposed ice** zone is the region below the snow line — the boundary between firn and ice at the end of the melt season. In the **wet snow zone**, all the snow deposited throughout the year reaches the melting point during summer. The content of fluid water in the snow strongly influences its scattering conditions. In the superimposed ice and ablation zones, signals from active sensors are backscattered at the surface when there is fluid water present, and the signal's intensity is determined by surface roughness. In the absence of meltwater, the influence of volume scattering increases, resulting in large variations of backscatter intensity throughout the year. For passive systems, the transition from a volume signal to surface scattering means an increase in brightness temperature, and also an increase in the ratio between horizontal and vertical polarizations, since signals at horizontal polarization are more sensitive to meltwater than at vertical polarization (Abdalati and Steffen, 1997).

- The **percolation zone** is characterized by occasional melt events. Water from surface melt can percolate into the snow and form ice pipes and lenses when it refreezes. In regions where water percolates into an otherwise dry snow pack, scattering from ice pipes and lenses contributes the most part of the signal which also includes a contribution from volume scattering. This results in a relatively low brightness temperature (much of the signal is scattered within the snowpack) (Rott et al., 1993), and in a relatively high σ^0 (much of the signal is scattered back to the sensor). A strong seasonal variability in scattering properties can be observed, it is caused by the melt-induced presence of fluid water within the summer snowpack and the resulting transition from volume scattering to surface scattering.

- **Dry snow zone**: Temperatures here are always below the freezing point, and the snowpack contains no fluid water. Layers of different density and grain size are visible in the firn. The signal return from dry snow regions is caused by scattering within the snow volume, and results from a dielectric contrast between firn layers of different densities at low frequencies or from the contrast between individual ice particles and the surrounding air at high frequencies. Since much of the energy is scattered within the volume, this region appears dark in backscatter images. The amount of stratification of the snow pack (Rott et al., 1993) also influences the brightness temperature polarization ratio — a pronounced stratification leads to a high polarization ratio. V-polarized brightness temperatures are more sensitive to the physical temperature of the firn, while h-polarized brightness temperatures are sensitive to its stratification (West et al., 1996).

  Due to the absence of melt and relatively homogeneous conditions, microwave backscatter images from the dry snow zone display only little

> seasonal variability. It has been found that the seasonal amplitude of brightness temperatures depends on grain size development: larger grains mean lower brightness temperatures (Surdyk, 2002). This implies that regions with a high accumulation rate have a high emissivity, because the snow grains remain smaller (see section 3.1.2). There is also a sensitivity of brightness temperatures to properties of the snow surface: while ice crusts increase the polarization ratio and decrease emissivity, the roughness at the layer interfaces decreases polarization ratio and increases emissivity at low frequencies (Surdyk and Fily, 1995).

Using microwave data, snow accumulation rates can only be indirectly inferred from an interpretation of the different scattering properties of the firn. Those differences are caused by local climate conditions, mainly by temperature, wind and the amount of accumulation. Scattering properties are also very sensitive to the amount of fluid water present in the snow pack, and even small percentages of water significantly reduce the signal's penetration depth. A microwave signal that originates from the surface has no information about the underlying stratigraphy, which means that accumulation rates cannot be derived from microwave data for zones below the wet snow line.

The presence of ice pipes and lenses in the percolation zone leads to a very complex signal which is difficult to model. For this reason, the development of algorithms of accumulation retrieval from microwave data is restricted to the dry snow zone.

For the correct interpretation of microwave images of the polar ice sheets, it is necessary to examine the structure of the firn that generate the signal in more detail. The following section will take a look at processes that occur in the upper tens of meters of the snowpack, where microwave radiation interacts with the firn volume.

3.1 Snow metamorphism

After snow accumulates on the surface by precipitation or wind drift (Figure 3.2b), it begins to settle and densify. Layers form by discontinuous deposition of snow on the surface. The structure of freshly-deposited snow grains quickly begins to change from complex crystals (Figure 3.2a) to more rounded grains (Figure 3.2c). While the snow volume densifies, the grains grow in diameter (Figure 3.2d and 3.2e) until eventually the firn is transformed to glacier ice (Figure 3.2f). The following section gives an introduction to the different processes involved in snow metamorphism, and defines some parameters required for the firn profile model introduced in Section 3.2.

(a) *Freshly deposited snow* **(b)** *Wind-packed snow* **(c)** *Rounded grains*

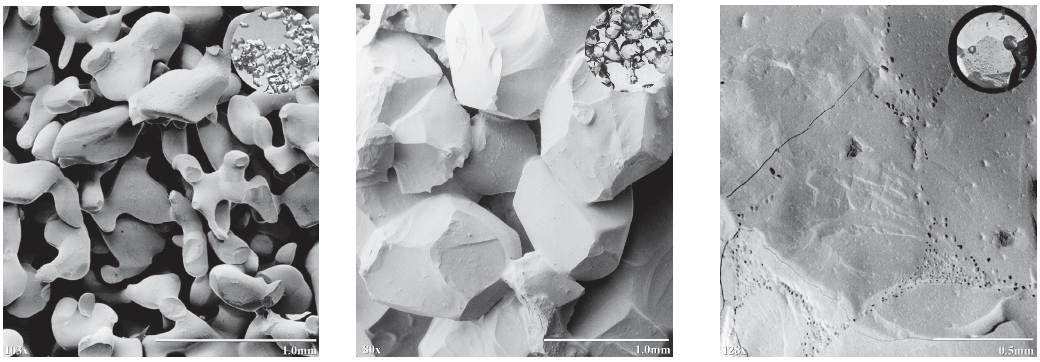

(d) *Sintering between small grains* **(e)** *Glacier firn* **(f)** *Glacier ice*

Figure 3.2: *Transition from snow to glacier ice, image source: Agricultural Research Service, U. S. Department of Agriculture, Electron & Confocal Microscopy Laboratory (2009)*

3.1.1 Densification

Three different densification stages have been discerned (Paterson, 1999). During the first stage, snow densifies by grain-boundary sliding (Alley et al., 1982) until a density approximately equivalent to the maximum packing of random spheres at $\approx 0.55\,\mathrm{g/cm^3}$ is reached (Anderson and Benson, 1963). Bonds begin to form between individual crystals very early in the metamorphism process (Gow, 1975). At this stage, air is exchanged between the snow volume and the surface. During the second stage, the firn densifies by plastic deformation. Here, the pore space between grains is compressed and eventually separated into single air bubbles. The third stage begins at the firn-ice-transition, with densities of 0.82–0.84 $\mathrm{g/cm^3}$, when the pore space is closed off and becomes isolated from the atmosphere (Herron and Langway, 1980). Further densification, up to the density of pure ice, 0.917 g/cm^3, happens by compression of the remaining air bubbles. Figure 3.3 shows two density profiles for different climate conditions. While the accumulation rates at both core locations are of similar magnitude (0.17 and 0.16 m w.e./a), mean annual temperatures are very different: $-47.5\,^\circ$C at the B32 core and $-24.4\,^\circ$C for the B25 core (both from Antarctica). Differences in the densification rate* are attributed to temperature in this example, and can be explained by faster metamorphism processes taking place at higher temperatures (Herron and Langway, 1980; Anderson and Benson, 1963).

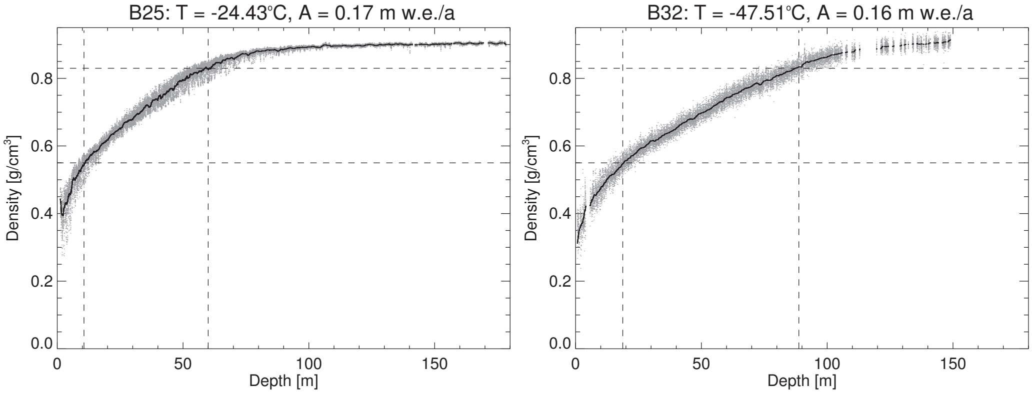

Figure 3.3: *Density profiles of two locations in Antarctica. Dots represent measurements, the solid line is the running mean. Dashed lines mark tresholds at 0.55* g/cm^3 *and 0.83* g/cm^3

Densification models

Different models have been developed to describe the densification of polar firn, they will be briefly introduced here. An empirical parametrization of the densification process was developed by Herron and Langway (1980), using mean temperature and accumulation rate to model mean density profiles. While this model gives good results for Greenland, it fails to accurately represent the density-depth relationship for more extreme Antarctic climate conditions.
A more complex densification model that takes into account the different physical stages was developed by Maeno and Ebinuma (1983), who described densification as pressure sintering driven by excess surface energy and external pressure. Another densification model was published by Arnaud et al. (2000), including grain boundary sliding in the first stage and plastic deformation at later stages.

---

*The term is used here to describe a change in density with respect to depth, rather than time. See also: 3.2.1

All models mentioned above either provide unrealistic results for a wide range of Antarctic climate conditions or rely on a large number of additional input parameters which were often empirically determined and are hence an additional source of uncertainty. For the purpose of this work, a simple empirical parametrization of density profiles depending only on temperature and accumulation rate was developed in order to approximate Antarctic density profiles more realistically. This new approach will be introduced in section 3.2.1.

Density variability

Density records show a significant variability that is due to the stratification of the firn. Alley et al. (1982) noted different densification rates for coarse and fine-grained snow examining a 50 m core from Dome C in East Antarctica. The first high-resolution density records were examined with a focus on density variability by Gerland et al. (1999) and Freitag et al. (2004), who noted that from a maximum at the surface, the variability drops to a minimum at approximately 0.6–0.65 $\mathrm{g/cm^3}$. It rises to another maximum at a density of $\approx$ 0.75–0.85 $\mathrm{g/cm^3}$ and converges on a very low value below the firn-ice transition. This was confirmed by Hörhold et al. (2010) on a total of 19 examined firn cores. Abrupt changes in density between layers cause a dielectric contrast, and microwave sensors working at lower freqencies are sensitive to that (see Chapter 4 for a detailed discussion). Hence it seems useful to incorporate an option to include the density variability in the microstructure model described in more detail in Section 3.2.1.

3.1.2 Grain growth

Seasonal temperature variations propagate into the snowpack and are observed down to a depth of approximately 10 m (Paterson, 1999). The temperature gradient within the upper meters of the firn column causes sublimation in lower layers and condensation in upper layers (Colbeck, 1983). This vertical mass flux is accompanied by the development of interconnections between individual grains. It is also observed that the surface area of the snow grains decreases, while the grain diameter grows (Domine et al., 2008). Layers influenced by temperature variations exhibit a strong grain growth due to the water vapor pressure gradient. Grain growth under isothermal conditions is attributed to energy exchange processes at the grain boundaries (Gow, 1975). The time for the transition from snow to ice strongly depends on the temperature within

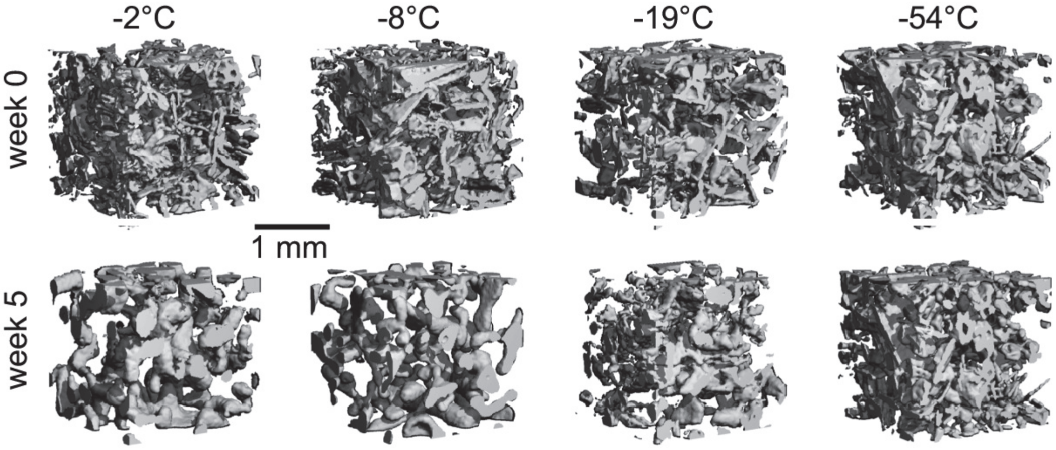

Figure 3.4: *Snow metamorphism (isothermal conditions), excerpt of a series of comuter tomography images from Kaempfer and Schneebeli (2007)*

the snowpack. For lower temperatures there will be less sublimation, resulting in slower grain growth and bonding processes (Figure 3.4).

Various methods for modeling grain growth processes have been described in the literature. Jordan (1991); Colbeck (1983) and Baunach et al. (2001) model temperature gradient growth as a process driven by the saturation vapor pressure gradient. In this case, grains grow only when there is a temperature gradient present within the snowpack, neglecting equi-temperature processes. Flanner and Zender (2006), among others, have created complex 3D models of firn metamorphism that consider physical processes of grain growth in great detail, but require substantial amounts of computation time.

Microwave radiation interacts with the snow volume, and the largest contribution to the measured signal originates from near-surface layers. Therefore it is important that the rapid grain growth in those layers is included in a parametrization of firn microstructure intended as input for a microwave scattering model. In the context of this work, a sufficiently fast, numerically robust and easy-to-implement parametrization of grain size profiles is devised. It will be introduced in section 3.2.3.

3.1.3 Grain size description

A hint to the difficulties of defining a parameter for grain size to be used for modeling purposes can be taken from the large variety of grain shapes and sizes depicted in Figure 3.2. For more densely packed and sintered snow, it is difficult to delineate the borders between single grains or crystals, making the definition of grain size even more arbitrary. Accordingly, grain size descriptions found in the literature are ambiguous (Fierz et al., 2009; Grenfell and Warren, 1999), and can differ significantly in their respective size definitions (Aoki et al., 2000). This makes a validation of grain size model results by comparison with published data very difficult. Table 3.1 summarizes the most common definitions of grain sizes.

Table 3.1: *Grain size definitions*

Type	Definition
Geometrical size	Largest radius
	Mean radius
	Branch width of fresh dendritic snow
	Projected radius (2-D image processing)
Optical equivalent	Sphere of equivalent volume
	Sphere of equivalent surface area
	Sphere of equivalent volume/area ratio

For radiative transfer modeling, it is desirable to use a definition of grain size that relates to the optical properties of the scattering medium. This excludes the use of the geometrical descriptions for this application. Following Domine et al. (2008), an optically equivalent grain size definition is used here. It is based on the specific surface area SSA, which is a measure of the ice-air interface per unit mass:

$$SSA = \frac{S_d}{\rho} \tag{3.1}$$

Here, ρ is the density of the firn sample and S_d denotes the surface density, which is the ratio of the total surface and the total volume of a firn sample. The parameters needed to calculate S_d and ρ can be derived from computer tomography measurements (Hörhold, 2010; Freitag et al., 2004). With the density of ice, $\rho_{ice} = 0.917\,\mathrm{g/cm^3}$, the effective radius r_{eff} of a sphere of equivalent volume/area ratio can be calculated:

$$r_{eff} = \frac{3}{SSA \cdot \rho_{ice}} \tag{3.2}$$

For the validation of the grain growth model described in section 3.2.3, above definition of grain size will be used.

3.2 Modeling snow microstructure

Microwave radiation is scattered within a snow volume. The properties of the snowpack determine microwave backscattering or emission characteristics. Homogeneous environmental conditions on spatial scales that are on the order of microwave data pixel sizes are assumed, and a one-dimensional firn profile is used to describe microstructure characteristics.

A vertical firn profile is described by depth z, age t, density ρ, and grain size r. The grain size is defined as an optically equivalent radius, and is thus comparable to the effective grain radius r_{eff} defined in Equation 3.2. The characteristics of the modeled firn profile are determined by a set of initial parameters: the layer thickness l_0, which corresponds to the accumulation rate A, the mean annual temperature $\bar{T}$ and temperature variation at the surface ΔT.

3.2.1 Density and firn age

Assuming a constant accumulation rate, model layers at a semi-annual resolution are generated to parameterize firn age. Considering firn compaction due to compression of the firn under its own weight, the age t at depth z can be written (Munk et al., 2003):

$$t(z) = \int_0^z \frac{\rho(z')dz'}{A \cdot \rho_{ice}} \tag{3.3}$$

Density profiles of polar firn can be modeled using a generic exponential function.

$$\rho(z) = a_0 \cdot \exp(a_1 \cdot z) + a_2 \tag{3.4}$$

Equations 3.3 and 3.4 are solved to give $z(t)$. It is assumed from previous studies introduced in section 3.1.1 that the unknown parameters a_i in Equation 3.4 can be parameterized depending on temperature and accumulation rate. To verify this, all available density records (see Figure 3.5a and Appendix 7) were analyzed with respect to their temperature dependency. Figure 3.5b shows the correlation between temperature $\bar{T}$ and density at different depths. Plotted density values are averaged over a 1-m interval to account for the noise. A linear regression of the data shows a significant correlation between density and firn temperature. The slope of the curve indicates that higher temperatures cause a faster densification of the firn. The effect of the accumulation rate on densification counteracts the effect of temperature: in the upper meters of the

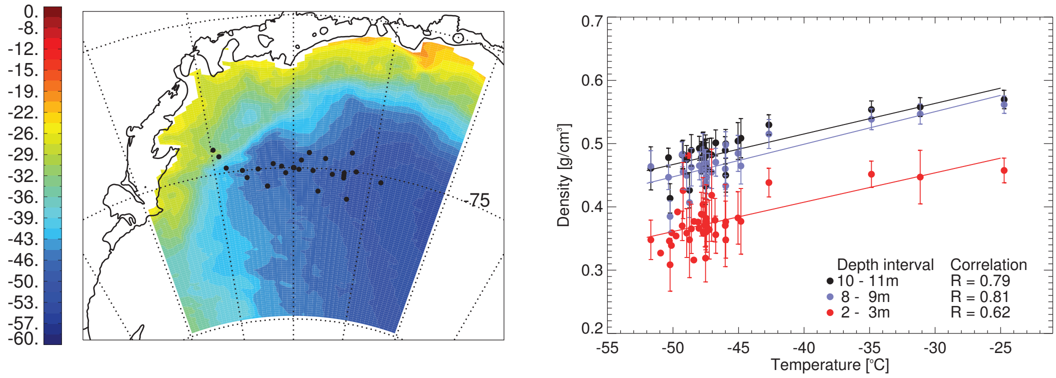

(a) *Dots show core locations, mean annual temperatures from MODIS data (in °C) are color-coded*

(b) *Temperature/density correlation for different depth intervals. Temperatures at the depth intervals are estimated using Equation 3.9 and MODIS data*

Figure 3.5: *Density-temperature relationship.*

firn column, snow densifies mainly by settling of grains. In high accumulation regions, the snow remains within a depth interval for a relatively short time period as it gets buried under fresh accumulation. This gives a snow volume less time to settle before it reaches greater depths. For this reason, both temperature and accumulation are considered in the densification model.

The parameters a_i used in Equation 3.4 to model the density-depth relationship are determined empirically from density records of the 11 ice cores from the dry snow zones of Greenland and DML described in section 2.1.2. Only cores longer than 70 m were considered to reduce the influence of density variability noise on the parameter set. A simple linear dependency between the parameters is assumed:

$$a_i = b_{0i} + b_{1i} \cdot T + b_{2i} \cdot A \tag{3.5}$$

The results from the linear regression are:

$$a_0 = -0.55793 + 0.00127 \cdot T + 0.06621 \cdot A \tag{3.6}$$

$$a_1 = -0.04193 - 0.00054 \cdot T + 0.00257 \cdot A \tag{3.7}$$

$$a_2 = 0.85692 - 0.00271 \cdot T - 0.00417 \cdot A \tag{3.8}$$

When comparing the parametrization for the a_i with values derived from density profiles, it can be seen from Figure 3.6 that the linear regression approach is valid.

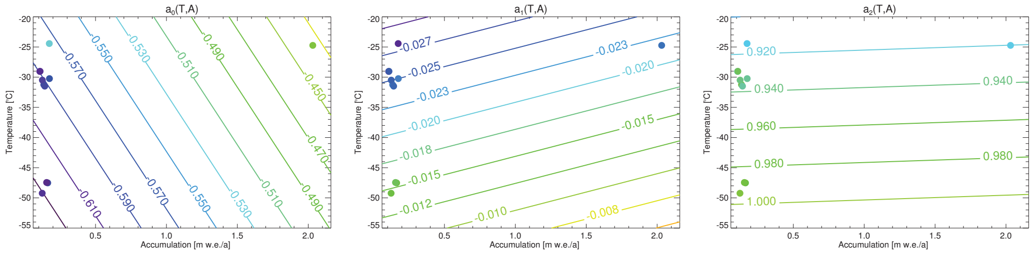

Figure 3.6: *Density parameters fitted to temperature and accumulation rate. Each dot corresponds to the parameters a_i derived from a measured density profile, their absolute values are color-coded on the same scale as the a_i isolines*

Figure 3.7 compares different approaches to model firn densification. Density profiles generated from the new parameter set are compared to the results from the Herron-Langway model and two density profile parametrizations used in other approaches to invert accumulation rates from microwave data (Flach et al., 2005; Munk et al., 2003). The line marked with "exponential fit" in Figure 3.7 shows the results of the newly-derived parameter set. While the results are similar for the B26 core (Greenland, Figure 3.7a), there are large deviations for the B33 core (Figure 3.7b), which is from Antarctica. It can be seen that Equations 3.4–3.8 give more accurate estimates of density profiles for Antarctic climate conditions.

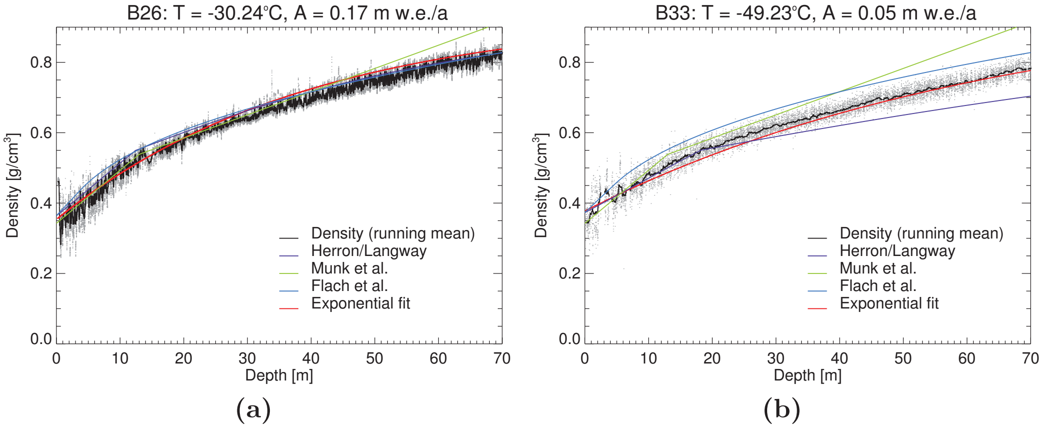

(a) **(b)**

Figure 3.7: *Comparison of firn densification models*

Optionally, a semi-annual variability in the density profiles can be emulated by fitting a spline function with a variability minimum at a density of 0.55 g/cm^3 and a maximum at a density of ≈0.6–0.8 g/cm^3. Parameters for the function are taken from Freitag et al. (2004). Results from the new model are shown in Figure 3.8.

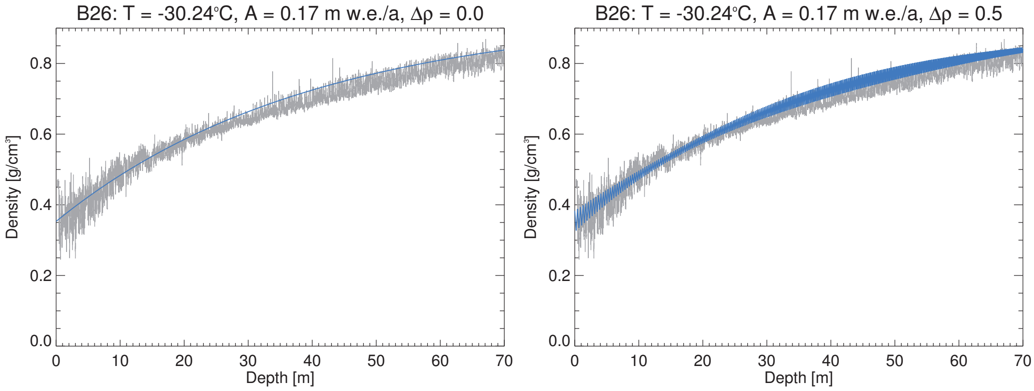

Figure 3.8: *Firn densification, different density variabilities. The grey curves are measured densities, the blue curves are modeled densities using different settings for density variability.*

3.2.2 Temperature

Temperature propagation into the snow pack, $T(z)$, is modeled as an exponentially decaying oscillation as described by Paterson (1999) (Figure 3.9). It depends on mean annual temperature $\bar{T}$, amplitude of the seasonal temperature signal at the surface ΔT, thermal diffusivity of snow k, and frequency ω and phase φ of the seasonal signal.

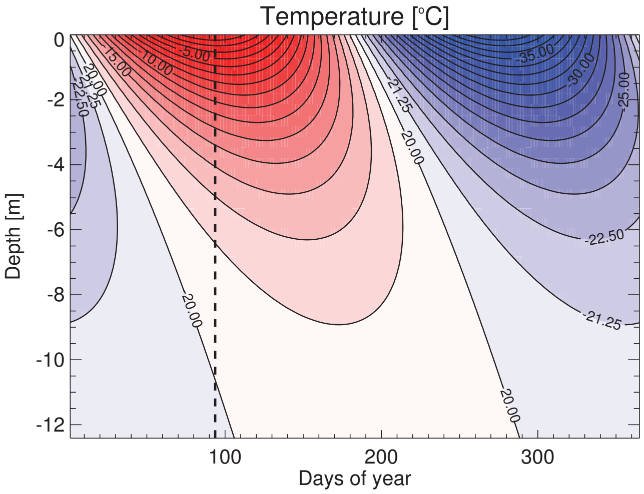

Figure 3.9: *Modeled temperature propagation into the firn. The mean annual temperature in this example is -20°C. The dashed line shows the temperature maximum used to parameterize growth rates in Section 3.2.3*

$$T(z) = \bar{T} + \Delta T \exp\left(-z\sqrt{\omega/2k}\right) \cdot \sin\left(\omega\varphi - z\sqrt{\omega/2k}\right) \tag{3.9}$$

$\bar{T}$ and ΔT can be obtained from MODIS land surface temperature measurements. The thermal diffusivity is calculated from thermal conductivity $\hat{\kappa}$, specific heat capacity of ice $\gamma = 2.009\,\mathrm{kJ}(\mathrm{kg}\cdot{}^\circ\mathrm{C})^{-1}$ and modeled densities using the empirical approach developed by Sturm et al. (1997):

$$k(z) = \frac{\hat{\kappa}(z)}{\rho(z) \cdot \gamma} \tag{3.10}$$

$$\hat{\kappa}(z) = \begin{cases} 0.138 - 1.01\,\rho(z) + 3.233\,\rho(z)^2 & \text{if } 0.156 \leq \rho \leq 0.6 \\ 0.023 + 0.234\,\rho(z) & \text{if } \rho < 0.156 \end{cases} \tag{3.11}$$

The phase value of Equation 3.9 is shifted to match the seasons. The amount of days for the phase shift is determined from the seasonal temperature cycle in the MODIS data.

3.2.3 Grain size profiles

Snow grain growth can be described as a pressure sintering process (Maeno and Ebinuma, 1983), and there are many examples in the literature where the Arrhenius equation (3.12 –3.13) is used to model grain growth as a function of depth z, e.g. by Alley et al. (1982); Gow et al. (2004); Flach et al. (2005). The Arrhenius equation assumes linear particle growth under *isothermal* conditions:

$$\begin{aligned} r^2(t) &= Kt + r_0^2 \qquad (3.12) \\ K &= K_0 \exp(-E/RT) \qquad (3.13) \end{aligned}$$

If the temperature within the snow pack is constant, then the growth rate K in Equation 3.13 is constant for the entire firn profile length, leading to a linear particle growth over time. When the temperature is *not* constant over the profile length, the growth rate is no longer a constant and, due to the exponential term in Equation 3.13, leads to a strongly non-linear particle growth. This behaviour is consistent with observed grain growth, although the Arrenius Equation is not a physically correct description of the actual snow metamorphism processes (see section 3.1.2).

The age-dependent grain radius $r(t)$ of a particle is determined from initial radius r_0 and growth rate K, which is a function of rate constant K_0, activation energy E, gas constant R and absolute temperature T. Reported values for E vary between 47.0 $\times 10^3$ J/mol (Gow, 1969) and 42.4 $\times 10^3$ J/mol (Paterson, 1999). Values found for the rate constant K_0 are very variable, ranging from 1.86×10^{-2} mm^2/a (Budd and Jacka, 1989) to 6.75×10^7 mm^2/a (Flach et al., 2005). Growth rates calculated from the above range of parameters differ considerably. Budd and Jacka (1989) described E and K_0 to be temperature-dependent, and Jacka and Li (1994) supply parameters to fit activation energy E and growth rate K to temperature.

Growth rate

Since the signal measured at the sensor is sensitive to grain size (Shi and Dozier, 2000), the strongly non-linear particle growth in the upper firn layers influenced by the seasonal thermal gradient needs to be considered to approximate a realistic grain size profile. Also, reported K and E vary to such an extent that grain sizes calculated from above values can become quite arbitrary, so a new parametrization based on the measured grain size profiles introduced in section 2.1.3 is developed in the context of this thesis.

As a first step, the temperature profile of the firn column $T(z)$ is simulated using the annual mean temperature $\bar{T}$ and temperature amplitude ΔT. During an (idealized) annual temperature cycle, there are two extreme points: a temperature minimum at the surface in winter and a maximum in summer, both assumed to have the same amplitude (Figure 3.9). The amount of sublimation that drives grain growth depends on the temperature gradient, but also on the absolute temperature value. At the point of the temperature minimum, the growth rate is therefore lower than at the temperature maximum. The observed particle size sums up the influence of the entire temperature cycle a snow grain was subjected to, with the stronger summer growth rate dominating the growth process. This is considered in the following by setting the phase value of Equation 3.9 to the time of the temperature maximum.

Next, the parameterization of grain growth is based on the measured grain size profiles. Looking at the measured grain sizes, no significant correlation between growth rate and accumulation rate can be found, and therefore $K(T)$ is modeled to depend on temperature only. Since the measurements of the effective grain size are available for each firn core in steps of 2.5 cm, with 16 to 20 single measurements repeating in 1-meter intervals to capture grain size variability, the single radii are averaged over the measurement intervals to determine a mean grain size profile. The firn age $t(z)$ corresponding to the mean radius at depth z was estimated from Equation 3.3. Temperatures for each depth interval are calculated according to Equation 3.9, with input values obtained from MODIS data.

Input data for the determination of the growth rate are the average grain size profiles with corresponding values for temperature, density and firn age.

The growth rate $K = dr/dt$ is determined numerically for every 1-m interval. An exponential temperature dependency of K is assumed, and coefficients for Equation 3.14 are calculated.

$$K(T) = c_0 \exp\left(c_1[1000/T(z) + c_2]\right) \tag{3.14}$$

A comparison of growth rates determined from the new dataset with values published by Paterson (1999) shows the values derived from Equation 3.14 to be in good accordance (Figure 3.10), though systematically larger. Growth rates published by Paterson were determined at depths below 45 m, or even below the firn-ice transition, which is not the case for the measurements available for this work. This would explain the lower growth rates in comparison with data from the upper firn layers that are still influenced by seasonal and diurnal temperature variations. Another source of bias again comes from different grain size definitions. The following parameter set was used to estimate the rate of particle growth:

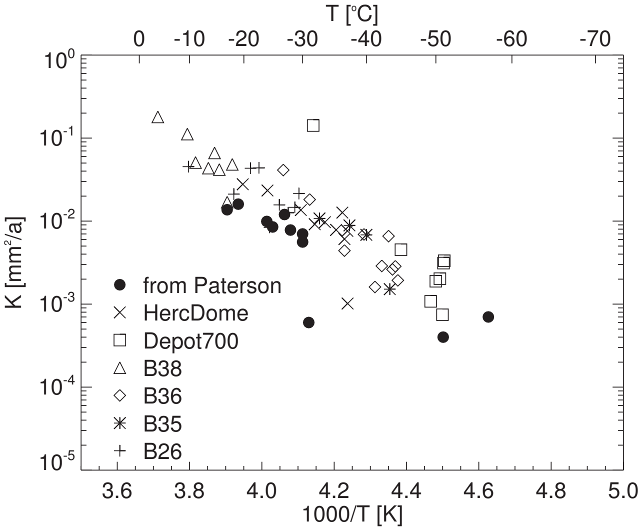

Figure 3.10: *Growth rates derived from profile data, compared with values published by Paterson (1999)*

$$\begin{aligned} c_0 &= 0.165 \\ c_1 &= -5.218 \\ c_2 &= -3.712 \end{aligned} \tag{3.15}$$

Surface grain size

In the literature, the initial grain size parameter r_0 in Equation 3.12 is either set to an arbitrarily fixed value, or there is no value given at all. From the available microstructure dataset, a dependency between surface grain size and climate conditions can be observed. Theoretical considerations confirm that the surface grain size r_0 depends on both temperature *and* accumulation rate: high temperatures correspond to more water vapor transport and thus to faster grain growth. Higher accumulation reduces the time the snow grains are subject to a strong temperature gradient and thus slows down the grain growth process.

To quantify the temperature and accumulation dependency of the surface grain size, initial radii r_0 and their standard deviation σ_{r_0} were estimated from the upper 30 cm interval of each individual profile. The depth interval size was set empirically to balance the noise from the grain size variability against the bias resulting from grain growth. This was done for all available grain size profiles except the Dome C profile since it starts at a depth of 6 m. A multiple linear regression applied to the data from table 3.2 yields the following relationship between initial grain radius r_0, mean annual temperature $\bar{T}$ [°C] and accumulation rate A [m w.e./a].

Table 3.2: *Initial grain size measurement characteristics. Temperatures were obtained from MODIS data, all other data derived from Hörhold (2010)*

Name	r_0 [mm]	σ_{r_0} [mm]	$\bar{T}$ [°C]	A [m w.e./a]
B26	0.40	± 0.033	-31.60	0.180
B35	0.30	± 0.035	-44.60	0.067
B36	0.28	± 0.028	-44.60	0.067
B38	0.20	± 0.010	-18.10	1.250
Depot700	0.25	± 0.043	-51.00	0.045
Hercules Dome	0.35	± 0.029	-37.00	0.180

$$r_0(\bar{T}, A) = d_0 + d_1\bar{T} + d_2 A \tag{3.16}$$

with

$$\begin{aligned} d_0 &= 0.781 \pm 0.019 \\ d_1 &= 0.0085 \pm 0.002 \\ d_2 &= -0.279 \pm 0.055 \end{aligned} \tag{3.17}$$

In order to test the accuracy of the fit, initial radii determined from Equation

3.16 are compared to measured values. Figure 3.11 shows that the multiple regression approach used in this work reproduces the measured values with sufficient accuracy.

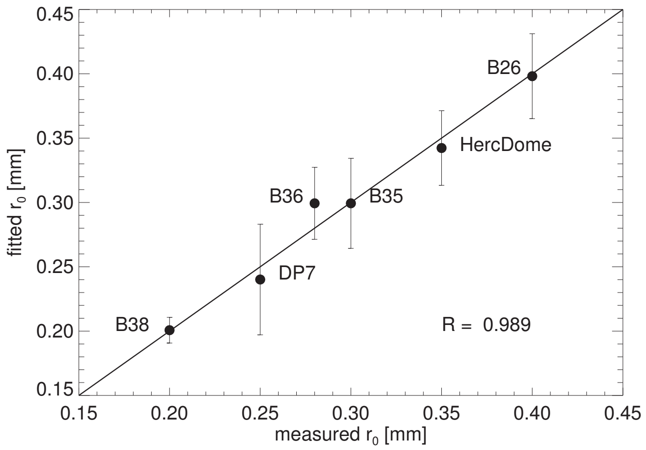

Figure 3.11: *Correlation between simulated and measured surface grain sizes*

Grain size model results

Figure 3.12 shows model results in comparison with grain size models from Flach et al. (2005) and Zwally and Li (2002). It can be seen that the rapid grain growth in the upper layers influenced by a strong temperature gradient is represented more realistically. The approach chosen here overestimates grain growth for B38, a site with an extremely high accumulation rate of 1.25 m water equivalent per year and a comparably high mean annual temperature of -18°C. For the Depot700 core, the extreme grain growth caused by a very low accumulation rate of ≈ 0.045 m water equivalent per year and, in consequence, the long exposure time of snow layers to a large temperature gradient, is underestimated by the new model (Hörhold, 2010). For intermediate polar climate conditions, the simulated grain size profiles are in good agreement with the measurements.

Even though the grain size model does not accurately reproduce grain sizes at very extreme conditions, it yields more realistic results than the other approaches considered previously. The model's accuracy is limited by the availability of grain size measurement, though.

Due to the limited length of the measured profiles, there is currently no way of estimating the modeled grain size profiles' validity for depths greater than approximately 20 meter, but this is sufficient for the purpose of this work. Models of firn-microwave interaction have to consider only the region of the firn column

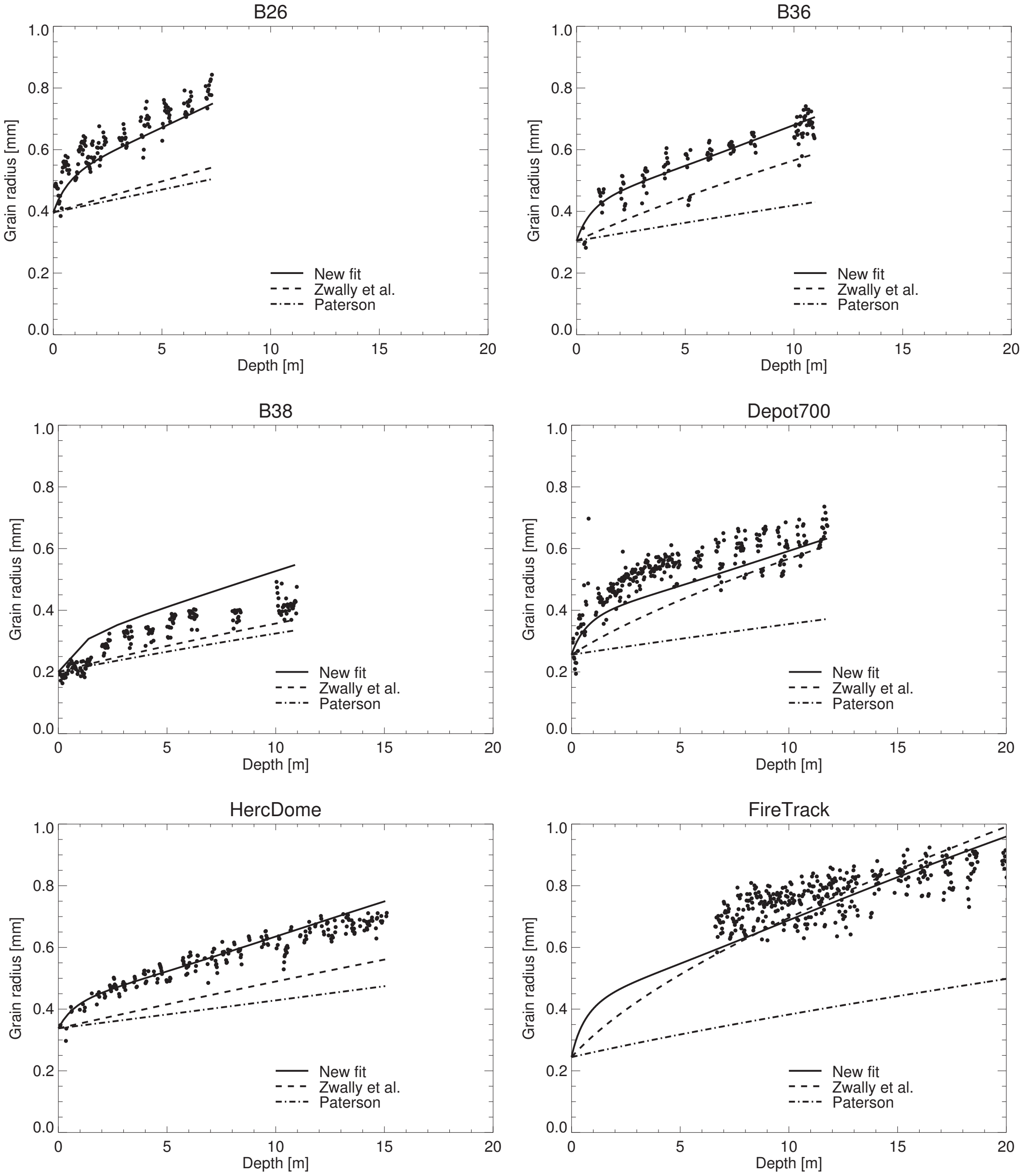

Figure 3.12: *Modeled grain size profiles for all six polar firn cores, in comparison with measured values. Dots represent measurements, and the lines show model results from the different sources listed in the plots*

that interacts with the radiation. Table 4.1 lists the signal penetration depths for the wavelengths of the sensors used here. For all frequency ranges, with an exception of the C-band, penetration depths are estimated to be smaller than 20 m, and even if the scatterer profiles became more unrealistic at greater depths, the main contribution to the signal comes from the upper layers of the firn column, making the contribution of the error introduced by an inaccurate grain size profile at greater depths less prominent (see section 4.3.2 for a more detailed discussion).

4

Interaction of electromagnetic waves with firn

Both active and passive microwave sensor systems are sensitive to firn microstructure properties. At lower frequencies, reflections at layer interfaces constitute the largest part of the signal, while at higher frequencies, the signal is scattered at the ice-air interface of individual snow particles (West, 1994). Electromagnetic radiation is scattered or reflected if there is a dielectric contrast between two different media. In a very simple example, the first medium is air and the second medium is the snow pack below. Depending on the electromagnetic properties of the ground and the instrument's frequency, the radiation can be scattered, absorbed and reflected directly at the surface or within the volume of the second medium. The properties of the snow pack also determine the ratio between scattering and absorption. This chapter introduces the basic theoretical background of microwave scattering and emission.

4.1 Active microwave remote sensing

An active microwave sensor (radar or scatterometer) consists of an antenna that sends out a pulse of energy and measures the returned amplitude and phase of the signal. The radar equation relates the received (measured) power P_r to the transmitted power P_t.

$$P_r(\varphi_s, \vartheta_s) = \frac{\lambda^2}{(4\pi)^3} \int_{\hat{A}} \frac{P_t(\varphi_i, \vartheta_i)\; G_t G_r}{R^4} \; \sigma^0_{rt}(\varphi_s, \vartheta_s, \varphi_i, \vartheta_i)\, d\hat{A} \qquad (4.1)$$

On interacting with the scattering medium, part of the energy is absorbed, and part of it is scattered at the dielectric discontinuity, depending on the electromagnetic properties of the snow pack and the radar wavelength. The resolution cell area $\hat{A}$ consists of many scattering elements, and the received power is integrated over all elements comprising the resolution cell (see Figure 4.1a).

The bistatic scattering coefficient σ^0_{rt} is a function of the scattering characteristics of the area illuminated by the radar beam, the radar wavelength λ, azimuth angle φ_i and angle of incidence ϑ_i and the angles φ_s and ϑ_s at which the signal is scattered (Figure 4.1a). The σ^0_{rt} term includes contributions from the surface as well as from volume scattering, reaching the antenna through area $\hat{A}$.

If only the part of the signal that is scattered back into the direction of the antenna is considered, i.e. if $\vartheta_s = \vartheta_i = \theta$ and $\varphi_s = \varphi_i + \pi$, the parameter is called *backscattering* coefficient $\sigma^0(\theta)$. This quantity is related to the intensity recorded by the receiving antenna (Massom and Lubin, 2006). The sensors used in this work transmit and receive either horizontally or vertically polarized signals, resulting in four possible combinations of polarization: σ_{hh}, σ_{hv}, σ_{vh} and σ_{vv} (Figure 4.1b). The combination of different polarizations can give additional information about the properties of the snow, for instance about scatterer anisotropy and orientation.

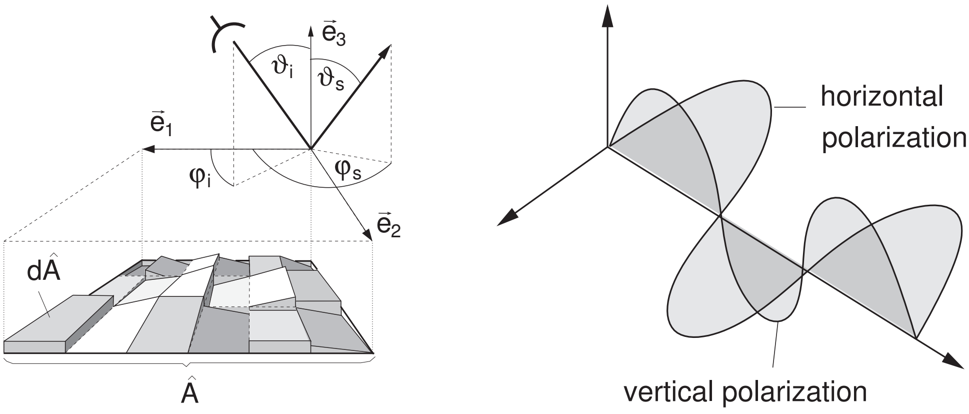

(a) *Radar equation geometry: resolution cell, incident and scattering angles*

(b) *Horizontal and vertical polarization*

Figure 4.1: *Radar imaging properties*

4.2 Passive microwave remote sensing

Planck's radiation law states that the spectral brightness of a blackbody B_b depends on frequency f and physical temperature T (Ulaby et al., 1981). In Equation 4.2, c is the velocity of light, $\boldsymbol{h}$ is Planck's constant, and $\boldsymbol{k}$ is Boltzmann's constant.

$$B_b = \frac{2\boldsymbol{h}f^3}{c^2}\left(\frac{1}{\exp(\boldsymbol{h}f/\boldsymbol{k}_bT)-1}\right) \tag{4.2}$$

If $\boldsymbol{h}f/\boldsymbol{k}_bT \ll 1$, which is the case in the microwave frequency region, the Rayleigh-Jeans approximation of Planck's law is valid. In this case,

$$B_b = \frac{2\boldsymbol{k}T}{\lambda^2}. \tag{4.3}$$

A direction-dependent, blackbody-equivalent temperature can be defined so that the brightness of a snow volume, $B_v(\phi_s, \vartheta_s)$, is

$$B_v(\theta, \phi) = \frac{2\boldsymbol{k}T_B(\phi_s, \vartheta_s)}{\lambda^2}. \tag{4.4}$$

Equations 4.3 and 4.4 are combined to relate the emitted brightness temperature T_B to the physical temperature T:

$$T_B(\phi_s, \vartheta_s) = \Upsilon(\phi_s, \vartheta_s) \cdot T + T_B^{atm}. \tag{4.5}$$

When considering remote sensing data, the main contributions to the measured brightness temperature are the physical temperature of the snow layer and the emissivity of the snow Υ. The part of the signal caused by scattering in the atmosphere T_B^{atm} is the sum of radiation scattered directly into sensor direction and radiation from the atmosphere reflected at the ground. Since this atmospheric part of the brightness temperature is hard to quantify and is of small magnitude compared to the brightness temperature of the snow, it is often neglected.

4.3 Scattering mechanisms

4.3.1 Surface scattering

Depending on the ratio between wavelength and scatterer size, the signal contribution from volume scattering can become very small. In this case, scattering only happens at the interfaces between air and snow, where a part of the incident radiation is scattered and the rest is transmitted into the snow pack. The roughness of this interface in relation to the wavelength has a large impact on the amount of energy scattered back to the sensor. Surface roughness can be characterized by the correlation length $\hat{l}$ and the standard deviation of the surface heigth variation $\hat{\sigma}$ (RMS heigth). There are different scales of surface

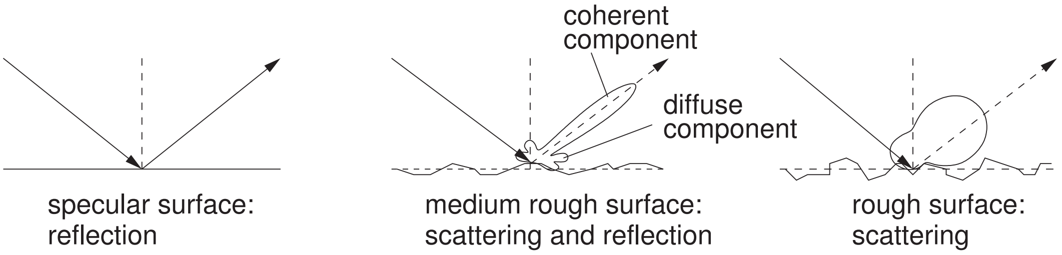

Figure 4.2: *Surface roughness influence on scattering pattern, from Ulaby et al. (1982)*

roughness, depending on wavelength and the system's resolution capabilities. Large-scale roughness caused by topography influences the incidence angle θ, with correlation lengths that exceed the spatial resolution of the instrument. Small-scale roughness directly influences the backscattered intensity due to surface structures on wavelength-scale. According to the Rayleigh criterion, a surface is considered smooth if $\hat{\sigma} < \lambda \cdot (8\,\cos\theta)^{-1}$. For small-scale roughness ($\hat{\sigma} \sim \lambda$), the Fraunhofer criterion is more accurate: in this case, a surface is smooth when $\hat{\sigma} < \lambda \cdot (32\,\cos\theta)^{-1}$.

Scattering processes at random surfaces can be modeled using different approaches, depending on their roughness scale. For surfaces that are relatively smooth, the Small Pertubation Model can be used: the surface is decomposed into its spectral components, and it is assumed that the signal is dominated by Bragg resonance effects which occur at wavelengths λ_B when

$$\lambda_B = \frac{n\,\lambda}{2\,\pi\sin\theta} \quad \text{for} \quad n = \{1, 2, 3, \dots\} \tag{4.6}$$

For higher surface roughness, the Integral Equation Method (IEM) and the geometrical optics approach give more accurate model results (Fung, 1994).

On an interface between media with different dielectric constants ε_1 and ε_2, total transmission of vertically polarized waves can occur at the Brewster angle θ_B:

$$\tan\theta_B = \sqrt{\frac{\varepsilon_2}{\varepsilon_1}} \tag{4.7}$$

At this angle, the reflectivity Γ becomes 0 and the transmissivity Υ equals 1. This makes it interesting for passive remote sensing, since most of the emitted microwave radiation is transmitted to a sensor operating near the Brewster angle. In the case of snow and air, the Brewster angle is approximately at 53°, which coincides with the incidence angle of the SSM/I instrument.

For dry polar snow, the low dielectric contrast between snow and air leads to a low contribution from surface scattering, while volume scattering is more important. Hence, surface scattering is neglected here.

4.3.2 Volume scattering

In the case of a medium composed of different materials, e.g. ice particles mixed with air, the part of the incident energy transmitted into the medium is additionally scattered at the inhomogenities within the volume. A fraction of the energy will eventually be scattered into the sensor's direction. Energy within a volume is scattered in arbitrary directions, resulting in a loss of transmitted power in forward direction. The loss from a combination of volume scattering κ_s and absorption κ_a in the medium per unit length is referred to as the extinction coefficient $\kappa_e = \kappa_a + \kappa_s$. The absorption coefficient κ_a depends on the imaginary part of the dielectric constant, ε''. Extinction properties depend on the distribution of the scattering particles in the surrounding medium, and on their shape and orientation (anisotropy). The volume fraction of scatterers determines whether multiple and coherent scattering effects are significant. Scattering behaviour is also determined by particle size (Figure 4.3). When scatterer sizes are small in comparison to the wavelength, the Rayleigh approximation is used to determine the scattering coefficient κ_s. For scatterer sizes on the order of the wavelength, this approach is no longer sufficiently accurate, and scattering properties are calculated using Mie theory (Ulaby et al., 1981). The applicability of Rayleigh scattering for the combinations of sensor wavelengths and scatterer sizes analyzed in this work is examined in Section 5.1.3.

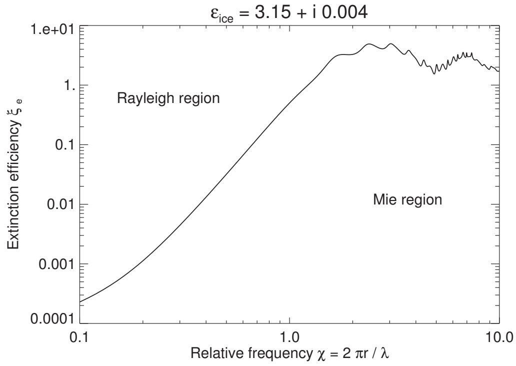

Figure 4.3: *Extinction efficiency calculated for ice particles of different sizes using the Mie scattering model implemented in this work (see Section 5.1.3). ξ_e and κ_e are related quantities. The jitter in the upper right part of the curve is due to numerical noise*

As a consequence of power loss due to volume scattering, a depth can be defined to which volume scattering processes contribute significantly to the signal. This penetration depth d also depends on frequency and scatterer size. It is defined as the depth at which the transmitted power is dampened to $1/e$ of the incident energy and is related to the extinction coefficient.

$$d = \frac{1}{\kappa_e} \tag{4.8}$$

Equation 4.8 is valid only if a constant extinction coefficient is assumed, and in a layered medium it is difficult to determine. Penetration depth can also be approximated using the free-air wavelength λ_0 and the complex dielectric constant of the medium, $\varepsilon = \varepsilon' + i\varepsilon''$.

$$d = \frac{\lambda_0 \sqrt{\varepsilon'}}{2\pi\varepsilon''} \tag{4.9}$$

Typical penetration depths of microwave radiation in polar firn are listed in the Table 4.1.

Table 4.1: *Estimated penetration depths in dry snow*

Band	f [GHz]	λ [mm]	d [m]	Source
C	5.3	57	20-60	Munk et al. (2003)
			20	Rott et al. (1993)
X	9.6	31	8	Rott et al. (1993)
			5	Davis and Poznyak (1993)
Ku	13.4	22	6-7	Legresy and Remy (1998)
K	19.3	16	0.5-4	Bingham and Drinkwater (2000)
	22.2	14	0.1-1	Bingham and Drinkwater (2000)
Ka	37.0	8	0.03-0.3	Bingham and Drinkwater (2000)

Several different approaches to modeling volume scattering or emission exist, and the appropriate method strongly depends on the volume's properties. One possibility is the wave approach, which relies on solving Maxwell's field equations. In this case, the phase information is preserved in the solution. Even though this approach can be rigorously formulated, some approximations need to be made for more complex media to calculate the field solutions.

A simple example is the Born approximation. Here, the dielectric constant is split into a mean part $\bar{\varepsilon}$ and a fluctuating part ε_f: $\varepsilon = \bar{\varepsilon} + \varepsilon_f$ (Figure 4.4b). Then, the mean (coherent) field due to an incident plane wave equals the field transmitted into the medium. This specific method is applicable only for small dielectric fluctuations, but there exist a number of solutions capable of handling stronger scattering. In the wave approach, effects like multiple scattering and interference between layer boundaries can be included at the cost of an increased numerical complexity.

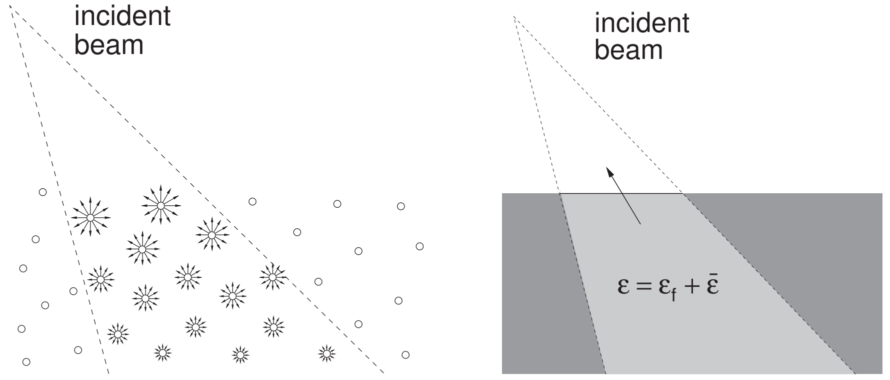

(a) *Discrete scatterers. The length of the arrows indicate the amount of scattered power*

(b) *Fluctuating dielectric constant. Backscattered energy is evaluated at boundary*

Figure 4.4: *Volume scattering*

A different way to model volume scattering is to look at the propagation of energy within the medium using radiative transfer equations. This intensity-based approach ignores interference effects but can include strong dielectric fluctuations. A scattering medium is assumed to consist of discrete scatterers (Figure 4.4a). "Classic" radiative transfer theory considers only independent scattering, allowing volume fractions of up to 5%.

Interference effects between scatterers can be partially accounted for using dense medium radiative transfer theory (DMRT), which allows higher volume volume fractions of up to 40%. In a dense medium, such as polar firn, the scatterer positions are no longer independent of each other. In DMRT, the particle distribution is determined from a pair distribution function, and an effective propagation constant is calculated, allowing the derivation of extinction properties and albedo of the scattering medium (Tsang et al., 1985; Tsang, 1992). An extension to the DMRT accounts for the formation of particle agglomerates, such as the aggregation of ice crystals due to water vapor transport processes, by introducing a "sticky particle" model into the particle distribution function (Tsang et al., 2000, 2007).

5

Radiative transfer modeling of polar firn

During the development of methods to determine snow accumulation rates, various simplified radiative transfer models were introduced. The first attempts were made by Swift et al. (1985) more than 20 years ago, assuming emission in the microwave region from within a homogeneous snowpack with a constant temperature. Later attempts to solve the accumulation problem share the assumption of independent spherical scatterers and the applicability of the Rayleigh approximation with this model.

In the mid-1990's, radar response at different frequencies to different snow and firn characteristics was systematically examined by Jezek et al. (1994) and later verified using ground truth data. It was found that the amplitude of the radar return and signal penetration depth depend mainly on the water content of the snow (Jezek et al., 1993). A simple model of snow layers representing the dry snow pack was developed and integrated into the scattering models by Long and Drinkwater (1994). Later developments include multi-layer scattering (Munk et al., 2003; Drinkwater et al., 2001) and emission models in combination with a complex description of snow stratigraphy to derive snow accumulation rates from microwave remote sensing data. Also, statistical analyses and classification algorithms were included to enhance the accuracy of accumulation estimates (Tedesco et al., 2004; Rotschky et al., 2006).

In order to determine snow accumulation, a backscatter or brightness temperature signal measured by satellite is matched to synthetically generated signals. In the dry snow zone, the signals received by both active and passive radar systems come from within the snow volume. Hence, it is necessary to model snow properties realistically over the depth the sensors can resolve. Modeled snow properties then are used as an input for a multi-layer scattering model.

5.1 Backscatter and brightness temperature models

The radiative transfer equation relates incident to scattered intensity (Tsang et al., 1985).

$$\frac{\partial \bar{\boldsymbol{I}}(\vec{r},\vec{s})}{\partial s} = -\bar{\boldsymbol{\kappa}}_e(\vec{r},\vec{s})\ \bar{\boldsymbol{I}}(\vec{r},\vec{s}) + \boldsymbol{J}_e + \int_{4\pi} \bar{\boldsymbol{P}}(\vec{r},\vec{s},\vec{s}\,')\ \bar{\boldsymbol{I}}(\vec{r},\vec{s}\,')d\Omega' \tag{5.1}$$

Here, $\bar{\boldsymbol{I}}(\vec{r},\vec{s})$ is the incident intensity at point $\vec{r}$ in direction $\vec{s}$. The extinction matrix $\bar{\boldsymbol{\kappa}}_e$ defines intensity loss due to absorption and scattering within the medium, and s is the distance. An emission source term, $\boldsymbol{J}_e$, accounts for intensities radiating from the volume element. The distribution of scattered intensities in all possible directions is expressed by the phase matrix $\bar{\boldsymbol{P}}(\vec{r},\vec{s},\vec{s}\,')$, and the integral expression in Equation 5.1 sums up the scattered intensities from all directions $\vec{s}$ into direction $\vec{s}\,'$.
Assuming spherical particles, the extinction matrix $\bar{\boldsymbol{\kappa}}_e$ reduces to a scalar expression, the extiction coefficient κ_e. Approximations for the phase matrix under the assumption of incoherent scattering and identical scatterer sizes are given e.g. by Tsang et al. (1985). Phase matrices for more complex scattering processes are found e.g. in Ulaby et al. (1986), Wen et al. (1990) and Tsang et al. (2000).

5.1.1 Microwave Backscatter

For active microwave remote sensing, the emission source term in Equation 5.1 is small compared to the contribution from the instrument itself, and is hence neglected. The signal return measured at the sensor is therefore determined by the extinction properties of the underlying medium.
A simple radar backscatter model of a medium consisting of ice particles as scatterers and air as a background medium (Munk et al., 2003) employs Rayleigh scattering theory. Since it is used here to model backscattering coefficients, it is described at this point in greater detail.
The absorption coefficient κ_a is determined from the complex ice permittivity $\varepsilon_{ice} = \varepsilon'_{ice} + i\varepsilon''_{ice}$, the free-air wavenumber k_0, and the volume fraction of scatterers $f_v = \rho/\rho_{ice}$.

$$\kappa_a = k_0\ \varepsilon''_{ice} \left| \frac{3}{\varepsilon_{ice}+2} \right|^2 \cdot f_v \tag{5.2}$$

The scattering coefficient additionally depends on the scatterer radius r and the number of scatterers per unit volume N_v:

$$\kappa_s = \frac{8}{3}\pi \; N_v \; k_0^4 \; r^6 \left| \frac{\varepsilon_{ice} - 1}{\varepsilon_{ice} + 2} \right|^2 \tag{5.3}$$

The number of scatterers per unit volume, N_v, is determined from snow density ρ, the density of pure ice, ρ_{ice}, and the grain radius r:

$$N_v = \frac{\rho}{\rho_{ice}} \left(\frac{4}{3}\pi r^3 \right)^{-1} \tag{5.4}$$

The extinction coefficient is the sum of the absorption and the scattering coefficient

$$\kappa_e = \kappa_a + \kappa_s. \tag{5.5}$$

The backscattering coefficient for a single homogeneous snow layer depends on incidence angle θ, layer thickness d_0, the single scattering albedo of the layer $\omega = \kappa_s/\kappa_e$ and the dielectric loss due to extinction $L = \exp(\sec\theta \cdot \kappa_e \cdot d_0)$ and can be written as

$$\sigma^0 = \frac{\cos\theta \; \kappa_s}{2\kappa_e} \left(1 - \frac{1}{L^2} \right) \tag{5.6}$$

In order to extend this model to a multi-layer case, all quantities contributing to the backscatter coefficient are derived from the physical properties defined for each layer. Subsequently, the resulting values are summed up over the previously defined depth range under consideration of a depth-dependent attenuation factor. The total backscatter can be calculated using a radiative transfer model, which considers single scattering only (Munk et al., 2003).

$$\sigma^0 = \cos\theta \sum_{n=1}^{N} \frac{\omega_n}{2} \left(1 - \frac{1}{L_n^2} \right) \; e^{-2\tau_n}. \tag{5.7}$$

Here, ω_n is the single scattering albedo and the index n denotes the n-th layer. The incidence angle θ is the angle at the surface boundary, and the refraction into the layers is considered in Equations 5.9 and 5.10.

$$\omega_n = \frac{\kappa_{s_n}}{\kappa_{e_n}} \tag{5.8}$$

The term τ_n is an attenuation factor depending on layer thickness d

$$\tau_n = \sum_{j=0}^{n-1} \sec\theta_j \kappa_{e_j} d_j. \tag{5.9}$$

The one-way loss factor L_n accounts for signal loss within the layers

$$L_n = \exp(\sec\theta_n \ \kappa_{e_n} \ d_n). \tag{5.10}$$

Following Bingham and Drinkwater (2000), microwave backscatter σ^0 can also be modeled as the incoherent sum of the return from single spherical scatterers within each layer. A radiative transfer model that includes the transmissivity $\hat{\Upsilon}_{i,j}$ at the layer interfaces is used to determine σ^0:

$$\sigma^0 = \hat{\Upsilon}^2_{0,1}(\theta_0) \ \sigma^0_{v1}(\theta_0) + \sum_{j=2}^{N} \frac{\prod_{i=1}^{i=j} \hat{\Upsilon}^2_{i-1,i}(\theta_{i-1})}{\prod_{i=1}^{i=j-1} L^2_i(\theta_i)} \cdot \sigma^0_{vj}(\theta_j). \tag{5.11}$$

The incidence angle-dependent volume contribution σ^0_{vj} of each layer is calculated using Equation 5.6.

5.1.2 Brightness Temperatures

To determine the brightness temperature of a snow pack, the emission source term in Equation 5.1 needs to be evaluated. If a local thermodynamic equilibrium is assumed, Kirchhoff's law states that emissivity Υ equals absorptivity. In this case, $\boldsymbol{J}_e$ is proportional to the product of the absorption coefficient κ_a and physical temperature T (Tsang et al., 1985). The solution used here calculates the reflectivity Γ to account for absorption within the snow volume

$$\Gamma = 1 - \Upsilon, \tag{5.12}$$

and for a homogeneous half-space with a constant temperature, the brightness temperature would be

$$T_B = (1 - \Gamma) \cdot T. \tag{5.13}$$

The multilayer brightness temperature model developed by Burke et al. (1979) for soil layers was adapted by Bingham and Drinkwater (2000) to be valid for snow and is used here to simulate brightness temperatures of the modeled firn profiles. Emissions from each layer are assumed to be proportional to the mean layer temperature T_j. These temperatures are summed up over N layers, considering signal loss caused by scattering and absorption in each layer, and reflections at layer interfaces. The power reflection coefficient $\Gamma(\theta)$ is used to calculate brightness temperatures T_B as a function of the incidence angle θ:

$$T_B(\theta) = \sum_{j=1}^{N} T_j \left(1 - \frac{1}{L_j(\theta_i)}\right)\left(1 + \frac{\Gamma_{j+1}}{L_j(\theta_i)}\right) \cdot \prod_{i=1}^{j}(1-\Gamma_i) \cdot \prod_{i=2}^{j}\left(\frac{1-\Gamma_{j-1}}{L_{j-1}}\right) + T_{atm} \tag{5.14}$$

A correction term for atmospheric influence, T_{atm}, is of small magnitude and therefore not considered in the calculations. The power reflection coefficient Γ can be derived from the polarization dependent Fresnel reflection coefficients $z_{p,i}$ given by

$$z_{p=h,i} = \frac{\sec\theta_i}{\sqrt{\varepsilon_i}} \tag{5.15}$$

$$z_{p=v,i} = \frac{\cos\theta_i}{\sqrt{\varepsilon_i}} \tag{5.16}$$

$$\Gamma = \left|\frac{z_{p,i+1} - z_{p,i}}{z_{p,i+1} + z_{p,i}}\right|^2 \tag{5.17}$$

5.1.3 Validity of Rayleigh Scattering

In Ulaby et al. (1981), a criterion for sufficient accuracy of the Rayleigh approximation is given. It is defined as $|n\chi| < 0.5$, with the refractive index of the medium n depending on the dielectric constants of the scattering particles ε_p and of the background medium ε_b.

$$n = \frac{n_p}{n_b} = \sqrt{\frac{\varepsilon_p}{\varepsilon_b}} \tag{5.18}$$

The parameter χ depends on the scatterer radius r, the wavelength of the incident wave λ_0 and the real part of the complex dielectric constant of the background medium:

$$\chi = \frac{2\pi r}{\lambda_0\sqrt{\varepsilon_b'}} \tag{5.19}$$

If the scatterer consists of ice and the background medium is assumed to be air, equation 5.18 simplifies to

$$n = \sqrt{\varepsilon_{ice}} \tag{5.20}$$

and equation 5.19 can be written as

$$\chi = \frac{2\pi r}{\lambda_0}. \tag{5.21}$$

Table 5.1: *Validity of Rayleigh approximation. Numbers printed in bold show the combinations of frequencies and particle sizes where the Rayleigh approximation is still valid*

Frequency [GHz]		13.40	19.35	22.23	37.00	85.50
Wavelength [mm]		22	15	13	8.1	3.5
$\lvert n\chi \rvert$	r=2.0 mm	0.997	1.440	1.654	2.753	6.360
	r=1.0 mm	**0.498**	0.720	0.827	1.376	3.180
	r=0.5 mm	**0.249**	**0.360**	**0.414**	0.688	1.590

Table 5.1 lists $|n\chi|$ for wavelengths used by the SSM/I and QuikSCAT sensors and a realistic range of scatterer sizes. From Table 5.1 and Figure 5.1 it can be seen that the assumption of Rayleigh scattering leads to inaccuracies in the result, especially at higher frequencies.

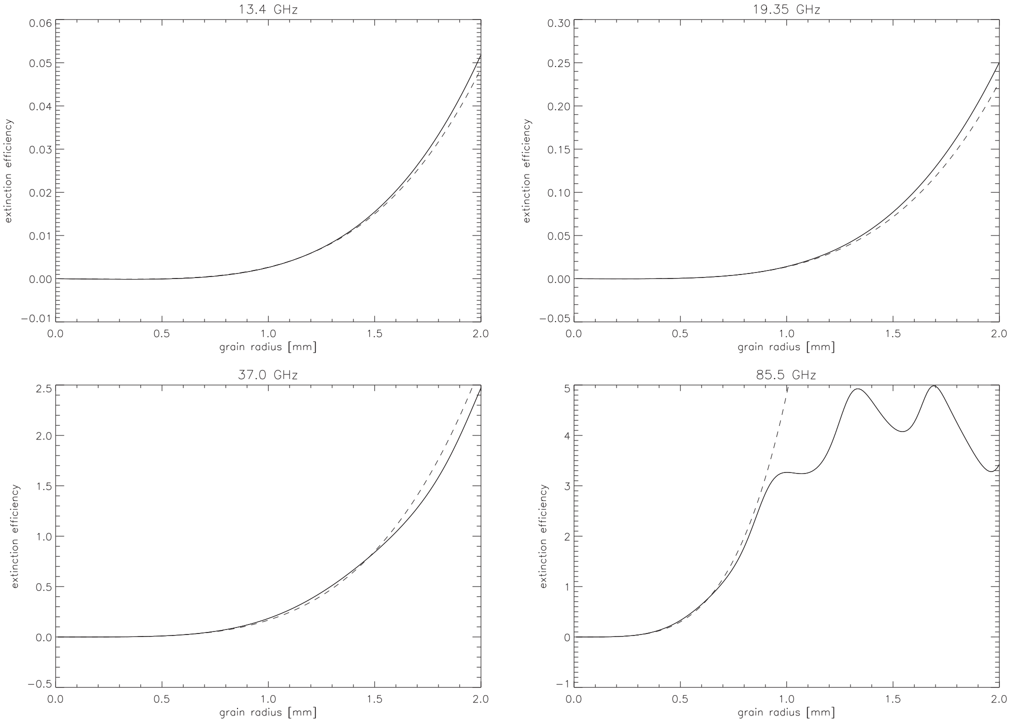

Figure 5.1: *Comparison of extinction efficiencies calculated from Mie and Rayleigh scattering models: the dashed line shows Rayleigh scattering, and Mie scattering is plotted in a solid line*

Using the Rayleigh approximation causes inaccuracies in the results for the entire SSM/I frequency range. Therefore, the Mie extinction efficiency ξ_e is used in this work to calculate κ_e, and to determine the loss factor (Equation 5.10). Mie extinction efficiencies are calculated using the iterative solution described in Ulaby et al. (1981). Results from both the Mie and the Rayleigh solution are discussed in Section 6.2.

Errors in the radiative transfer models (Equations 5.7, 5.11 and 5.14) also result from the assumption of single spherical scatterers, since only far-field interactions between ice particles are considered and coherent scattering effects are neglected.

6

Estimating snow accumulation

In Chapter 3, the properties of the microstructure of polar firn were introduced. It was shown that there is a correlation between microstructure parameters, such as density and grain size, and local climate indicators, e.g. temperature and accumulation rate (Section 3.2). A simple radiative transfer model for dry polar firn was described in Chapter 5, and it was noted that microwave emission or backscatter is sensitive to firn microstructure characteristics. The current chapter integrates the results from both parts and discusses the approach taken in this thesis to quantify snow accumulation. Figure 6.1 provides a schematic overview of the algorithms used in this thesis to invert accumulation rates from microwave satellite data. The model accepts a range of mean annual temperatures and accumulation rates as its initial parameters ①. From this set of values, firn profiles are generated ②. Developing the parameterizations for densification and grain growth as introduced in Section 3.2 required input from field data ③ to describe an empirical relationship between model input values and firn microstructure properties ④. The results of this step are

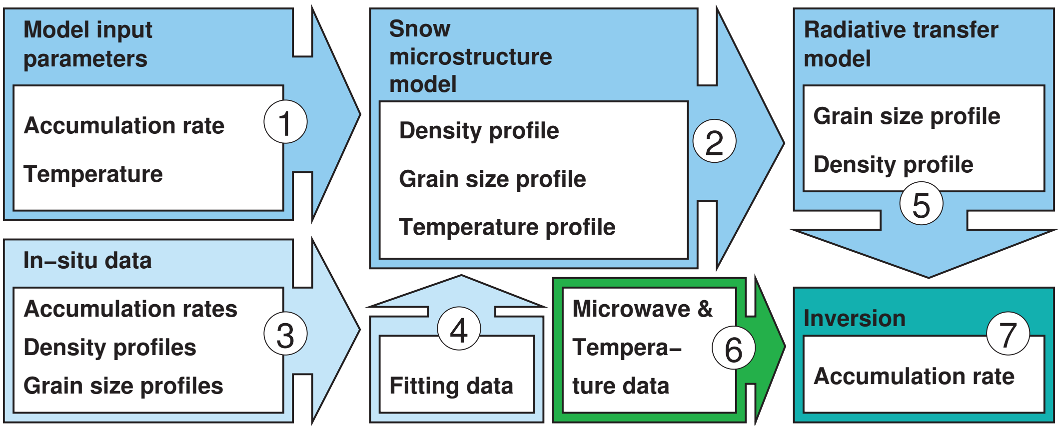

Figure 6.1: *Accumulation retrieval schematic*

vertical profiles of firn microstructure parameters: density, grain size and firn temperature for each combination of surface temperature and accumulation rate. The maximum depth of the profiles depends on the sensor wavelength and is estimated using 2 × the approximate penetration depth (Equation 4.9). Radiative transfer equations are solved for each model representation of the firn column, with scatterer sizes and density as input values ⑤. For each combination of the initial values (mean annual temperatures and accumulation rates), a brightness temperature or backscattering coefficient is calculated for each day of an entire seasonal cycle. They are then stored together with their corresponding initial values. Additionally, mean T_B or σ^0 are calculated from each set of results and included in the dataset. From temperature and microwave data ⑥, the matching accumulation rates can then be inverted ⑦ using the lookup table generated in the previous step.

6.1 Comparison of satellite measurements with in-situ data

In this section, the correlation beween ground truth accumulation measurements and satellite data is evaluated. This can lead to a statement on how well accumulation can be determined using datasets recorded at different frequencies and polarizations. In this work, the satellite signals (T_B or σ^0) are compared to ground-based measurements of accumulation rates.

6.1.1 Low-resolution data

To evaluate the relationship between the absolute values of SSM/I or QuikScat data and field measurements, annual means of T_B or σ^0 are used here, neglecting any seasonal fluctuations of the microwave signal.

Flach et al. (2005) introduced a method to invert accumuation rates from the *amplitude* of the seasonal signal of backscatter and brightness temperatures. Considering this approach, the correlation between seasonal amplitudes from satellite data and accumulation rates is examined more systematically in the context of this thesis. In order to reduce the noise present in the daily measurements of σ^0 or T_B, a moving average filter is applied, and the amplitude is determined from the filtered dataset. A window size of 30 days is chosen to suppress the day-to-day noise while retaining the magnitude of the seasonal amplitude.

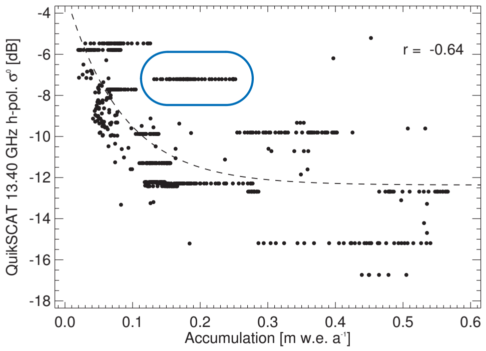

Figure 6.2: *Correlation between ground truth and 13.40 GHz QuikScat data, including the measurements from the Kottas traverse.*

The spatial resolution of the field data from the Kottas traverse (Figure 2.1b) is much higher than that of the SSM/I or QuikSCAT datasets. Including the traverse means that there can be a large number of accumulation measurements within a single pixel. An example can be seen in Figure 6.2, where the blue circle indicates a single QuikSCAT pixel containing a large number of field measurements. The large variability of accumulation rates within a single pixel serves as a good illustration for the problems that occur when point measurements are compared to spatially averaged data.

The following analysis uses only image pixels that contain a similar number of field measurements in order to compare data with similar standard deviations. For this reason, field data from the Kottas traverse are excluded from the evaluation of low-resolution data in this work. For the absolute values of σ^0 or T_B, a function was fitted to the data, but this is intended only as a visual guidance.

Table 6.1: *SSM/I and QuikSCAT noise levels*

Frequency	Noise (h-pol)	Noise (v-pol)	Unit
13.40 GHz	0.79	0.70	dB
19.35 GHz	1.18	0.70	K
22.23 GHz	—	0.86	K
37.00 GHz	1.60	1.01	K
85.50 GHz	6.66	5.20	K

Each σ^0 or T_B dataset has its specific level of noise. The amount of noise was estimated by calculating the standard deviation of the daily values after removing the seasonal trend with the same method as the one used to remove outliers in the data (see Section 2.4.4). The noise levels are listed in Table 6.1. Please note that the values given for the QuikSCAT sensor are on a logarithmic scale.

QuikScat data at 13.40 GHz

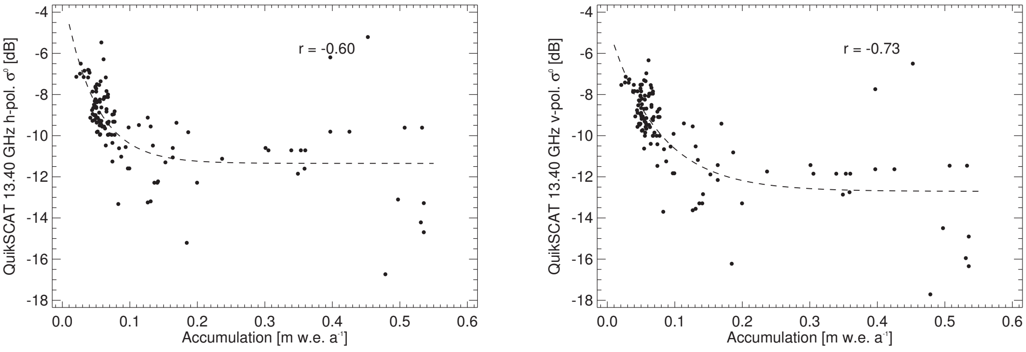

(a) *H-polarized* σ^0 **(b)** *V-polarized* σ^0

Figure 6.3: *Correlation between ground truth and 13.40 GHz QuikScat data.*

QuikScat annual mean backscatter values are plotted versus accumulation rates in Figure 6.3. From a theoretical viewpoint, it is to be expected that a high accumulation rate corresponds to a low backscatter value due to smaller scatterer sizes. This type of correlation between A and σ^0 can be found in the data, but it is not very pronounced. A significant sensitivity between A and σ^0 is visible only for $A < 0.1$ m w.e./a. There is no correlation between amplitude and accumulation rate (Figure 6.4) in the QuikScat data, hence the amplitudes are not suitable to infer accumulation rates. This is in agreement with other observations (Rott et al., 1993). Only little seasonal variability of σ^0 in the dry snow zone is to be expected because backscatter properties are mainly influenced by the size of the scatterers. Hence, the seasonal variation of σ^0 is only indirectly temperature-dependent.

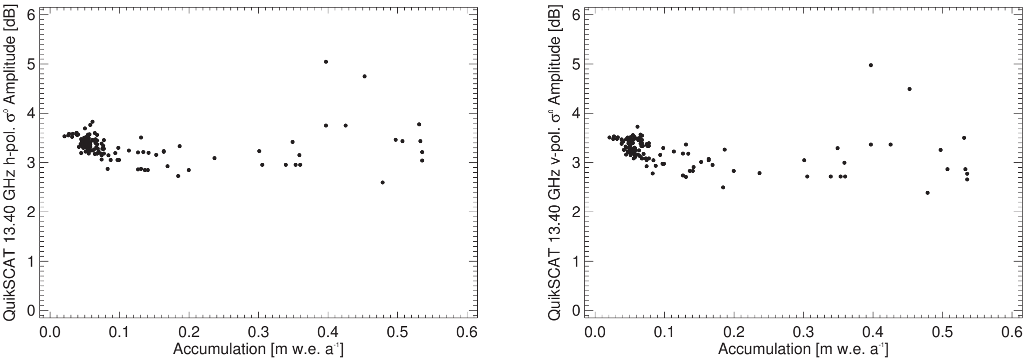

(a) *H-polarized* σ^0 *amplitude* **(b)** *V-polarized* σ^0 *amplitude*

Figure 6.4: *Correlation between ground truth and 13.40 GHz QuikScat amplitude*

The day-to-day variability of the σ^0 measurements in the QuikSCAT data is on the order of the amplitude of the seasonal signal. Due to the large variations, QuikScat amplitudes are not suitable to derive accumulation rates, which is in accordance with findings by Flach et al. (2005). As a consequence, QuikSCAT data are not included in the following considerations.

SSM/I data at 19.35 GHz

Figure 6.5 shows the correlation between mean annual SSM/I brightness temperatures at 19.35 GHz and measured accumulation rates. Because larger snow grains lower the emissivity of the snow pack, brightness temperatures measured in areas with low accumulation are lower than brightness temperatures measured in high-accumulation areas. The brightness temperatures' sensitivity to accumulation rates is variable. There is a "saturation effect" with respect to measured accumulation rates for A higher than approximately 0.2 m w.e./a, decreasing the capability to resolve accumulation rates from absolute brightness temperatures beyond that value. This effect is possibly due to the sensitivity of microwave radiation to grain size in combination with the accumulation rate dependency of the grain radii in near-surface layers.

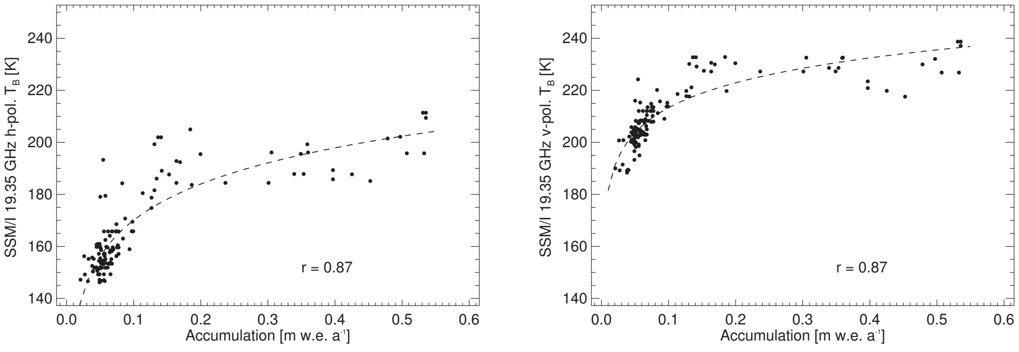

(a) *H-polarized* T_B **(b)** *V-polarized* T_B

Figure 6.5: *Correlation between ground truth and* T_B *(19.35 GHz)*

The annual amplitude of brightness temperatures at 19.35 GHz displays a significant amount of noise at horizontal polarization and some sensitivity to the accumulation rate at vertical polarization for $A < 0.15$ m w.e./a (Figure 6.6). As described earlier in Section 3, the brightness temperature at both polarizations is correlated to the physical temperature of the firn. At horizontal polarization, the amount of stratification additionally influences the T_B signal. The stratification of polar firn is not directly linked to the accumulation rate, and rather depends on single precipitation or drift events (Gow, 1965; Alley

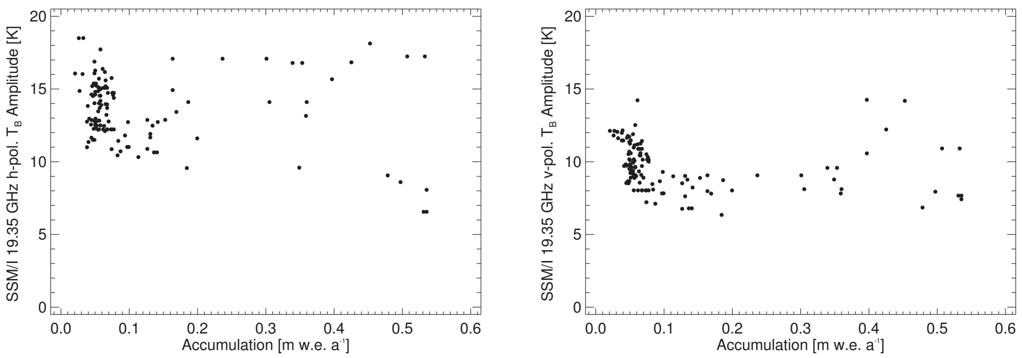

(a) *H-polarized T_B amplitude* **(b)** *V-polarized T_B amplitude*

Figure 6.6: *Correlation between ground truth and amplitude (19.35 GHz)*

et al., 1982; Palais et al., 1982). This is difficult to include in the microstructure model, whereas the parametrization of a temperature profile is relatively simple.

SSM/I data at 22.23 GHz

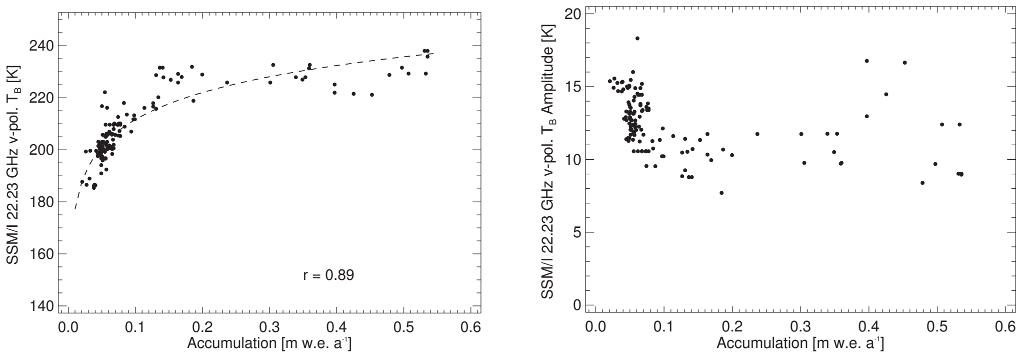

(a) *V-polarized T_B* **(b)** *V-polarized T_B amplitude*

Figure 6.7: *Correlation between ground truth and data (22.23 GHz)*

The 22.23 GHz data are available at vertical polarization only. They show a distinct correlation between T_B and A in Figure 6.7a, and a sensitivity of the brightness temperature amplitude to the accumulation rate at $A < 0.15$ m w.e./a. For higher accumulation rates, the relation again saturates.

SSM/I data at 37.00 GHz

At a frequency of 37.00 GHz, the correlation between absolute brightness temperatures and accumulation rates is relatively high. The saturation effect starts off again at about 0.2 m w.e./a for both polarizations (Figure 6.8) as well as the amplitudes (Figure 6.9). This value seems to be independent of sensor frequency, and is thus not connected to signal penetration depth into the firn.

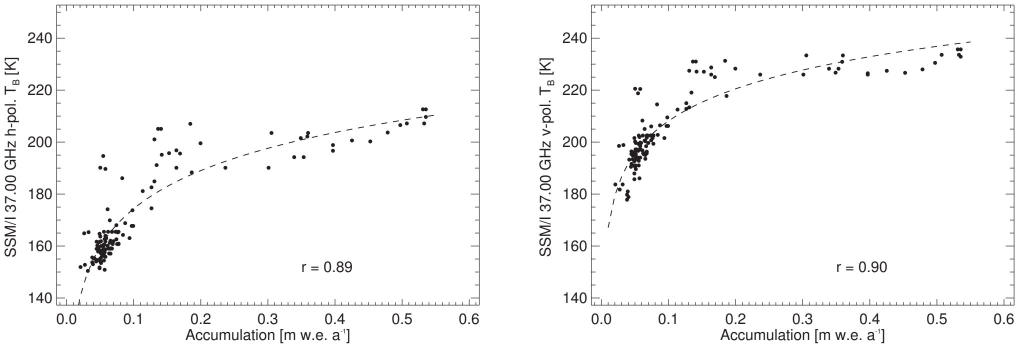

(a) *H-polarized T_B* **(b)** *V-polarized T_B*

Figure 6.8: *Correlation between ground truth and T_B (37.00 GHz)*

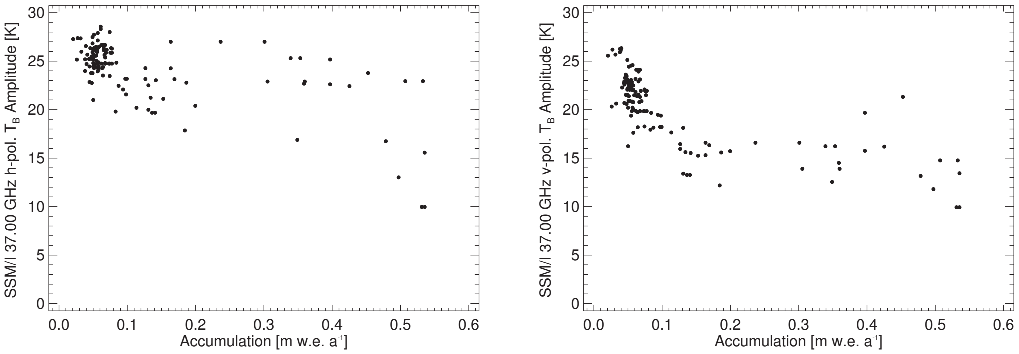

(a) *H-polarized T_B amplitude* **(b)** *V-polarized T_B amplitude*

Figure 6.9: *Correlation between ground truth and amplitude (37.00 GHz)*

At vertical polarization, the amplitudes also show a pronounced correlation with the accumulation rate for $A < 0.15\,\mathrm{m\,w.e./a}$ (Figure 6.9b). The amplitudes at horizontal polarization are very noisy (Figure 6.9a) and not well suited to invert accumulation rates.

SSM/I data at 85.50 GHz

The absolute T_B at 85.50 GHz shown in Figure 6.10 has a low correlation to accumulation rates, and the highest level of noise of all the brightness temperature datasets examined. Despite a high amplitude range of 20 K, there is no sufficient correlation between amplitude and accumulation rate. This can be explained by looking at the atmospheric transmission windows for electromagnetic radiation in the microwave frequency region and noting a sensitivity to atmospheric water vapor at this frequency (Petty, 2006). It can be concluded from this investigation that data recorded at 85.50 GHz are not well suited to determine accumulation rates without correcting for this effect.

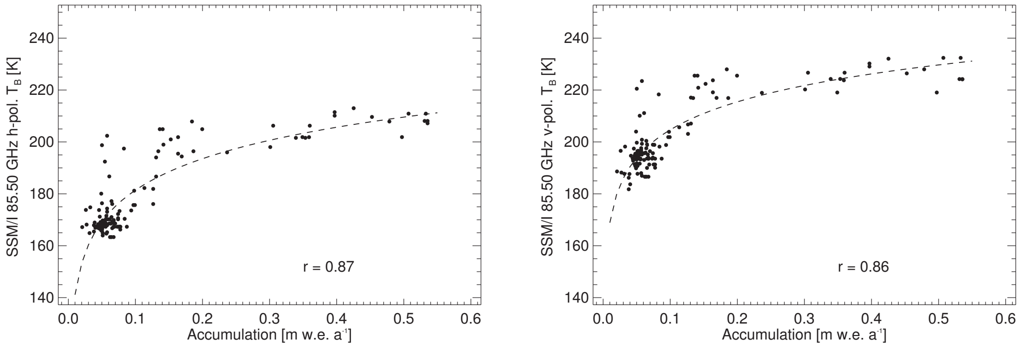

(a) *H-polarized T_B* **(b)** *V-polarized T_B*

Figure 6.10: *Correlation between ground truth and T_B (85.50 GHz)*

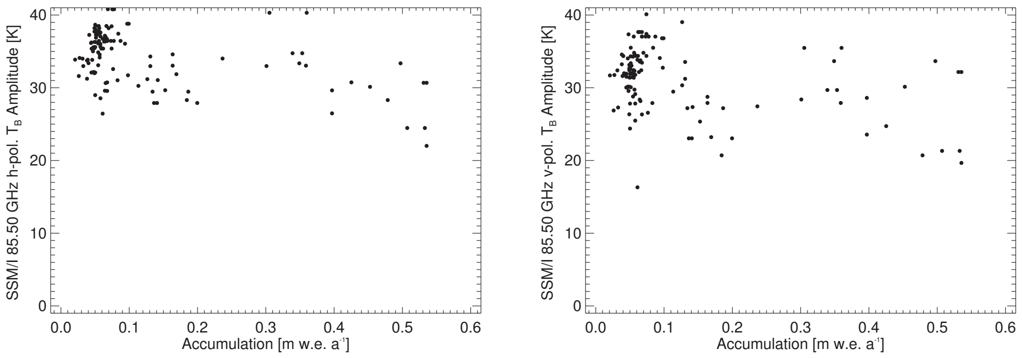

(a) *H-polarized T_B amplitude* **(b)** *V-polarized T_B amplitude*

Figure 6.11: *Correlation between ground truth and amplitude (85.50 GHz)*

Summarizing above observations, passive microwave data at frequencies between 19 and 37 GHz seem most suited to derive accumulation rates, with possible caveats regarding the sensitivity at A-values larger than 0.15–0.2 m w.e./a. Data recorded at 85 GHz are influenced by atmospheric effects, and while this may be possible to correct, the penetration depth into polar firn is on the order of centimeters only, hence the signal is very strongly influenced by grain size variability at the surface. This effect will be very difficult to model. For all cases, the vertically polarized datasets promise more accurate results due to lower noise levels. For this reason, the horizontal polarization will not be considered in the following part.

6.1.2 SAR data

The relationship between Envisat ASAR backscatter normalized to an incidence angle of 35° and accumulation rate measurements is also examined in

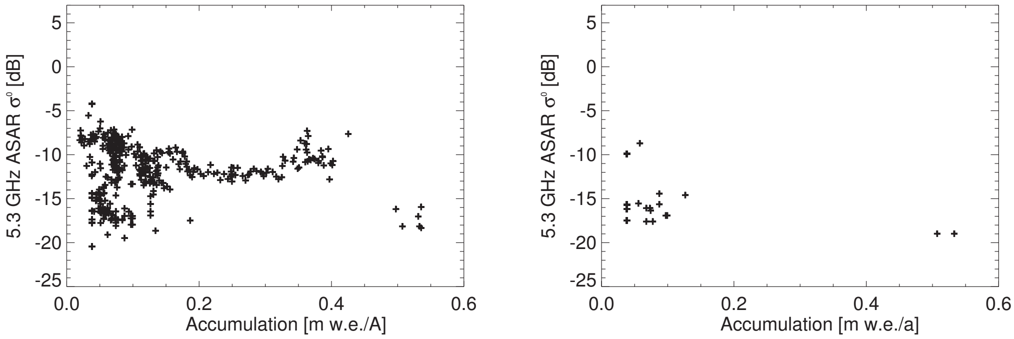

(a) *H-polarized* σ^0 **(b)** *V-polarized* σ^0

Figure 6.12: *Correlation between ground truth and Envisat ASAR backscatter at 5.3 GHz*

this work. Results are shown in Figure 6.12 for both polarizations. Since SAR images have a much higher spatial resolution than the datasets discussed previously, the measurements from the Kottas traverse are included at this point. There are relatively few SAR images available at vertical polarization, hence the degree of correlation between those two sets of data remains inconclusive. There is a sufficient amount of data available from horizontally polarized ASAR scenes, but the interpretation is difficult.

While the QuikScat and SSM/I datasets are available for an entire annual cycle, ASAR images are single radar scenes. For this reason there is no seasonal amplitude available for SAR data. Additionally, there is a strong relation between σ^0 and temperature, which will be examined in the following section.

6.2 Validation of the radiative transfer model

The radiative transfer model can be validated by a comparison to measurements. Many studies of microwave interaction with snow at different frequencies exist, but very few of the results are applicable to polar dry snow conditions. A study of microwave signatures of Antarctic firn was conducted by Rott et al. (1993). They examined the angular dependency of microwave signatures at C- and X-band and measured brightness temperatures and backscatter coefficients at frequencies of 5.25 and 10.3 GHz at three sites in Dronning Maud Land, and the measurements from their publication are used to validate the results from the model developed in this work. Accumulation rates and mean annual temperatures of the three measurement sites are known, and those values are used as input for the microstructure model (Section 3.2). Brightness temperatures were calculated from the layered radiative transfer model introduced in Section

5.1.2. Figure 6.13 shows the angular dependency of brightness temperatures measured at C- and X-band at the Base Camp site and the respective model results. Base Camp is located at 74 ° 45 " S, 12 ° 24 " W, at an elevation of 1200 m above sea level; it has an accumulation rate of 0.38 m w.e./a and a mean annual temperature of -25 °C.

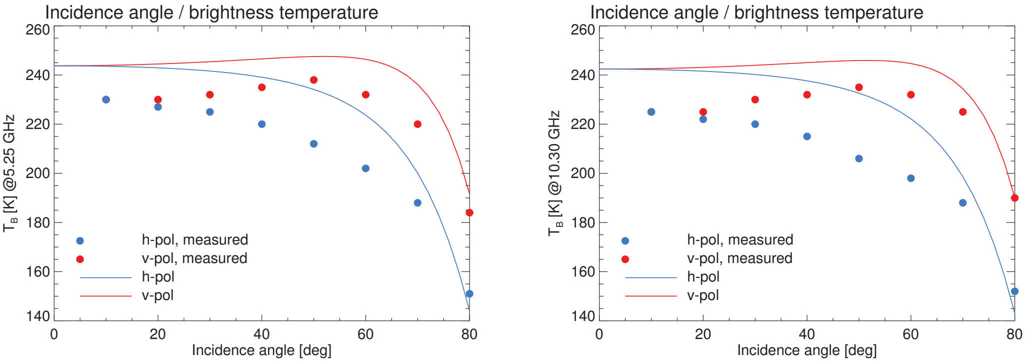

(a) *C-band* **(b)** *X-band*

Figure 6.13: *Modeled absolute T_B values (lines) and measurements from Rott et al. (1993) (dots)*

It is clearly visible that the model results overestimate the measured values. That is also the case for the other two sites examined by Rott et al. (1993), which are not shown here. Due to the sensitivity to firn structure, the offset between model results and measurements is not constant and cannot be easily removed by empirical correction. Another fact to notice is a lower polarization difference in the model result, compared to the measurements. Both effects can be caused by not including scattering at internal boundaries in the radiative transfer model (West, 1994; Li et al., 2006; Rott et al., 1993). Including dense medium effects, on the other hand, would increase modeled brightness temperatures (Tedesco and Kim, 2006; Tsang, 1992). The model results are in accordance with findings by Flach et al. (2005).

West (1994) examined the same locations and showed that, due to firn layer thicknesses on wavelength order, coherent scattering effects become significant. He used a fully coherent field solution to model brightness temperatures, and found that the absolute T_B assumed more realistic values than those calculated from a non-scattering model, albeit not in all cases examined.

A microwave emission model for layered snow packs (MEMLS) (Wiesmann and Mätzler, 1999; Mätzler and Wiesmann, 1999) includes multiple and coherent scattering and is based on the improved Born approximation (Mätzler, 1998). Results from this model for the Base Camp site are shown in Figure 6.14. The scatterer profile used as input to MEMLS is generated from the microstructure model from Section 3.2 and is identical to the one used to generate Figure 6.13.

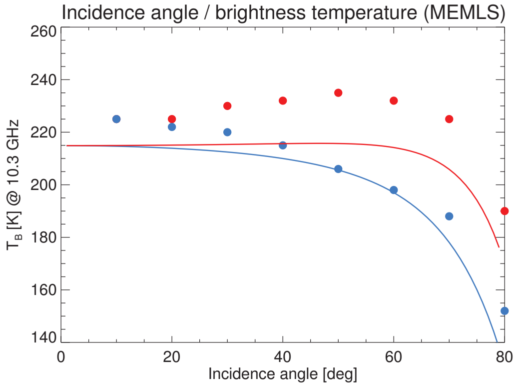

Figure 6.14: *Modeled absolute T_B values at X-band from MEMLS (lines) and measurements from Rott et al. (1993) (dots)*

Despite being much more complex than the simple model used in this work, MEMLS also underestimates the absolute brightness temperature values. So does the model of West (1994), but at this specific location only. While it might seem slightly arbitrary to evaluate results from different emission models based on one single location and one single frequency, this gives a hint to the difficulties of creating an accurate model of microwave interaction with polar firn*.

Therefore, the focus here will be on the relationship between the amplitude of the annual brightness temperature cycle and the accumulation rate, using the frequency range between 19 and 37 GHz.

A comparison between measured and modeled amplitudes was carried out to determine the suitability of the model results for accumulation rate retrieval. Modeled amplitudes for all considered frequencies are calculated from a set of accumulation rates ranging from 0.01 to 0.6 m w.e./a and mean annual temperatures of -50 °C and -20 °C. The temperature values were chosen as a lower and an upper limit representing the temperature range of the field data. Mie scattering becomes significant at the considered frequencies, hence the model was run twice for each frequency, once including Mie scattering and once with the Rayleigh approximation.

Since there is an option in the microstructure model to include a density variability factor, described in Section 3.2.1, it was integrated in the model runs. Each of the following plots display model results calculated with a density variability of $\Delta\rho = 0.0$ and $\Delta\rho = 1.0$ to evaluate the impact of density variability.

---

*A more detailed comparison of microwave emission models was conducted by Tedesco and Kim (2006), with similarly inconclusive results.

6.2.1 Low-resolution data

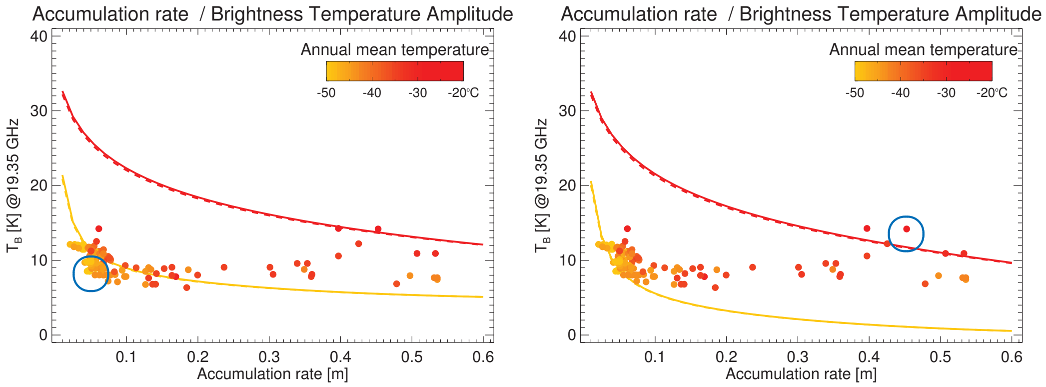

(a) *Rayleigh solution* **(b)** *Mie solution*

Figure 6.15: *Modeled T_B amplitudes; solid lines are modeled with a density variability of $\Delta\rho = 0.0$, dashed lines are modeled with $\Delta\rho = 1.0$. Dots show amplitudes from SSM/I data for 19.35 GHz at vertical polarization. Model results are color-coded on the same scale as the measurements*

Amplitudes for a frequency of 19.35 GHz are shown in Figure 6.15. While the Rayleigh solution compares well with the field data for high temperatures and high accumulation rates, it overestimates amplitudes at low accumulation rates and low temperatures. The amplitudes modeled using Mie scattering and a mean annual temperature of -50 °C fit the observed values more accurately. On the other hand, the Mie solution at a mean annual temperature of -20 °C tends to underestimate amplitudes at higher accumulation rates. Due to the nonlinear dependency of the amplitude of the seasonal brightness temperature signal and the accumulation rate, the impact of a deviation of the model result from the observed values is much more severe at low accumulation rates.
The Rayleigh solution in the area circled in blue in Figure 6.15a results in a modeled accumulation rate that is roughly 2.5 × the observed value. The deviations between the Mie solution and observations marked in Figure 6.15b lead to an accumulation rate that is approximately 0.7 × the observed value. It can be noted that considering Mie scattering in the model significantly improves the accuracy of the accumulation retrieval algorithm. Another observation is that amplitudes become very small at high accumulation rates and low temperatures for the Mie solution. This combination does not occur in reality (see Figure 6.20).

The comparison of modeled amplitudes and data was also carried out for a frequency of 22.23 GHz (Figure 6.16). Similar to the 19.35 GHz results, modeled

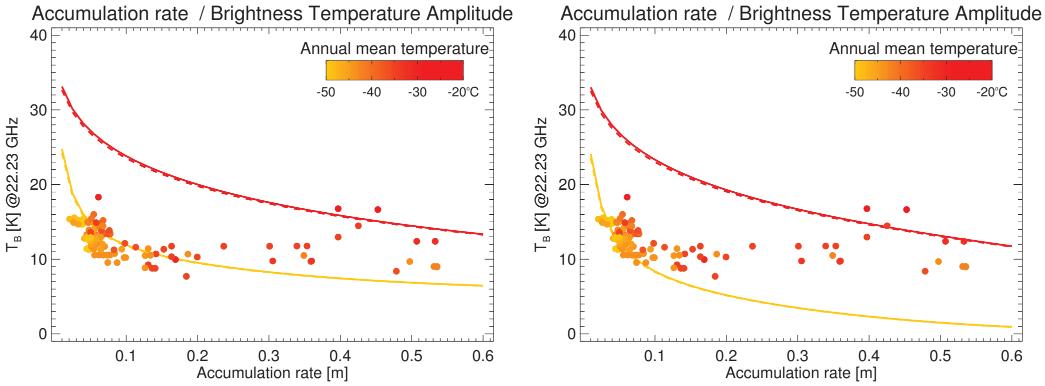

(a) *Rayleigh solution* **(b)** *Mie solution*

Figure 6.16: *Modeled T_B amplitudes; solid lines are modeled with a density variability of $\Delta\rho = 0.0$, dashed lines are modeled with $\Delta\rho = 1.0$. Dots show amplitudes from SSM/I data for 22.23 GHz at vertical polarization. Model results are color-coded on the same scale as the measurements*

amplitudes are too high at low accumulation rates and low temperatures for the Rayleigh result, but fit better when Mie scattering is considered. There is almost no difference between amplitudes modeled using Mie or Rayleigh scattering for a mean annual temperature of -20 °C. A possible explanation for this effect has to consider the temperature dependency of the grain growth rate as well as the penetration depth and the particle size at which the Rayleigh approximation is no longer valid (the latter both depending on frequency) and still needs to be evaluated.

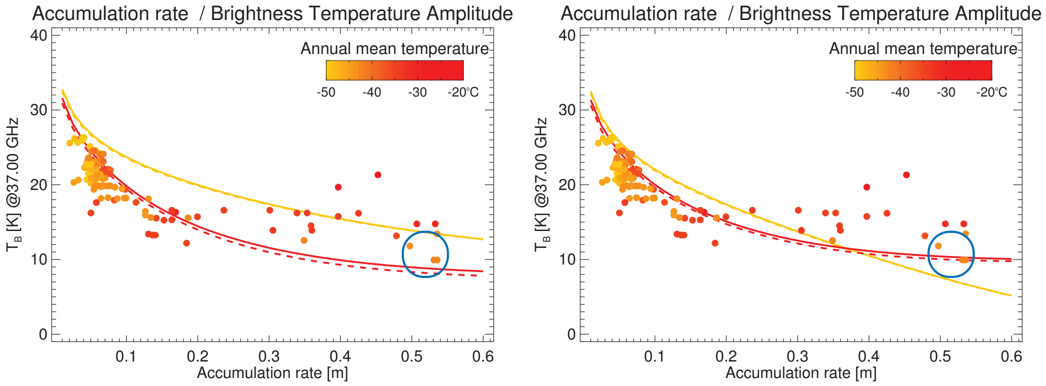

(a) *Rayleigh solution* **(b)** *Mie solution*

Figure 6.17: *Modeled T_B amplitudes; solid lines are modeled with a density variability of $\Delta\rho = 0.0$, dashed lines are modeled with $\Delta\rho = 1.0$. Dots show amplitudes from SSM/I data for 37.00 GHz at vertical polarization. Model results are color-coded on the same scale as the measurements*

The vertically polarized amplitudes modeled at 37.00 GHz are somewhat inconclusive at a first glance (Figure 6.17). It can be seen that modeled amplitudes using the Mie solution are larger than the measurements for $A < 0.2\,\mathrm{m\,w.e./a}$.

As a result, low accumulation rates will be systematically overestimated in the inversion. For $A > 0.35\,\mathrm{m\,w.e./a}$, the model calculates amplitudes that are too low, underestimating accumulation rates inverted from the model results. The Rayleigh solution overestimates amplitudes for $A < 0.2\,\mathrm{m\,w.e./a}$ and underestimates amplitudes for $A > 0.2\,\mathrm{m\,w.e./a}$ and high temperatures. From the theoretical considerations outlined in the description of the glacier zones in Section 3, it is expected that due to the larger sensitivity to stratification, the effect of $\Delta\rho$ on the model result is more pronounced at horizontal polarization. That is confirmed by the model results, which show no significant sensitivity of the amplitudes at vertical polarization, while at horizontal polarization, the inclusion of density variability lowers the modeled amplitudes. This effect is on the order of less than 1 K for all all examined frequencies, and is more pronounced at lower accumulation rates because the layering is more dense in that case. If only the vertical polarization is considered, the effect of stratification variability can safely be ignored.

6.2.2 SAR data

Figure 6.18 shows the model results for 5.3 GHz absolute backscatter values in comparison with σ^0 from Envisat ASAR images at horizontal polarization for a range of accumulation rates. The first thing to note is that the modeled absolute backscatter values are far too high, compared with the data. This might be attributed to neglecting dense medium effects in the model (West, 1990).

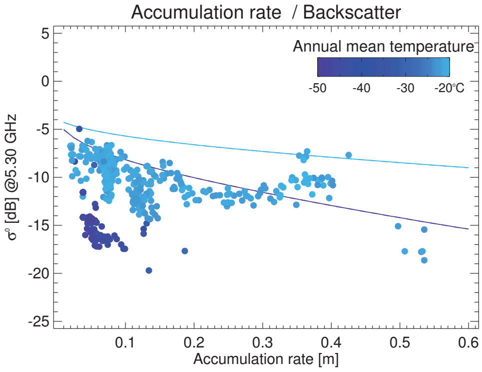

Figure 6.18: *Correlation between ground truth and Envisat ASAR σ^0 at 5.3 GHz (dots). The solid line is the model result at horizontal polarization. Model results are color-coded on the same scale as the measurements*

There is a significant correlation between temperature and backscatter, which is strongly underestimated by the model. For similar temperatures, there is a variability in the backscatter values of up to 7 dB, which introduces additional errors to the results from the inversion. The variability cannot be explained by radar speckle, as speckle is approximately one order of magnitude smaller. A large variability of backscatter intensities at constant accumulation rates was also noted by Drinkwater et al. (2001) for scatterometer data from different spaceborne sensors.

6.3 Inversion results

For the inversion procedure, lookup tables are generated by calculating T_B amplitudes or absolute backscatter σ^0 from the radiative transfer models introduced in Chapter 5, using firn microstructure profiles calculated from the parameterization developed in Chapter 3 as input.

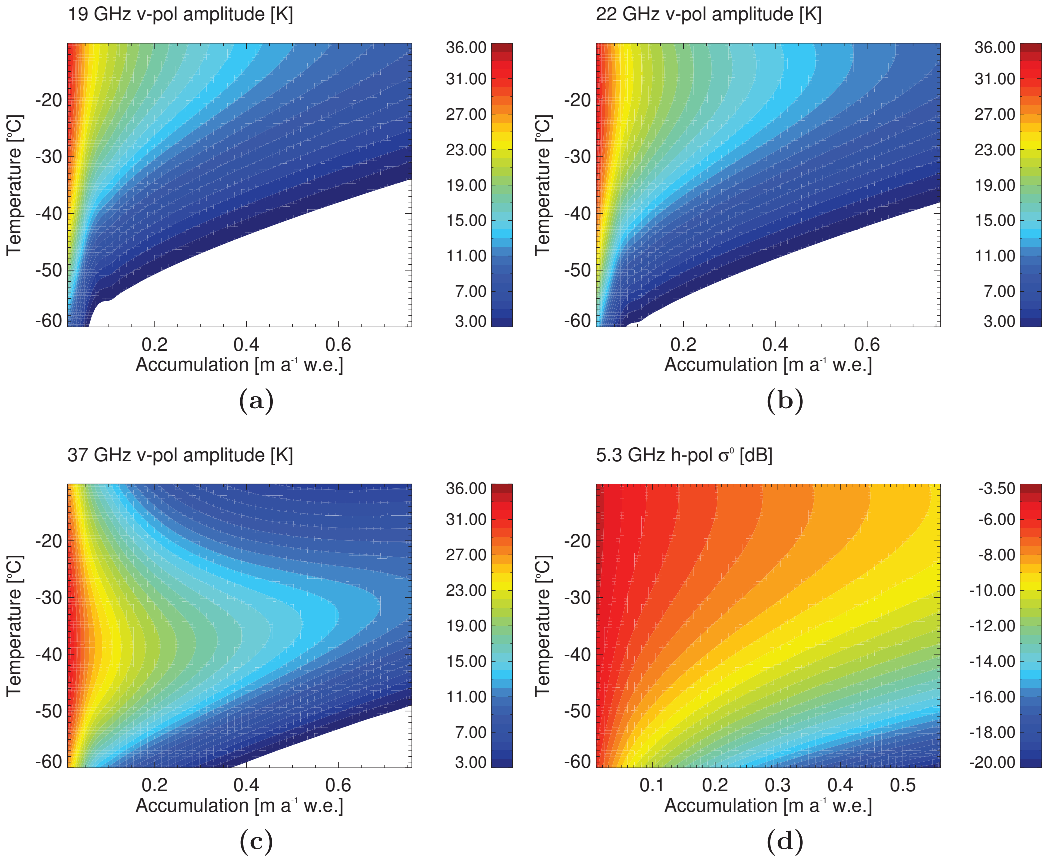

(a) (b) (c) (d)

Figure 6.19: *Lookup tables, Mie solution*

All tables are generated to cover temperature ranges between -20 °C and -60 °C using a step size of 0.1 °C. Accumulation rates range from 0.01 – 0.8 m w.e./a, with a step size of 0.01 m w.e./a. For each combination on input parameters, a firn profile is calculated. This is then used to determine the brightness temperatures for an entire annual cycle, from which the T_B amplitudes are subsequently derived. Absolute σ^0 values are also calculated for the firn profile obtained from each combination of input parameters. Resulting amplitudes and σ^0 are then stored in lookup tables.

Passive microwave amplitudes of seasonal variations are calculated at frequencies from 19 GHz to 37 GHz (Figures 6.19a to 6.19c). Figure 6.19d shows the lookup table for 5.3 GHz absolute backscatter. Following the observations in the previous section, the Mie solution was used to generate the tables for the passive sensors' frequency range. This was not necessary for calculating the backscatter. The results from the lookup table generation are shown in Figure 6.19.

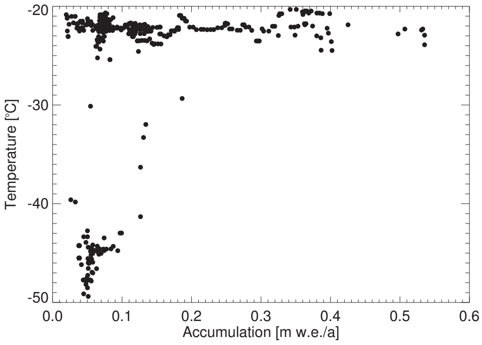

Figure 6.20: *Correlation of accumulation rates to temperature*

There are some data gaps in the lookup tables for the brightness temperature amplitudes, notably at a combination of high accumulation rates and low temperatures. In those regions the model fails, mostly due to the fact that the scatterer sizes assume unrealistic values. On the other hand, the combination of high accumulation and low temperatures is never found in reality, because there is not enough humidity left in the air to cause precipitation (Pruppacher and Klett, 1997). Figure 6.20 confirms this, using the entire set of in-situ accumulation rates and MODIS temperatures.

6.4 Derived accumulation maps

For the recent work, accumulation maps are generated by looking up temperature values from an external dataset, finding the corresponding amplitude or backscatter value in the lookup table and then assigning the accumulation rate accordingly. For the low-resolution passive microwave datasets in Antarctica, the spatially interpolated THERMAP (Section 2.3.1) is used. Those values have a rather coarse resolution and are inaccurate in regions of sparse spatial sampling. Temperatures used for the high-resolution SAR images are obtained from MODIS data (Section 2.3.2). The accumulation maps derived from SSM/I data for Greenland were also generated using MODIS temperatures that were sampled down to SSM/I resolution.

6.4.1 Antarctica

Low-reslution data

Figure 6.21 shows accumulation maps derived from 19.35 GHz SSM/I amplitudes. Figure 6.21a was generated from a lookup table calculated using Rayleigh scattering. For the table from which Figure 6.21b originates, Mie scattering was used to calculate the amplitude values. There is a large difference in the amount of accumulation between those maps. While the spatial accumulation patterns agree, a comparison with field data shows that the amount of accumulation is significantly overestimated by the Rayleigh solution. This effect is most pronounced in East Antarctica. Scatterplots of the correlation between accumulation rates inverted from 19.35 GHz SSM/I amplitudes and ground truth values are shown in Figure 6.22a for the Rayleigh solution and in Figure 6.22b for the Mie solution. From the model validation (Figure 6.15), it is to be expected that the inversion results are higher than the measurements. The correlation between observed (A_{obs}) and modeled accumulation rates (A_{mod}) is almost linear in Figure 6.22b, this is not the case for Figure 6.22a. Inversion results from 22.23 GHz (Figure 6.23a) are similar to results from the 19.35 GHz dataset, both in spatial distribution and magnitude. This

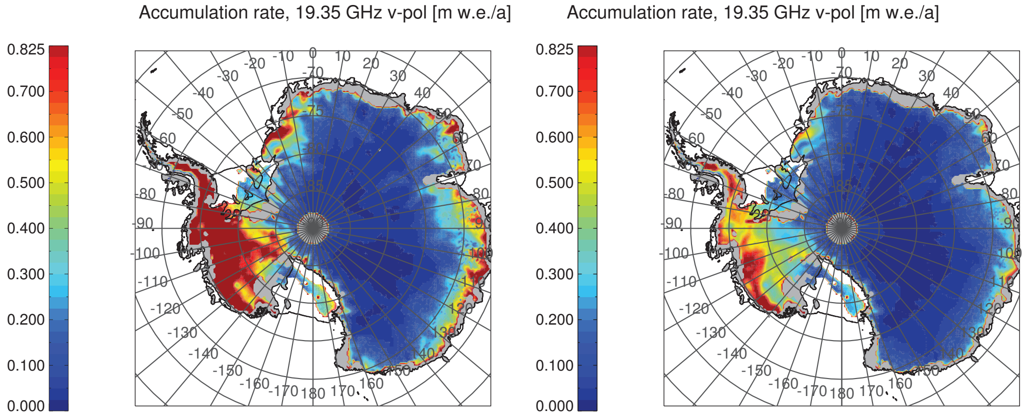

(a) *19.35 GHz, Rayleigh approximation* **(b)** *19.35 GHz, Mie solution*

Figure 6.21: *Accumulation maps from 19.35 GHz v-polarized SSM/I data*

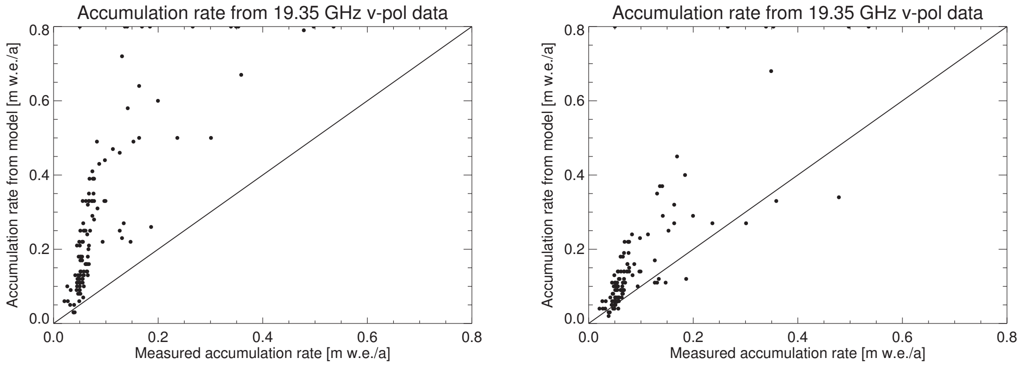

(a) *19.35 GHz v-polarized SSM/I data, Rayleigh approximation*

(b) *19.35 GHz v-polarized SSM/I data, Mie solution*

Figure 6.22: *Measured vs. modeled accumulation rates, 19.35 GHz*

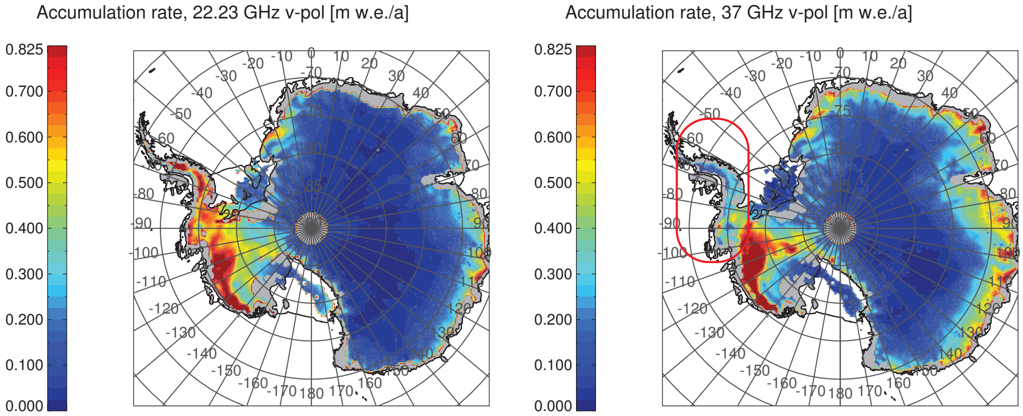

(a) *22.23 GHz, Mie solution*

(b) *37.00 GHz, Mie solution*

Figure 6.23: *Accumulation maps from 22.23 and 37.00 GHz v-polarized SSM/I data*

is not the case for accumulation rates determined from 37.00 GHz data (Figure 6.23b). Here, accumulation rates in Antarctica's coastal areas are significantly overestimated. The values derived for the Antarctic peninsula, circled in red in Figure 6.23b, are heavily underestimated. A scatterplot of A_{obs} versus A_{mod} for 22.23 GHz (Figure 6.24a) is very similar to the one at 19.35 GHz (Figure 6.22b), showing an almost linear relationship between inverted and observed accumulation rates. The slope of a fitted linear function is larger than the one at 19.35 GHz, indicating that low accumulation rates tend to be overestimated by the 22.23 GHz solution.

At 37 GHz, the relationship between A_{obs} and A_{mod} is no longer linear (Figure 6.24b). The model does not fully account for the high sensitivity of the annual brightness temperature amplitudes to accumulation rates of less than 0.2 m w.e./a. at this frequency.

Shown in Figures 6.25 and 6.26 are differences between the accumulation maps

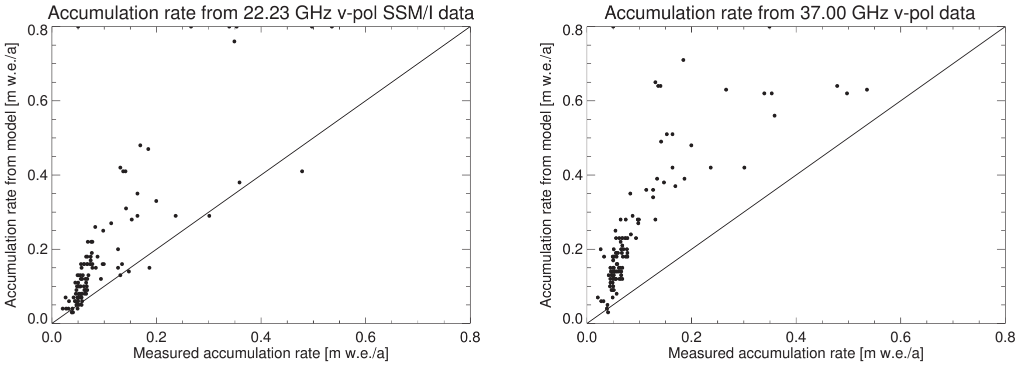

(a) *22.23 GHz v-polarized SSM/I data, Mie solution* **(b)** *37.00 GHz v-polarized SSM/I data, Mie solution*

Figure 6.24: *Measured vs. modeled accumulation rates, 22.23 and 37.00 GHz*

derived in this work and results published by Monaghan et al. (2006) (Figures 6.25b and 6.26b) and by Arthern et al. (2006) (Figures 6.25a and 6.26a). Both datasets are based on different methods: the accumulation map by Arthern et al. was generated by combining passive microwave-derived polarization ratios with field data, using geostatistical techniques. The accuracy of the dataset is given by the authors of this study to be < 10%, with larger errors at the ice sheet margins and more accurate results on the continent's interior. The nominal resolution of this accumulation map is limited by the spatial sampling of the field data to approximately 100 km. The authors also note that there are correlations between different accumulation maps if the same sets of ground truth are used.

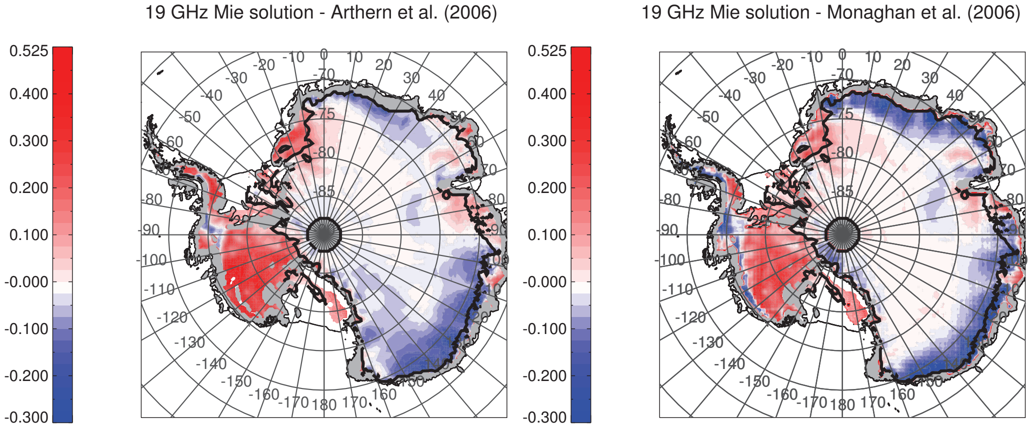

(a) *Own solution - Arthern et al. (2006)* **(b)** *Own solution - Monaghan et al. (2006)*

Figure 6.25: *Difference maps at 19.35 GHz. Marked in black is the 0.2 m w.e./a isoline from the 19 GHz Mie solution*

The dataset published by Monaghan et al. was generated using a regional climate model (Polar MM5), with the boundary conditions defined by different sets of climate reanalysis data. The accuracy of accumulation data from climate models is restricted by the quality of the climate data used to set its inital and boundary conditions. The resulting accumulation patterns can vary significantly, depending on the choice of boundary conditions. The autors of this study found deviations from other datasets of up to 33 % in some regions, compared to an accumulation map derived from field data by Vaughan et al. (1999). Another study by Van de Berg et al. (2005), which also uses a regional climate model to estimate A, finds accumulation values that are systematically larger than results from Arthern et al. (2006) and Monaghan et al. (2006). Neither approach included a radiative transfer model, hence the datasets are used for an additional independent validation of the results of this study.

As both the 19 GHz and the 22 GHz channel are used to derive accumulation maps, both are included in the comparison. It can be seen that accumulation rates retrieved in this work are underestimated in the coastal regions of East Antarctica in comparison to the maps referenced above. At the same time, accumulation rates inverted using the model introduced here are significantly higher than the reference maps on the Antarctic peninsula.

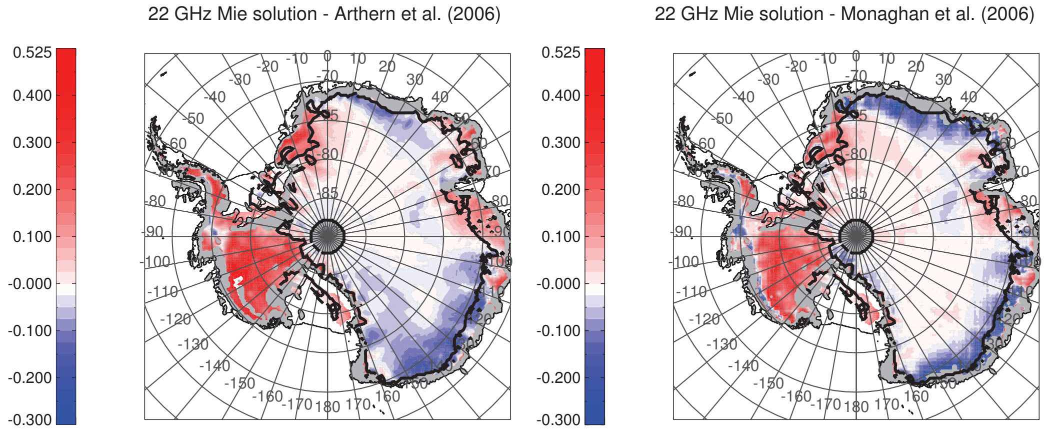

(a) *Own solution - Arthern et al. (2006)* **(b)** *Own solution - Monaghan et al. (2006)*

Figure 6.26: *Difference maps at 22.20 GHz. Marked in black is the 0.2 m w.e./a isoline from the 22 GHz Mie solution*

As a conclusion of the part concerning low-resolution passive microwave data, it can be observed that at higher accumulation rates the model results become less reliable. For higher accumulation rates, the correlation shows significantly more noise than for lower values. The SSM/I instrument has a low spatial resolution, with pixel sizes on the order of 20 km. The highest spatial heterogenity of accumulation patterns can be found in coastal areas, where the accumulation rates are high compared to the plateau region. It is possible that the noise at higher accumulation rates originates from this high heterogenity. After all, the A_{obs} are point data and it is always a source of error to compare those with large-scale spatially averaged values. Additional uncertainty is introduced by the lower sensitivity of brightness temperatures to accumulation rates at larger A.

The accuracy of the inversion results also degrades with increasing sensor frequency. It has to be considered that the penetration depths d of microwave radiation in dry snow at 37 GHz is between 3–30 cm (Table 4.1), and thus below the layer thickness used in the model (approximately 1–70 cm, depending on input accumulation rates, see also Section 3.2.1).

For regions of $A < 0.2$ meter w.e./a, the compared datasets (field data as well as accumulation maps from external sources) agree well, and the approach chosen in this work is found suitable to invert accumulation rates from passive microwave data within the limits discussed above.

SAR data

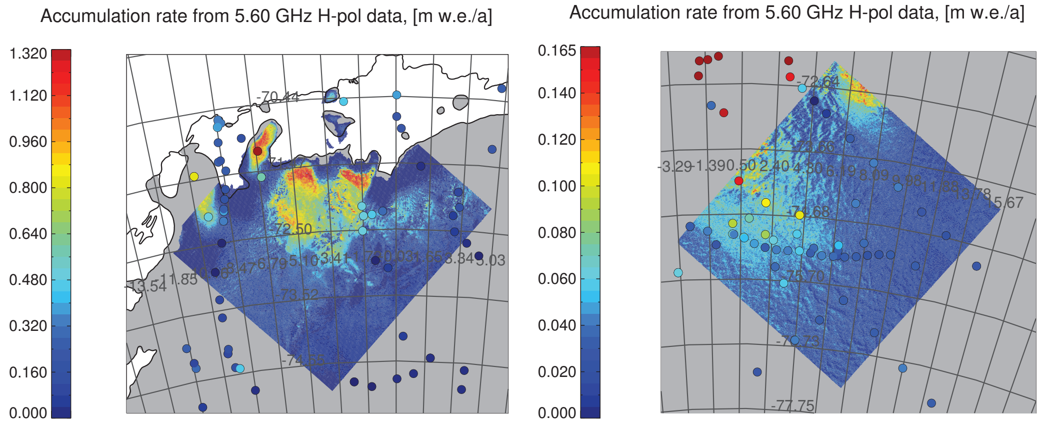

(a) *Frame #5652* **(b)** *Frame #5580*

Figure 6.27: *Accumulation maps from 5.3 GHz h-polarized ASAR data. Please note the different scales used for Figure 6.27a and 6.27b*

Figure 6.27 shows accumulation maps generated using the lookup table in Figure 6.19d and two consecutive Envisat ASAR Wide Swath scenes recorded over Dronning Maud Land. To assess the accuracy of the resulting accumulation map, SAR speckle is estimated by evaluating the backscatter variability from a homogeneous region of 10 × 10 pixel. The corresponding standard deviation is on the order of 0.5 dB. For an observed accumulation rate of 0.2 m w.e./a, the effect of speckle on accumulation rates inverted from the lookup table in Figure 6.19d depends on temperature. For a temperature of -50 °C, the in-

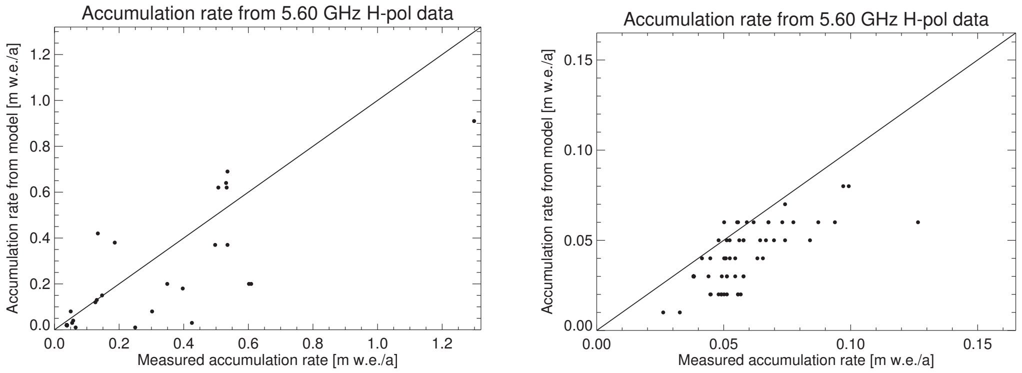

(a) *Frame #5652* **(b)** *Frame #5580*

Figure 6.28: *Measured vs. modeled accumulation rates, 5.3 GHz. The point measurements are color-coded on the same scale as the accumulation map. Please note the different scales used for Figure 6.28a and 6.28b*

verted accumulation rates can assume values between 0.17 and 0.23 m w.e/a if σ^0 varies by 0.5 dB. This range is much larger at -20 °C. In this case, the inverted values can be between 0.13 and 0.27 m w.e/a. The speckle uncertainty can account for much of the deviations in Figure 6.28, and it is obvious that the results are more accurate in low-accumulation, low-temperature regions (Figures 6.27a and 6.28b) than in high-accumulation areas (Figures 6.27b and 6.28a).

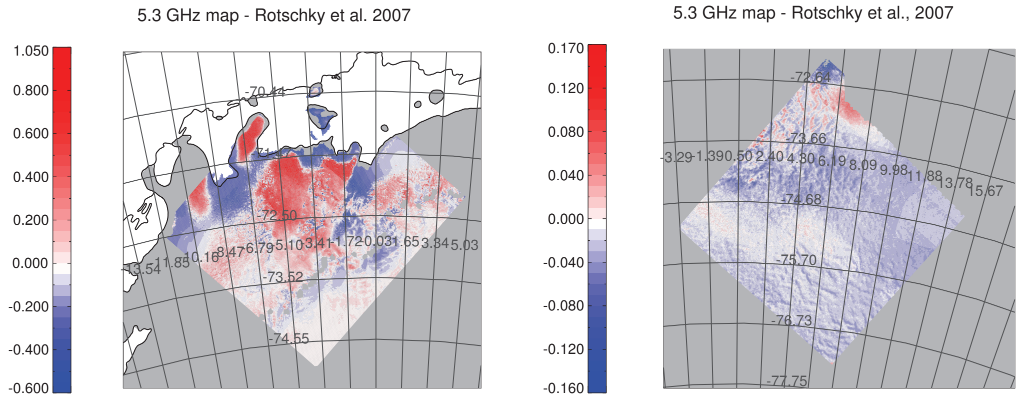

(a) *Frame #5652* **(b)** *Frame #5580*

Figure 6.29: *Difference maps at 5.3 GHz. Please note the different scales used for Figures 6.29a and 6.29b*

The accumulation map published by Rotschky et al. (2007) was used to externally evaluate the inversion results. This dataset was generated by using Envisat ASAR images to spatially interpolate field data. It is based on empirical relationships between snow classes derived from satellite data and ground truth. A difference map was calculated for the intersecting areas between the Rotschky et al. map and the dataset derived in this work (Figure 6.29). There are large deviations in high-accumulation areas (Figure 6.29a). The accumulation map derived from Envisat ASAR Wide Swath data (Figure 6.27b) has a resolution of 150 m, and the resolution of the dataset from Rotschky et al. is 5 km. The differences between the two datasets in the low-accumulation area in Figure 6.29b can be mostly attributed to different spatial sampling.

6.4.2 Greenland

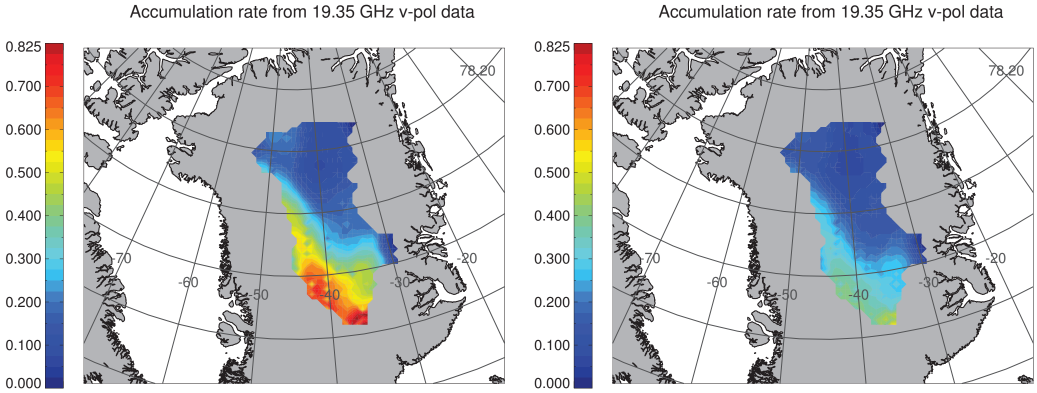

(a) *19.35 GHz, Rayleigh solution* **(b)** *19.35 GHz, Mie solution*

Figure 6.30: *Accumulation of the Greenland dry snow zone from v-pol SSM/I data*

An accumulation map of the Greenland dry snow zone was also generated using the lookup tables for 19.35 GHz vertically polarized SSM/I amplitudes. Shown in Figure 6.30a is the map generated using Rayleigh scattering. The derived accumulation rates are much higher than observed values. Figure 6.30b shows the accumulation map derived from the Mie solution, it is in accordance with published results from other sources, e.g. (Cogley, 2004; Burgess et al., 2010) in both spatial distribution and absolute amount of accumulation.

7

Discussion and outlook

There have been a number of attempts to retrieve snow accumulation rates A from both passive and active microwave remote sensing data. Using the Kottas traverse data, Welker (2007) used a multiple regression approach to derive accumulation rates from SSM/I brightness temperatures. Rotschky et al. (2006) developed a classification of snow properties for Antarctica based on the same set of ground truth in combination with scatterometer data, but no direct quantification of A is possible using this method. A different approach by Rotschky et al. (2006) derives different empirical relations between ASAR backscatter and accumulation rates based on the derived snow classes. Because this relies on a locally restricted set of field data, it is valid for parts of Dronning Maud Land only.

Following the approaches developed by Munk et al. (2003) and Flach et al. (2005), a quantification of A is possible. Both approaches were validated with field data from the dry snow zone of Greenland, and Munk et al. (2003) required some empirical correction terms to obtain realistic results. For Antarctica, both models failed due to an unrealistic microstructure parametrization for Antarctic climate conditions. For this reason, an improved firn microstructure model valid for the upper meters of the firn column is developed in this work. It allows a wider range of environmental conditions and accounts for the rapid grain growth caused by the seasonal temperature propagation into the firn.

All simple radiative transfer models used to invert snow accumulation, e.g. by Flach et al. (2005); Munk et al. (2003); Drinkwater et al. (2001) or Forster et al. (1999), employ the Rayleigh approximation to determine extinction properties of the firn. Results from more complex models of firn-microwave interaction were compared with measurements at single sites only (e.g. (Surdyk and Fily, 1995; West et al., 1996; Chuah et al., 1997; Jiang et al., 2007)). Since the assumption of Rayleigh scattering is no longer valid at the frequency range used by the SSM/I sensor, Mie scattering is integrated into a simple radiative transfer model for this study.

By inverting the accumulation rate from seasonal amplitudes rather than absolute brightness temperature values, the model approach developed here requires no additional empirically derived terms to account for inadequacies in the radiative transfer model.

Spatial patterns of accumulation are well represented by all model solutions, since they are inherent in the microwave data themselves. The absolute values of inverted accumulation rates depend on the scattering model used. The Rayleigh scattering solutions significantly overestimates A, but including Mie scattering leads to more reliable results. In general, a higher model sensitivity can be noted at low accumulation rates and low temperatures, and the uncertainty in accumulation rate retrieval increases at higher accumulation and higher temperature. This was demonstrated by analyzing the scatterplots between σ^0 / T_B and A, and the conclusion is that accumulation rate retrieval by means of the microwave remote sensing inversion introduced here works reliably for $A < 0.2\,\mathrm{m}$ w.e/a. For higher A, the uncertainty of the results increases, due to the loss of sensitivity of the microwave signal to the accumulation rate. For future work, it would be interesting to combine the method introduced here with an approach to retrieve accumulation rates from GRACE data (Sasgen et al., 2007), which is more sensitive to high A.

The accuracy of the results is also dependent on the frequency of the dataset used to invert A. For frequencies exceeding 22 GHz, the model tends to systematically overestimate accumulation. A source of the uncertainty can be the small signal penetration at those wavelengths. If only relatively few layers are included in the calculation, the radiative transfer model result would be more susceptible to inaccuracies in the firn microstructure implementation. For a larger penetration depth, inaccuracies in the mean firn profile will average out, as the signal is integrated over a larger number of layers. The most realistic results were obtained with SSM/I channels of 22 and 19 GHz. Because the correlation between accumulation and amplitude is less pronounced at horizontal polarization, only SSM/I datasets at vertical polarization were used for accumulation rate retrieval in this study.

SSM/I datasets have a rather coarse spatial resolution, resulting in an error due to large-scale spatial averaging of accumulation rates. Using data from sensors with a higher resolution (e.g. AMSR-E passive microwave) can lead to an improved estimate of accumulation rates on the polar ice sheets.

Future work should include a quantitative error assessment and an improved radiative transfer model including dense medium effects. It would be also very interesting to validate and improve the microstructure model using data from the snow grain size surveys conducted during the Trans-Antarctic Scientific Traverses Expeditions (ITASE) in 2007/08.

Symbols

Symbol	Unit	Value
a	m	ellipsoid semi-major axis
az	—	SAR azimuth direction
a_0, a_1, a_2	—	empirical fit parameters (density)
A	m w.e./a	accumulation rate
A_{mod}	m w.e./a	accumulation rate derived from model
A_{obs}	m w.e./a	accumulation rate from field data
$\hat{A}$	m^2	radar resolution cell area
b	m	semi-minor axis
$b_{i,j}$	—	empirical fit parameters (density)
B_r	—	bandwidth
c	m/s	speed of light
c_0, c_1, c_2	—	empirical fit parameters (grain size)
d	m	microwave penetration depth
d_0, d_1, d_2	—	empirical fit parameters (grain size)
DN^2	—	pixel intensity in SAR image
$\vec{e_i}$	—	orthonormal basis
E	$kJ \cdot mol^{-1}$	activation energy for grain-boundary self-diffusion
f	Hz	frequency
f_v	—	volume fraction of scatterers
$\boldsymbol{h}$	J	Planck's constant
h	m	height above reference ellipsoid
i, j	—	multi-purpose index variables
k	m^2/s	thermal diffusivity
$\vec{k}$	—	negative slant range direction
$\boldsymbol{k}_b$	J/K	Boltzmann's constant

Symbol	Unit	Value
k_0	m^{-1}	free-air wavenumber
K	mm^2/a	crystal growth rate
K_0	—	rate constant
$\hat{K}$	—	absolute radiometric calibration constant
l_{ra}	m	antenna footprint
l_i	m	snow layer thickness of the i-th layer
l_0	m	initial snow layer thickness
$\hat{l}$	m	correlation length
L_i	—	one-way loss factor of the i-th layer
$\vec{n}$	—	unit surface normal
$\lvert n\chi\rvert$	—	Mie parameter
n_{col}	—	number of image columns
n_{row}	—	number of image rows
N_v	—	number of scatterers in unit volume
$p = \{h\lvert v\}$	—	polarization: horizontal (h) or vertical (v)
P	—	polarization ratio
P_r	W	received power
P_t	W	transmitted power
r	mm	grain radius
r_0	mm	initial grain radius
r_{eff}	mm	effective grain size
rg	—	SAR range direction
$\hat{r}_0$	m	range distance to a target
$\hat{r}_{gr}$	m	ground range distance
$\hat{r}_{sr}$	m	slant range distance
$\mathbf{R}$	—	correlation coefficient
R	$\mathrm{J/(K \cdot mol)}$	gas constant
R_i	—	rotation matrix, rotation around the i-axis
R_e	m	Earth radius
SSA	cm^2/g	specific surface area
S_d	cm^{-1}	surface density of a firn sample
t_i	a	age of the i-th layer
T	°C | K	temperature
$\bar{T}$	°C | K	mean temperature
T_{atm}	K	atmospheric brightness temperature contribution
T_B	K	brightness temperature

Symbol	Unit	Value
z_i	m	depth of the i-th layer
Z_p	—	Fresnel reflection coefficient, polarization dependent
α	°	azimuth of local datum
γ	J/(kg · K)	specific heat capacity
Γ	—	power reflection coefficient
Υ	—	emissivity
$Up\hat{s}ilon$	—	transmissivity
δ_a	m	azimuth resolution (real aperture)
δ_{gr}	m	ground range resolution (real aperture)
δ_{ra}	m	range resolution (real aperture)
δ_{sa}	m	azimuth resolution (synthetic aperture)
δ_{sr}	m	slant range resolution
Δaz	m	SAR azimuth spacing
Δrg	m	SAR range spacing
ΔT	°C	temperature amplitude
$\Delta\, T_B$	K	seasonal brightness temperature amplitude
$\Delta\theta_{i,j}$	°	local incidence correction term
$\Delta\tau$	s	two-way signal traveltime
ε	F/m	dielectric constant
$\varepsilon', \varepsilon''$	F/m	real, imaginary part of the dielectric constant
ϑ_i	°	incidence angle component
ϑ_s	°	scattering angle component
θ	°	local angle of incidence
θ_a	°	local slope component in azimuth direction
θ_r	°	local slope component in range direction
θ^*	°	angle of incidence with reference to the ellipsoid
$\Delta\theta$	°	angle of incidence correction
Θ	°	elevation angle
$\hat{\kappa}$	W/(m · K)	thermal conductivity
$\kappa_a, \kappa_s, \kappa_e$	dB/m	absorption, scattering, extinction coefficients
λ	cm	wavelength
Λ	°	geographic longitude
Λ_0	°	longitude of map projection origin
ξ_a, ξ_s, ξ_e	—	absorption, scattering, extinction efficiencies
ρ	kg/m^3	density
ρ_0	kg/m^3	initial density

Symbol	Unit	Value
$\hat{\sigma}$	m	RMS height
σ^0	dB	radar backscatter coefficient
τ	s	pulse length
τ_i	—	attenuation factor of the i-th layer
φ_i	°	incidence angle component
φ_s	°	scattering angle component
ϕ	—	phase of seasonal shift
Φ	°	geographic latitude
Φ_0	°	latitude of map projection origin
Φ_1	°	standard parallel (latitude of true scale)
ω_i	—	single scattering albedo of the i-th layer

Acronyms

AWS	automatic weather station
GCM	general circulation model
DEM	digital elevation model
DML	Dronning Maud Land
DMRT	Dense medium radiative transfer
LP DAAC	Land Processes Distributed Active Archive Center, U.S. Geological Survey
MODIS	Moderate-resolution Imaging Spectroradiometer
NCAR	National Center for Atmospheric Research
NCEP	National Centers for Environmental Prediction
NSIDC	National Snow and Ice Data Center, University of Colorado
PO.DAAC	Physical Oceanography Distributed Active Archive Center, NASA
RAMP	Radarsat Antarctic Mapping Project
RMS	root mean square, standard deviation
SSA	specific surface area
SSM/I	Special Sensor Microwave/Imager
WGS84	World Geodetic System

Density records

Name	Longitude	Latitude	Source
DML01C97_00	-2.5500	-74.8550	doi:10.1594/PANGAEA.58434
DML03C97_00	1.9612	-74.4995	doi:10.1594/PANGAEA.58794
DML03C98_09	1.9608	-74.4992	doi:10.1594/PANGAEA.58410
DML04C97_00	7.2175	-74.3990	doi:10.1594/PANGAEA.58436
DML05C97_00	0.0073	-75.0025	doi:10.1594/PANGAEA.58795
DML05C98_06	0.0227	-75.0027	doi:10.1594/PANGAEA.58407
DML05C98_07	0.0362	-74.9970	doi:10.1594/PANGAEA.58806
DML05C98_32	0.0070	-75.0023	doi:10.1594/PANGAEA.58815
DML06C97_00	8.0053	-75.0007	doi:10.1594/PANGAEA.58796
DML07C97_00	-3.4303	-75.5815	doi:10.1594/PANGAEA.58792
DML07C98_31	-3.4303	-75.5815	doi:10.1594/PANGAEA.58814
DML08C97_00	3.2828	-75.7528	doi:10.1594/PANGAEA.58440
DML09C97_00	7.2130	-75.9333	doi:10.1594/PANGAEA.58793
DML10C97_00	11.3500	-75.2167	doi:10.1594/PANGAEA.58442
DML11C98_03	-8.4970	-74.8547	doi:10.1594/PANGAEA.58404
DML12C98_17	-6.4983	-75.0007	doi:10.1594/PANGAEA.58418
DML13C98_16	-4.4963	-75.0000	doi:10.1594/PANGAEA.58417
DML14C98_15	-1.4945	-74.9492	doi:10.1594/PANGAEA.58416
DML15C98_14	2.5010	-75.0837	doi:10.1594/PANGAEA.58415
DML16C98_13	5.0033	-75.1673	doi:10.1594/PANGAEA.58414
DML17C98_33	6.4985	-75.1670	doi:10.1594/PANGAEA.58816
DML18C98_04	-6.0000	-75.2503	doi:10.1594/PANGAEA.58405
DML19C98_05	-0.9950	-75.1673	doi:10.1594/PANGAEA.58406
DML20C98_08	0.9998	-74.7507	doi:10.1594/PANGAEA.58409
DML21C98_10	4.0017	-74.6672	doi:10.1594/PANGAEA.58807

Name	Longitude	Latitude	Source
DML22C98_11	6.5000	-75.0840	doi:10.1594/PANGAEA.58800
DML23C98_12	6.5017	-75.2508	doi:10.1594/PANGAEA.58413
DML24C98_18	-9.1807	-74.4490	doi:10.1594/PANGAEA.58419
DML25C00_01	0.0819	-75.0060	doi:10.1594/PANGAEA.58443
DML27C00_04	0.7040	-75.0560	doi:10.1594/PANGAEA.58445
DML60C98_02	-9.7417	-74.2050	doi:10.1594/PANGAEA.58797
DML76S05_11	0.0795	-75.0048	doi:10.1594/PANGAEA.708082
DML77S05_12	0.7221	-75.0603	doi:10.1594/PANGAEA.708083
DML78S05_13	1.3404	-75.1468	doi:10.1594/PANGAEA.708084
DML79S05_14	2.0122	-75.2037	doi:10.1594/PANGAEA.708085
DML80S05_15	2.7140	-75.2314	doi:10.1594/PANGAEA.708086
DML81S05_16	3.4240	-75.2363	doi:10.1594/PANGAEA.708087
DML82S05_17	4.1314	-75.2274	doi:10.1594/PANGAEA.708088
DML83S05_18	4.8331	-75.2474	doi:10.1594/PANGAEA.708089
DML84S05_19	5.5372	-75.2722	doi:10.1594/PANGAEA.708090
DML85S05_20	6.2482	-75.2651	doi:10.1594/PANGAEA.708091
DML86S05_21	6.9568	-75.2565	doi:10.1594/PANGAEA.708092
DML87S05_22	7.6553	-75.2278	doi:10.1594/PANGAEA.708093
DML88S05_23	8.3370	-75.1820	doi:10.1594/PANGAEA.708094
DML89S05_24	9.0263	-75.1421	doi:10.1594/PANGAEA.708095
DML90S05_25	9.7240	-75.1169	doi:10.1594/PANGAEA.708096
DML96C07_39	-9.9167	-71.4083	doi:10.1594/PANGAEA.615237
NGT03C93.2 (B16)	-37.6299	73.9402	doi:10.1594/PANGAEA.56560
NGT06C93.2 (B17)	-37.6248	75.2504	doi:10.1594/PANGAEA.57153
NGT14C93.2 (B18)	-36.4033	76.6170	doi:10.1594/PANGAEA.56615
NGT27C94.2 (B21)	-41.1374	80.0000	doi:10.1594/PANGAEA.57296
NGT37C95.2 (B26)	-49.2167	77.2533	doi:10.1594/PANGAEA.57798
NGT42C95.2 (B29)	-43.4920	76.0039	doi:10.1594/PANGAEA.57655

Envisat ASAR scenes

Orbit	Track	Pass	Polarization	Swath	Frame	Date
35398	274	Ascending	H	IS2	5607	07.12.2008
35516	392	Descending	H	IS2	5193	15.12.2008
35613	489	Ascending	V	IS4	5661	22.12.2008
35584	460	Ascending	H	IS2	5625	20.12.2008
35584	460	Ascending	H	IS2	5643	20.12.2008
35584	460	Ascending	H	IS2	5661	20.12.2008
35584	460	Ascending	H	IS2	5679	20.12.2008
35584	460	Ascending	H	IS2	5697	20.12.2008
35658	033	Descending	V	IS7	5337	25.12.2008
35670	045	Ascending	V	IS2	5607	26.12.2008
35671	046	Ascending	V	IS7	5499	26.12.2008
36214	088	Ascending	H	WS	5580	02.02.2009
36214	088	Ascending	H	WS	5652	02.02.2009

Bibliography

Abdalati, W. and Steffen, K. (1997). Snowmelt on the Greenland ice sheet as derived from passive microwave satellite data. *Journal of Climate*, 10:165–175.

Abdalati, W. and Steffen, K. (2001). Greenland ice sheet melt extent: 1979-1999. *Journal of Geophysical Research*, 106(D24):33,983–33,988.

Agricultural Research Service, U. S. Department of Agriculture, Electron & Confocal Microscopy Laboratory (2009). Electron microscopy unit snow page. http://emu.arsusda.gov/snowsite/default.html.

Alley, R., Bolzan, J., and Whillans, I. (1982). Polar firn densification and grain growth. *Annals of Glaciology*, 3:7–11.

Anderson, D. and Benson, C. (1963). The densification and diagenesis of snow. In Kingery, W., editor, *Ice and snow: properties, processes and applications*, chapter 30, pages 391–411. MIT Press, Cambridge.

Aoki, T., Aoki, T., Fukabori, M., Hachikubo, A., Tachibana, Y., and Nishio, F. (2000). Effects of snow physical parameters on spectral albedo and bidirectional reflectance of snow surface. *Journal of Geophysical Research*, 105(D8):10,219–10,236.

Arnaud, L., Barnola, J., and Duval, P. (2000). *Physics of ice core records*, chapter Physical modeling of the densification of snow/firn and ice in the upper part of polar ice sheets., pages 285–305. Hondoh, T., Sapporo, Hokkaido University Press.

Arthern, R., Winebrenner, D., and Vaughan, D. (2006). Antarctic snow accumulation mapped using polarization of 4.3-cm wavelength microwave emission. *Journal of Geophysical Research*, 111(D06107):1–10.

Bales, R., E., M.-T., and McConnell, J. (2001a). Variability of accumulation in northwest Greenland over the past 250 years. *Geophysical Research Letters*, 28(14):2679–2682.

Bales, R., McConnell, J., Mosley-Thompson, E., and Csatho, B. (2001b). Accumulation over the Greenland ice sheet from historical and recent records. *Journal of Geophysical Research*, 106(D24):33,813–33,825.

Bamber, J., Layberry, R., and Gogenini, S. (2001a). A new ice thickness and bed data set for the Greenland ice sheet 1: Measurement, data reduction, and errors. *Journal of Geophysical Research*, 106 (D24):33773–33780. Data provided by the National Snow and Ice Data Center DAAC, University of Colorado, Boulder, CO.

Bamber, J., Layberry, R., and Gogenini, S. (2001b). A new ice thickness and bed data set for the Greenland ice sheet 2: Relationship between dynamics and basal topography. *Journal of Geophysical Research*, 106 (D24):33781–33788. Data provided by the National Snow and Ice Data Center DAAC, University of Colorado, Boulder, CO.

Baunach, T., Fierz, C., Satyawali, P., and Schneebeli, M. (2001). A model for kinetic grain growth. *Annals of Glaciology*, 32(1):1–6.

Bindschadler, R., Choi, H., Shuman, C., and Markus, T. (2005). Detecting and measuring new snow accumulation on ice sheets by satellite remote sensing. *Remote Sensing of Environment*, 98(4):388–402.

Bingham, A. and Drinkwater, M. (2000). Recent changes in the microwave scattering properties of the Antarctic ice sheet. *IEEE Transactions on Geoscience and Remote Sensing*, 38(4):1810–1820.

Bohlander, J. and Scambos, T. c. (2001). THERMAP Antarctic ice sheet temperature data. Digital media.

Budd, W. and Jacka, T. (1989). A review of ice rheology for ice sheet modelling. *Cold Regions Science and Technology*, 16(2):107 – 144.

Burgess, E. W., R., F. R., Box, J. E., Mosley-Thompson, E., Bromwich, D. H., Bales, R. C., and Smith, L. C. (2010). A spatially calibrated model of annual accumulation rate on the Greenland ice sheet (1958-2007). *Journal of Geophysical Research*, 115:F02004.

Burke, W., Schmugge, T., and Paris, J. (1979). Comparison of 2.8- and 21-cm microwave radiometer observations over soils with emission model calculations. *Journal of Geophysical Research*, 84:287–294.

Chen, J. L., Wilson, C. R., Blankenship, D., and Tapley, B. D. (2009). Accelerated Antarctic ice loss from satellite gravity measurements. *Nature Geoscience*, 2:859–862.

Chuah, H.-T., Tjuatja, S., Fung, A., and Bredow, J. (1997). Radar backscatter from a dense discrete random medium. *Geoscience and Remote Sensing, IEEE Transactions on*, 35(4):892–900.

Cogley, J. G. (2004). Greenland accumulation: An error model. *Journal of Geophysical Research*, 109:D18101.

Colbeck, S. (1983). Theory of metamorphism of dry snow. *Journal of Geophysical Research*, 88:5475–5482.

Comiso, J. (2000). Variability and trends in Antarctic surface temperatures from in situ and satellite infrared measurements. *Journal of Climate*, 13:1674–1696.

Courville, Z., Albert, M., Fahnestock, M., Cathles, L., and Shuman, C. (2007). Impacts of an accumulation hiatus on the physical properties of firn at a low-accumulation polar site. *Journal of Geophysical Research*, 112:10.

Davis, C. and Poznyak, V. (1993). The depth of penetration in Antarctic firn at 10 ghz. *Geoscience and Remote Sensing, IEEE Transactions on*, 31(5):1107–1111.

Dethloff, K., Schwager, M., Christensen, J., Kiilsholm, S., Rinke, A., Dorn, W., Jung-Rothenhäusler, F., Fischer, H., Kipfstuhl, S., and Miller, H. (2002). Recent greenland Accumulation estimated from regional climate model simulations and ice core analysis. *Journal of Climate*, 15:2821–2832.

Domine, F., Albert, M., Huthwelker, T., Jacobi, H.-W., Kokhanovsky, A., Lehning, M., Picard, G., and Simpson, W. (2008). Snow physics as relevant to snow photochemistry. *Atmospheric Chemistry and Physics*, 8(2):171–208.

Drinkwater, M., Long, D., and Bingham, A. (2001). Greenland snow accumulation estimates from satellite radar scatterometer data. *Journal of Geophysical Research*, 106(D24):33935–33950.

Eisen, O., Frezzotti, M., Genthon, C., Isaksson, E., Magand, O., van den Broeke, M., Dixon, D., Ekaykin, A., Holmlund, P., Kameda, T., Karlöf, L., Kaspari, S., Lipenkov, V., Oerter, H., Takahashi, S., and Vaughan, D. (2008). Ground-based measurements of spatial and temporal variability of snow accumulation in East Antarctica. *Reviews of Geophysics*, 46:RG2001.

ESA (2007). ASAR product handbook. Issue 2.2.

Fierz, C., Armstrong, R., Durand, Y., Etchevers, P., Greene, E., McClung, D., Nishimura, K., Satyawali, P., and Sokratov, S. (2009). The international classification for seasonal snow on the ground. IHP-VII Technical Documents in Hydrology 83, UNESCO-IHP, Paris. IACS Contribution No. 1.

Flach, J., Partington, K., Ruiz, C., Jeansou, E., and Drinkwater, M. (2005). Inversion of the surface properties of ice sheets from satellite microwave data. *IEEE Transactions on Geoscience and Remote Sensing*, 43(4):743–752.

Flanner, M. and Zender, C. (2006). Linking snowpack microphysics and albedo evolution. *Journal of Geophysical Research*, 111:D12208.

Forster, R., Jezek, K., Bolzal, J., and Baumgartner, F. (1999). Relationships between radar backscatter and accumulation rates on the Greenland ice sheet. *Int. J. Remote Sensing*, 20(15&16):3131–3147.

Freitag, J., Wilhelms, F., and Kipfstuhl, S. (2004). Microstructure-dependent densification of polar firn derived from X-ray microtomography. *Journal of Glaciology*, 50:243–250.

Fung, A. (1994). *Microwave Scattering and Emission Models and Their Applications*. Artech House Publishers.

Genthon, C., Magand, O., Krinner, G., and Fily, M. (2009). Do climate models underestimate snow accumulation on the Antarctic plateau? a re-evaluation of/from in situ observations in East Wilkes and Victoria Lands. *Annals of Glaciology*, 50:61–65(5).

Gerland, S., Oerter, H., Kipfstuhl, J., Wilhelms, F., Miller, H., and Miners, W. (1999). Density log of a 181 m long ice core from Berkner Island, Antarctica. *Annals of Glaciology*, 29:215–219.

Giovinetto, M. and Zwally, H. (2000). Spatial distribution of net surface accumulation on the Antarctic ice sheet. *Annals of Glaciology*, 31:171–178(8).

Gow, A. (1975). Time-temperature dependence of sintering in perennial isothermal snowpacks. In *Snow Mechanics Symposium: Proceedings of the Grindelwald symposium*, volume 114 of *IAHS-AISH publication*, pages 25–41. International Association of Hydrological Sciences.

Gow, A., Meese, D., and Bialas, R. (2004). Accumulation variability, density profiles and crystal growth trends in ITASE firn and ice cores from West Antarctica. *Annals of Glaciology*, 39:101–109.

Gow, A. J. (1965). On the accumulation and seasonal stratification of snow at the South Pole. *Jounal of Glaciology*, 5:467–477.

Gow, A. J. (1969). On the rates of growth of grains and crystals in South Polar firn. *Journal of Glaciology*, 8(53):241–252.

Grenfell, T. and Warren, S. (1999). Representation of a nonspherical ice particle by a collection of independent spheres for scattering and absorption of radiation. *Journal of Geophysical Research*, 104(D24):31,697–31,709.

Hall, D. K., Box, J. E., Casey, K. A., Hook, S. J., Shuman, C. A., and Steffen, K. (2008). Comparison of satellite-derived and in-situ observations of ice and snow surface temperatures over Greenland. *Remote Sensing of Environment*, 112(10):3739 – 3749.

Helm, V., Rack, W., Cullen, R., Nienow, P., Mair, D., Parry, V., and Wingham, D. (2007). Winter accumulation in the percolation zone of Greenland measured by airborne radar altimeter. *Geophysical Research Letters*, 34:L06501.

Herron, M. and Langway, C. C. J. (1980). Firn densification: an empirical model. *Journal of Glaciology*, 25(93):373–385.

Hörhold, M. W. (2010). *Investigations of the climatic impact on polar firn structure using high resolution density measurements and 3D-X-ray-microfocus-computer-tomography.* PhD thesis, University of Bremen.

Hörhold, M. W., Kipfstuhl, S., Wilhelms, F., Freitag, J., and Frenzel, A. (2010). The densification of layered polar firn. *Journal Of Geophysical Research*, page F01001.

Huybrechts, P., Steinhage, D., Wilhelms, F., and Bamber, J. (2000). Balance velocities and measured properties of the Antarctic ice sheet from a new compilation of gridded data for modelling. *Annals of Glaciology*, 30:52–60.

Jacka, T. and Li, J. (1994). The steady-state crystal size of deforming ice. *Annals of Glaciology*, 20:13–18.

Jezek, K., Drinkwater, M., Crawford, J., Bindschadler, R., and Kwok, R. (1993). Analysis of synthetic aperture radar data collected over the southwestern Greenland ice sheet. *Journal of Glaciology*, 39:119–132.

Jezek, K., Gogineni, P., and Shanableh, M. (1994). Radar measurements of melt zones on the Greenland ice sheet. *Geophysical Research Letters*, 21(1):33–36.

Jiang, L., Shi, J., Tjuatja, S., Dozier, J., Chen, K., and Zhang, L. (2007). A parameterized multiple-scattering model for microwave emission from dry snow. *Remote Sensing of Environment*, 111(2-3):357 – 366. Remote Sensing of the Cryosphere Special Issue.

Jordan, R. (1991). A one-dimensional temperature model for a snow cover. Special Report SR 91-16, U.S. Army Cold Regions Research and Engineering Laboratory.

Kaempfer, T. and Schneebeli, M. (2007). Observation of isothermal metamorphism of new snow and interpretation as a sintering process. *Journal of Geophysical Research*, 112:D24101.

König, L., Steig, E., Winebrenner, D., and Shuman, C. (2007). A link between microwave extinction length, firn thermal diffusivity, and accumulation rate in West Antarctica. *Journal of Geophysical Research*, 112:F03018.

Lacroix, P., Dechambre, M., Legresy, B., Blarel, F., and Remy, F. (2008). On the use of the dual-frequency ENVISAT altimeter to determine snowpack properties of the Antarctic ice sheet. *Remote sensing of environment*, 112:1712–1729.

Legresy, B. and Remy, F. (1998). Using the temporal variability of satellite radar altimetric observations to map surface properties of the Antarctic ice sheet. *Journal of Glaciology*, 44(147):197–206.

Li, Z., Tan, Y., and Tsang, L. (2006). Modeling the passive microwave remote sensing of snow using dense media radiative transfer theory with NMM3D rough-surface boundary conditions. *Microwave and optical technology letters*, 48:557–562.

Liu, H., Jezek, K., Li, B., and Zhao, Z. (2001). Radarsat Antarctic Mapping Project digital elevation model version 2. Digital media.

Liu, H., Wang, L., and Jezek, K. (2006). Automated delineation of dry and melt snow zones in Antarctica using active and passive microwave observations from space. *IEEE Transactions on Geoscience and Remote Sensing*, 44:2152– 2163.

Long, D. (2006). BYU daily browse images of QuikSCAT sigma-0 measurements.

Long, D. and Drinkwater, M. (1994). Greenland ice-sheet surface properties observed by the Seasat-A scatterometer at enhanced resolution. *Journal of Glaciology*, 40:213–230.

LPDAAC (2009a). Land surface temperature & emissivity 8-day l3 global 1km. Digital media.

LPDAAC (2009b). MODIS reprojection tool. Digital media.

Maeno, N. and Ebinuma, T. (1983). Pressure sintering of ice and its implication to the densification of snow at polar glaciers and ice sheets. *Journal of Physical Chemistry*, 87:4103–4110.

Magand, O., Genthon, C., Fily, M., Krinner, G., Picard, G., Frezzotti, M., and Ekaykin, A. (2007). An up-to-date quality-controlled surface mass balance data set for the 90°-180°e Antarctica sector and 1950-2005 period. *Journal of Geophysical Research*, 112:D12106.

Maslanik, J. and Stroeve, J. (1990). DMSP SSM/I daily polar gridded brightness temperatures, 2007/01/01-2007/12/31. Digital media. (updated current year).

Massom, R. and Lubin, D. (2006). *Polar Remote Sensing*. Springer.

Mätzler, C. (1998). Improved Born approximation for scattering of radiation in a granular medium. *Journal of Applied Physics*, 83:6111.

Mätzler, C. and Wiesmann, A. (1999). Extension of the Microwave Emission Model of Layered Snowpacks to coarse-grained snow. *Remote Sensing of Environment*, 70(3):317 – 325.

Monaghan, A. J., Bromwich, D., and Wang, S.-H. (2006). Recent trends in antarctic snow accumulation from polar mm5 simulations. *Philisophical Transactions of the Royal Society*, A 364:1683–1708.

Munk, J., Jezek, K., Forster, R., and Gogineni, S. (2003). An accumulation map for the Greenland dry-snow facies derived from spaceborne radar. *Journal of Geophysical Research*, 108(D9):8.

Nghiem, S., Steffen, K., Neumann, G., and Huff, R. (2005). Mapping of ice layer extent and snow accumulation in the percolation zone of the Greenland ice sheet. *Journal of Geophysical Research*, 110:F02017.

Oerter, H., Fischer, H., and Sperlich, P. (2008). Spatial variability of delta 18-O upstream and around the EDML drilling site. In *Quaternary Climate: from Pole to Pole, EPICA Open Science Conference, Venice, Italy.*

Oerter, H., Graf, W., Wilhelms, F., Minikin, A., and Miller, H. (1999). Accumulation studies on Amundsenisen, Dronning Maud Land, Antarctica, by means of tritium, dielectric profiling and stable-isotope measurements: first results from the 1995-96 and 1996-97 field seasons. *Annals of Glaciology*, 29:1–9(9).

Oerter, H., Wilhelms, F., Jung-Rothenhausler, F., Goktas, F., Miller, H., Graf, W., and Sommer, S. (2000). Accumulation rates in Dronning Maud Land, Antarctica, as revealed by dielectric-profiling measurements of shallow firn cores. *Annals of Glaciology*, 30:27–34(8).

Ohmura, A. (1987). New temperature distribution maps for Greenland. *Zeitschrift für Gletscherkunde und Glazialgeologie*, 23:1–45.

Ohmura, A. and Reeh, N. (1991). New precipitation and accumulation maps for Greenland. *Journal of Glaciology*, 125:140–148.

Oveisgharan, S. and Zebker, H. (2007). Estimating snow accumulation from InSAR correlation observations. *IEEE Transactions on Geoscience and Remote Sensing*, 45:10 – 20.

Pack, J. and Jensen, M. (2001). Estimating snow accumulation on Greenland from SSM/I radiometerdata. *Geoscience and Remote Sensing Symposium, 2001. IGARSS '01. IEEE 2001 International*, 2:946–948.

Palais, J., Whillans, I., and Bull, C. (1982). Snow stratigraphic studies at Dome C, East Antarctica. *Annals of Glaciology*, 3:239–242.

Paterson, W. (1999). *Physics of Glaciers*. Butterworth-Heinemann, 3 edition.

Petty, G. W. (2006). *A First Course In Atmospheric Radiation*. Sundog Publishing, Madison, Wisconsin, 2 edition.

Picard, G., Fily, M., and Gallee, H. (2007). Surface melting derived from microwave radiometers: a climatic indicator in Antarctica. *Annals of Glaciology*, 46:29–34.

Pruppacher, H. R. and Klett, J. D. (1997). *Microphysics of Clouds and Precipitation*. Atmospheric and Oceanographic Sciences Library. Kluwer Academic Publishers, 2 edition.

Rau, F. and Braun, M. (2002). The regional distribution of the dry-snow zone on the Antarctic Peninsula north of 70°s. *Annals of Glaciology*, 34:95–100.

Reeh, N. (1989). Parameterization of melt rate and surface temperature on the Greenland ice sheet. *Polarforschung*, 59:113–128.

Rignot, E., Bamber, J., van den Broeke, M., Davis, C., Li, Y., van de Berg, W., and van Meijgaard, E. (2008a). Recent Antarctic ice mass loss from radar interferometry and regional climate modelling. *Nature Geoscience*, 1:106–110.

Rignot, E., Box, J., Burgess, E., and Hanna, E. (2008b). Mass balance of the Greenland ice sheet from 1958 to 2007. *Geophysical Research Letters*, 35:L20502.

Rosich, B. and Meadows, P. (2004). Absolute calibration od ASAR Level 1 products generated with PF-ASAR. Technical Note ENVI-CLVL-EOPG-TN-03-0010, ESA-ESRIN.

Rotschky, G. (2007). *Spatial distribution of snow accumulation and snowpack properties in Dronning Maud Land, Antarctica: Observational techniques and methods for surface-mass balance assessments of polar ice sheets*. PhD thesis, Bremen University.

Rotschky, G., Holmlund, P., Isaksson, E., Mulvaney, R., Oerter, H., Van Den Broeke, M., and Winther, J.-G. (2007). A new surface accumulation map for western Dronning Maud Land, Antarctica, from interpolation of point measurements. *Journal of Glaciology*, 53:385–398(14).

Rotschky, G., Rack, W., Dierking, W., and Oerter, H. (2006). Retrieving snowpack properties and accumulation estimates from a combination of SAR and scatterometer measurements. *IEEE Transactions on Geoscience and Remote Sensing*, 44(4):943–956.

Rott, H., Sturm, K., and Miller, H. (1993). Active and passive microwave signatures of Antarctic firn by means of field measurements and satellite data. *Annals of Glaciology*, 17:337–343.

Sasgen, I., Martinec, Z., and Fleming, K. (2007). Regional ice-mass changes and glacial-isostatic adjustment in Antarctica from GRACE. *Earth and Planetary Science Letters*, 264(3-4):391 – 401.

Schlosser, E., Duda, M., Powers, J., and Manning, K. (2008). Precipitation regime of Dronning Maud Land, Antarctica, derived from Antarctic Mesoscale Prediction System (AMPS) archive data. *Journal of Geophysical Research*, 113:D24108.

Schlosser, E., van Lipzig, N., and Oerter, H. (2002). Temporal variability of accumulation at Neumayer station, Antarctica, from stake array measurements and a regional atmospheric model. *Journal of Glaciology*, 48(160):87–94.

Schwager, M. (2000). *Eisbohrkernuntersuchungen zur räumlichen und zeitlichen Variabilität von Temperatur und Niederschlagsrate im Spätholozän in Nordgrönland*. PhD thesis, Bremen University. Ber. Polarforsch. 362 (2000), ISSN 0176 - 5027.

Shepherd, A. and Wingham, D. (2007). Recent sea-level contributions of the Antarctic and Greenland ice sheets. *Science*, 315:1529 – 1532.

Shi, J. and Dozier, J. (2000). Estimation of snow water equivalence using SIR-C/X-SAR. ii. inferring snow depth and particle size. *Geoscience and Remote Sensing, IEEE Transactions on*, 38(6):2475–2488.

Shuman, C., Fahnestock, M., Scambos, T., Haran, T., Bauer, R., Cathles, M., Courville, Z., Albert, M., and Suchdeo, V. (2008). Antarctic megadunes and other low accumulation features on the East Antarctic plateau from ICESat. Presentation.

Snyder, J. (1987). *Map Projections – A Working Manual*. USGS Professional Paper 1395.

Steffen, K. and Box, J. (2001). Surface climatology of the Greenland ice sheet: Greenland Climate Network 1995-1999. *Journal Of Geophysical Research*, 106(D24):33,951–33,964.

Steffen, K., Box, J., and Abdalati, W. (1996). Greenland Climate Network: GC-Net. Special report SR 96-27, U.S. Army Cold Regions Research and Engineering Laboratory.

Sturm, M., Holmgren, J., Koenig, M., and Morris, K. (1997). The thermal conductivity of seasonal snow. *Journal of Glaciology*, 43(143):26–41.

Surdyk, S. (2002). Low microwave brightness temperatures in central Antarctica: observed features and implications. *Annals of Glaciology*, 34:134–140(7).

Surdyk, S. and Fily, M. (1995). Results of a stratified snow emissivity model based on the wave approach: Application to the Antarctic ice sheet. *Journal of Geophysical Research*, 100(C5):8837–8848.

Swift, C., Hayes, P., Herd, J., Jones, W., and Delnore, V. (1985). Airborne microwave measurements of the southern Greenland ice sheet. *Journal of Geophysical Research*, 90(B2):1983–1994.

Takahashi, S., Kameda, T., Enomoto, H., Shiraiwa, T., Kodama, Y., Fujita, S., Motoyama, H., Watanabe, O., Weidner, G., and Stearns, C. (1998). Automatic weather station program during Dome Fuji Project by JARE in east Dronning Maud Land, Antarctica. *Annals of Glaciology*, 27:528–534.

Tedesco, M. and Kim, E. J. (2006). Intercomparison of electromagnetic models for passive microwave remote sensing of snow. *IEEE Transactions on Geoscience and Remote Sensing*, 44:2654 – 2666.

Tedesco, M., Pulliainen, J., Takala, M., Hallikainen, M., and Pampaloni, P. (2004). Artificial neural network-based techniques for the retrieval of SWE and snow depth from SSM/I data. *Remote Sensing of Environment*, 90:76–85.

Torge, W. (2001). *Geodesy.* de Gruyter, 3rd edition.

Tsang, L. (1992). *Dense media radiative transfer theory for dense discrete random media with spherical particles of multiple sizes and permittivities*, volume 6, chapter 5, Dielectric Properties of Heterogeneous Materials, pages 181–230. Elsevier, New York.

Tsang, L., Chen, C.-T., Chang, A. T. C., Guo, J., and Ding, K.-H. (2000). Dense media radiative transfer theory based on quasicrystalline approximation with applications to passive microwave remote sensing of snow. *Radio Science*, 35:731–749.

Tsang, L., Kong, J., and Shin, R. (1985). *Theory of Microwave Remote Sensing.* Wiley-Interscience, 2nd edition. ISBN 978-0471888604.

Tsang, L., Pan, J., Liang, D., Li, Z., Cline, D., and Tan, Y. (2007). Modeling active microwave remote sensing of snow using dense media radiative transfer (DMRT) theory with multiple-scattering effects. *Geoscience and Remote Sensing, IEEE Transactions on*, 45(4):990–1004.

Ulaby, F., Moore, R., and Fung, A. (1981). *Microwave Remote Sensing*, volume I. Addison-Wesley Publishing Company.

Ulaby, F., Moore, R., and Fung, A. (1982). *Microwave Remote Sensing*, volume II. Addison-Wesley Publishing Company.

Ulaby, F., Moore, R., and Fung, A. (1986). *Microwave Remote Sensing*, volume III. Artech House.

Ulander, L. (1995). A new look at the slope correction for SAR radiometric calibration. In *Geoscience and Remote Sensing Symposium, 1995. IGARSS '95. 'Quantitative Remote Sensing for Science and Applications', International*, volume 1, pages 602–604.

Van de Berg, W., Van den Broeke, M., Reijmer, C., and Van Meijgaard, E. (2005). Characteristics of the antarctic surface mass balance, 1958-2002, using a regional atmospheric climate model. *Annals of Glaciology*, 41:97–104(8).

Vaughan, D., Bamber, J., Giovinetto, M., Russell, J., and Cooper, A. (1999). Reassessment of net surface mass balance in Antarctica. *J. Climate*, 12:933–946.

Velicogna, I. (2009). Increasing rates of ice mass loss from the Greenland and Antarctic ice sheets revealed by GRACE. *Geophysical Research Letters*, 36:L19503.

Wan, Z. (2008). New refinements and validation of the MODIS land-surface temperature/emissivity products. *Remote Sensing of Environment*, 112(1):59 – 74.

Welker, C. (2007). Studies of snow characteristics in Dronning Maud Land, Antarctica, by means of satellite-borne microwave radiometry. Master's thesis, University of Innsbruck.

Wen, B., Tsang, L., Winebrenner, D., and Ishimaru, A. (1990). Dense medium radiative transfer theory: comparison with experiment and application to microwave remote sensing and polarimetry. *Geoscience and Remote Sensing, IEEE Transactions on*, 28(1):46–59.

Wesche, C. (2009). *Evaluation and application of GPS and altimetry data over central Dronning Maud Land, Antarctica: annual elevation change, a digital elevation model, and surface flow velocity.* PhD thesis, Universität Bremen.

West, R. (1994). *Microwave emission from polar firn.* PhD thesis, University of Washington.

West, R., Winebrenner, D., Tsang, L., and Rott, H. (1996). Microwave emission from density-stratified Antarctic firn at 6 cm wavelength. *Journal of Glaciology*, 42:63–76.

West, R. D. (1990). Polarimetric radar signatures for two layers of dense random media. Master's thesis, University of Washington.

Wiesmann, A. and Mätzler, C. (1999). Microwave emission model of layered snowpacks. *Remote Sensing of Environment*, 70:307–316.

Wilhelms, F. (2000). *Messung dielektrischer Eigenschaften polarer Eiskerne (Measuring the Dielectric Properties of Polar Ice Cores).* PhD thesis, Universität Bremen. Ber. Polarforsch. 191 (1996), ISSN 0176 - 5027.

Winebrenner, D., Arthern, R., and Shuman, C. (2001). Mapping Greenland accumulation rates using observations of thermal emission at 4.5-cm wavelength. *Journal of Geophysical Research*, 106(D24):33919–33934.

Zwally, H. and Li, J. (2002). Seasonal and interannual variations of firn densification and ice-sheet surface elevation at the Greenland summit. *Journal of Glaciology*, 48:199–207.

Acknowledgements

First of all, I would like to thank Prof. Peter Lemke for the opportunity to conduct my doctoral thesis at the Alfred-Wegener-Institute for Polar and Marine Research (AWI), and for supervising this thesis on behalf on the University of Bremen. I also thank Prof. Justus Notholt for taking over the additional report.

I am very grateful to my advisor, Wolfgang Dierking, for always being there to provide assistance and advice when needed, and for his patience and support. Many thanks also go to Maria Hörhold for the grain size measurements and, together with Johannes Freitag, giving helpful advice needed for understanding snow microstructure and carefully reviewing this thesis. I also thank Wolfgang Rack for the advice concerning SAR image processing, and Hans Oerter for providing the in-situ data. Further thanks go to Christine Wesche for advice and proofreading, as well as the entire AWI EOS working group for their support.

Last but not least, I wish to thank friends and family who provided me with good advice, much needed distractions and a steady supply of caffeine.

This work was funded by the DFG priority program “Mass transport and mass distribution in the system Earth” (SPP-1257).